POLITECNICO DI TORINO

Corso di Laurea Magistrale in Ingegneria Civile
Dipartimento di Ingegneria Strutturale, Edile e Geotecnica



Tesi di Laurea Magistrale

Numerical Modeling of Debris Flow Events in the Rio Gadria Catchment (Bolzano, Italy)

Relatrice
Prof.ssa Marina Pirulli

Candidata
Francesca Paravella

Correlatrice
Dott.ssa Giulia La Porta

Anno Accademico 2025-2026

Abstract

Debris flows are rapid mass movements of water and sediment that represent one of the most hazardous geomorphological processes in mountainous regions, often causing loss of life and severe damage to infrastructure, property, and economic activities. Among the main triggering factors is intense rainfall, as water infiltration can modify pore-water pressure and promote the mobilization of shallow soil layers. Climate change is expected to increase the frequency and intensity of extreme precipitation events, thereby enhancing slope instability and fostering the occurrence of debris flows. Consequently, improving the understanding and prediction of debris-flow initiation and propagation has become increasingly important for hazard assessment and risk mitigation. In this context, long-term monitoring systems provide valuable datasets for investigating debris-flow dynamics and validating numerical models.

This thesis focuses on the numerical modeling of debris-flow dynamics using a depth-averaged continuum approach that simulates the heterogeneous mass as an equivalent homogeneous flow. The flow behavior is described through the Voellmy rheological law, which incorporates two dissipative terms accounting for frictional and turbulent resistance mechanisms.

The study exploits the comprehensive monitoring dataset available for the Rio Gadria basin (Bolzano, Italy), an Alpine catchment that has been extensively instrumented for debris-flow monitoring since 2011. First, a benchmark event that occurred on 18 July 2013 is back-analyzed to calibrate the rheological parameters by comparing numerical simulations with flow hydrographs derived from stage-sensor measurements recorded at two monitoring stations along the channel. Subsequently, the calibrated parameters are applied to a second debris-flow event recorded in the same basin in 2019 to evaluate their transferability and predictive capability. Model performance is assessed using the available monitoring data for validation.

The results highlight the importance of integrating detailed monitoring observations with numerical modeling to improve the understanding of complex and highly variable phenomena such as debris flows. Numerical models can provide valuable support for hazard assessment and risk mitigation, provided that they are capable of realistically reproducing debris-flow dynamics. The availability of measurements from real events through monitoring systems represents a fundamental basis for model validation and performance evaluation, enhancing the reliability of model-based applications in risk management.

Contents

Abstract . . . . . **I**

List of Figures . . . . . **X**

List of Tables . . . . . **XI**

1 Introduction **1**

2 From landslides to debris flows: classification, triggering mechanisms and flow dynamics **4**

2.1 Classification of landslide phenomena 5
2.2 Factors controlling slope instability 8
2.3 Rainfall-induced shallow landslide 9
2.4 Flow-like landslides 11
2.5 Definition and characteristics of debris flows 13
2.5.1 Triggering analysis 14
2.5.2 Runout analysis 15

3 Case study **18**

3.1 Geographical framework 18
3.2 Geological and Geomorphological setting 20
3.2.1 Geological setting 20
3.2.2 Geomorphological characteristics 21
3.3 Climate characteristics of the basin 23
3.4 Debris-flow mitigation interventions 24
3.5 The open-air laboratory of Rio Gadria basin 25
3.5.1 Rain gauges 29
3.5.2 Stage sensors radar 30
3.5.3 Geophones 31
3.5.4 Video cameras 32
3.5.5 Hydrological monitoring tools 33
3.5.6 Monitoring barrier 34
3.6 Description of the analyzed events 35
3.6.1 July 18, 2013 event 35
3.6.2 July 26, 2019 event 38

4 Numerical modeling of debris-flow events 42
4.1 RASH3D numerical code 42
4.2 Model setup for the 18 July 2013 event 47
4.2.1 Identification of the source area 47
4.2.2 Topographic input data 49
4.2.3 Mesh generation 51
4.2.4 Rheological law 57
4.3 Model setup for the 26 July 2019 event 58
4.3.1 Identification of source area 58
4.3.2 Topographic input data 59
4.3.3 Mesh generation 60
4.3.4 Rheological law 60

5 Results and discussion 61
5.1 18 July 2013 event: flow dynamics and rheological calibration 61
5.2 18 July 2013 event: deposition and check-dam configurations 74
5.3 26 July 2019 event: assessment of parameter transferability 77

6 Conclusions 83

A Additional results based on spatial mean value 86

Bibliography 97

Website References 101

List of Figures

2.1 Types of landslides: **(a)** fall, **(b)** topple, **(c)** slide, **(d)** spread, **(e)** flow. Source: **Cruden and Varnes** (**1996**) 6
2.2 Classification based on the rate of movement and attribution of the velocity class (**Cruden and Varnes**, **1996**). 7
2.3 Definition of probable destructive significance of different velocity classes (**Cruden and Varnes**, **1996**). 8
2.4 Schematization of destabilizing factors acting on a slope. Source: modified from **Glade et al.** (**2005**). 9
2.5 Conceptual representation of rainfall infiltration in unsaturated soils and its consequences (**Ahmadi-Adli**, **2014**). 10
2.6 Classification of flow-like landslides (**Hungr et al.**, **2001**). 12
2.7 Material involved in flow-like landslides (**Hungr et al.**, **2001**). 13
2.8 Schematic representation of the triggering and runout phases. Source: modified from **La Porta et al.** (**2024**). 14
2.9 Scheme of a surge wave of a debris flow (**Hungr et al.**, **2001**). 16

3.1 Geographical context of the study area. **(a)** Trentino Alto-Adige region and Autonomous Province of Bolzano; **(b)** Autonomous Province of Bolzano showcasing the Val Venosta area; **(c)** detailed view of Val Venosta, emphasizing Gadria catchment, Strimm basin and alluvial fan at the confluence between the two. 18
3.2 Altimetric map of the Rio Gadria basin. 19
3.3 Slope map in degrees (°) of the Rio Gadria basin. 19
3.4 Map and location of the Gadria-Strimm catchments and their alluvial fan. 20
3.5 View of the Gadria basin: **(a)** kame terraces deposits (**Comiti et al.**, **2014**); **(b)** main channel in the upper part of the basin (**Comiti et al.**, **2014**); **(c)** main channel in the lower part of the basin within the instrumented part (**Comiti et al.**, **2014**); **(d)** main channel from above looking at the deposition basin (**Provincia Autonoma di Bolzano - Alto Adige**, **2026a**); **(e)** detail of the channel in the central part (**Provincia Autonoma di Bolzano - Alto Adige**, **2026a**). 22
3.6 Land cover map of the Rio Gadria basin (**Bressan**, **2024**). 23
3.7 Detailed view of some consolidation check dams (**Provincia Autonoma di Bolzano - Alto Adige**, **2026a**). 24

3.8 Views of the filter check dam: **(a)** photo taken from downstream; **(b)** photo taken from above after an event including the deposition basin. Sources: **(a) Bressan** (**2024**), **(b) Provincia Autonoma di Bolzano - Alto Adige** (**2026a**) 25
3.9 Spatial distribution of the monitoring instruments installed in the Gadria basin: **(a)** overview of the catchment and its installations; **(b)** detailed view of the red area in figure (a). 27
3.10 View of instrumented sections upstream the retention basin: **(a)** photo of sections D2 and D3 from downstream; **(b)** photo from upstream of section D2 and D1, comprehensive of monitoring barrier, retention basin and its filter check dam. Source: **Provincia Autonoma di Bolzano - Alto Adige** (**2026a**) 27
3.11 Stage sensor radar: **(a)** scheme of the position of the two radar sensors in the instrumented area and detail of the geometry sensor (**Dei Cas et al.**, **2021**); **(b)** Photo taken after an occurred event to highlight the position of stage radar sensor with respect the main channel (**Provincia Autonoma di Bolzano - Alto Adige**, **2026a**). 31
3.12 Detail of one of the vertical 10-Hz geophones (**Coviello et al.**, **2019**). . . . 32
3.13 Video camera and spotlight installed at site (**Dei Cas et al.**, **2021**). 33
3.14 Monitoring barrier in the centerline of the channel: **(a)** photo of the barrier taken from above (**Provincia Autonoma di Bolzano - Alto Adige**, **2026a**); **(b)** photo of the barrier taken downstream it (**Nagl et al.**, **2020**); **(c)** Illustration of the monitoring barrier and sensors position (**Nagl et al.**, **2020**); **(d)** photo of monitoring barrier from August 2017 taken upstream it (**Nagl et al.**, **2022**). 35
3.15 Cumulative precipitation curve of July 18, 2013 36
3.16 Hydrograph at station D2 and D3 of the July 18, 2013 debirs-flow event. . 36
3.17 Frames of the July 2013 debris flow from the video cameras at section D1 and D2: **(a)** snapshot of the front arrival at D1 downstream video camera; **(b)** frame of the front arrival at D1 upstream video camera which is looking through the deposition basin; **(c)** picture of the deposition basin after the event from D1 upstream video camera; **(d)** snapshot showing the initial front at D2; **(e)** frame of the central part of the event at D2; **(f)** picture of an advanced surge carrying a big boulder at D2. Source: personal communication with University of Bolzano 37
3.18 Cumulative precipitation curve of July 26, 2019 39
3.19 Hydrograph at station D2 and D3 of the July 26, 2019 debirs-flow event. . 39

3.20 Frames of the July 2019 debris flow from the video cameras at section D1 and D2: **(a)** snapshot of the front arrival at D1 downstream video camera; **(b)** frame of the front arrival at D1 upstream video camera which is looking through the deposition basin; **(c)** picture of the deposition basin after the event from D1 upstream video camera; **(d)** snapshot showing the precursory flow before the front arrival; **(e)** frame of the initial front at D2; **(f)** picture of the central part of the event at D2. Source: personal communication with University of Bolzano 40

4.1 From a complex moving mass to an equivalent continuum (**Pirulli and Mangeney**, **2008**): **(a)** heterogeneous flowing mass; **(b)** equivalent fluid. . 43
4.2 Scheme of the equivalent fluid with its characteristic dimensions. Source: modified from **Pirulli and Mangeney** (**2008**). 44
4.3 Source datasets used for the identification of the triggering area adopted in the numerical model: **(a)** MPI map proposed by **D'Agostino and Bertoldi** (**2014**); **(b)** Gadria basin system with indication of the initiation area of the 18 July 2013 debris-flow event (modified from **Finis et al.** (**2017**)). 48
4.4 Source area adopted for the numerical simulation of the 18 July 2013 debris-flow event: **(a)** Very High Hazard sediment source areas (MPI > 0.47) identified by **D'Agostino and Bertoldi** (**2014**) together with the polygonal initiation area proposed by **Finis et al.** (**2017**); **(b)** final release area obtained after intersecting the two datasets and adopted in the present study. 49
4.5 Preparation of the topographic input data: **a** Extent of the LiDAR survey, Gadria catchment and modeling domain; **(b)** Detail of the selected area showing missing elevation data. 50
4.6 Mesh sizing regions adopted for the generation of the mesh. The figure shows the outer boundary of the computational domain together with the three areas assigned different target mesh sizes. 53
4.7 Computational mesh adopted for the numerical simulation of the 18 July 2013 event: **(a)** Overview of the unstructured triangular mesh over the computational domain; **(b)** detail of the transition between different mesh size regions; **(c)** detail of the transition between the outer boundary and the deposition basin mesh size region. 54
4.8 Barrier and opening footprints adopted for the representation of the open filter check dam in the computational mesh with indication of the deposition basin contour used for the sizing of the mesh. 55
4.9 Longitudinal section of the barrier embedded in the original topography. . 56
4.10 Three-dimensional view of the modeled check dam embedded in the topography: **(a)** closed barrier configuration; **(b)** open barrier configuration. 57

4.11 Identification of the source area adopted for the numerical simulation of the 26 July 2019 debris-flow event: **(a)** map of the Gadria catchment with details regarding instruments location at the lower station and contour of the zone that identifies the upper station (**Marchi et al., 2023**); **(b)** overview of the Gadria catchment with identification of the the upper station zone contour, the main channel and its tributary and the source area for the 2019 event. 59

5.1 Preliminary analysis of the numerical response obtained from sampling areas centered at the actual monitoring sensor locations for the 18 July 2013 event, with comparison against recorded flow depth : **(a)** maximum sampled flow depth at D3; **(b)** maximum sampled flow velocity at D3; **(c)** maximum sampled flow depth at D2; **(d)** maximum sampled flow velocity at D2. 63

5.2 Location of the D3 and D2 monitoring sections and local channel topography: **(a)** overview of the instrumented channel reach; **(b, c)** detail of the original and upstream-shifted stage radar sensors and their relative sampling areas respectively at D3 and D2; **(d, e)** corresponding longitudinal elevation profiles highlighting the position of the local topographic steps and stage radar sensors position. 64

5.3 Preliminary analysis of the numerical response obtained from sampling area shifted upstream of the monitoring sensor locations for the 18 July 2013 event, with comparison against recorded flow depth: **(a)** maximum sampled flow depth upstream of D3; **(b)** maximum sampled flow velocity upstream of D3; **(c)** maximum sampled flow depth upstream of D2; **(d)** maximum sampled flow velocity upstream of D2. 65

5.4 Parametric analysis of the numerical response obtained from sampling areas centered at the actual monitoring sensor locations for the 18 July 2013 event varying μ at fixed ξ, with comparison against recorded flow depth: **(a)** maximum sampled flow depth at D3; **(b)** maximum sampled flow velocity at D3; **(c)** maximum sampled flow depth at D2; **(d)** maximum sampled flow velocity at D2. 67

5.5 Parametric analysis of the numerical response obtained from sampling areas shifted upstream of the monitoring sensor locations for the 18 July 2013 event varying μ at fixed ξ, with comparison against recorded flow depth : **(a)** maximum sampled flow depth upstream of D3; **(b)** maximum sampled flow velocity upstream of D3; **(c)** maximum sampled flow depth upstream of D2; **(d)** maximum sampled flow velocity upstream of D2. . . 68

5.6 Parametric analysis of the numerical response obtained from sampling areas centered at the actual monitoring sensor locations for the 18 July 2013 event varying ξ at fixed μ, with comparison against recorded flow depth : **(a)** maximum sampled flow depth at D3; **(b)** maximum sampled flow velocity at D3; **(c)** maximum sampled flow depth at D2; **(d)** maximum sampled flow velocity at D2. 69
5.7 Parametric analysis of the numerical response obtained from sampling areas shifted upstream of the monitoring sensor locations for the 18 July 2013 event varying ξ at fixed μ, with comparison against recorded flow depth : **(a)** maximum sampled flow depth upstream of D3; **(b)** maximum sampled flow velocity upstream of D3; **(c)** maximum sampled flow depth upstream of D2; **(d)** maximum sampled flow velocity upstream of D2. . . 70
5.8 Comparison of the numerical response obtained from sampling areas centered at the actual monitoring sensor locations against recorded flow depth for the 18 July 2013 event considering $\mu = 0.08$ and $\xi = 500$ m/s^2: **(a)** maximum sampled flow depth at D3; **(b)** maximum sampled flow velocity at D3; **(c)** maximum sampled flow depth at D2; **(d)** maximum sampled flow velocity at D2. 72
5.9 Comparison of the numerical response obtained from sampling areas shifted upstream of the monitoring sensor locations against recorded flow depth for the 18 July 2013 event considering $\mu = 0.08$ and $\xi = 500$ m/s^2: **(a)** maximum sampled flow depth upstream of D3; **(b)** maximum sampled flow velocity upstream of D3; **(c)** maximum sampled flow depth upstream of D2; **(d)** maximum sampled flow velocity upstream of D2. 73
5.10 Three-dimensional view of the final flow-depth distribution within the retention basin for the 18 July 2013 event: **(a)** closed barrier configuration; **(b)** open barrier configuration. 74
5.11 Plan view of the final flow-depth distribution within the retention basin for the 18 July 2013 event: **(a)** closed barrier configuration; **(b)** open barrier configuration. 75
5.12 Maximum flow depth reached during the simulation of the 18 July 2013 event for (a) the closed and (b) the open barrier configuration. 76
5.13 Maximum flow velocity reached within the retention basin during the simulation of the 18 July 2013 event for (a) the closed and (b) the open barrier configuration. 77
5.14 Comparison of the numerical response obtained from sampling areas centered at the actual monitoring sensor locations against recorded flow depth for the 26 July 2019 event using the rheological parameters calibrated on the 2013 event: **(a)** maximum sampled flow depth at D3; **(b)** maximum sampled flow velocity at D3; **(c)** maximum sampled flow depth at D2; **(d)** maximum sampled flow velocity at D2. 78

5.15 Comparison of the numerical response obtained from sampling areas shifted upstream of the monitoring sensor locations against recorded flow depth for the 26 July 2019 event using the rheological parameters calibrated on the 2013 event: **(a)** maximum sampled flow depth upstream of D3; **(b)** maximum sampled flow velocity upstream of D3; **(c)** maximum sampled flow depth upstream of D2; **(d)** maximum sampled flow velocity upstream of D2. 79
5.16 Comparison of the numerical response at monitoring section D4 against the recorded flow depth for the 26 July 2019 event using the rheological parameters calibrated on the 2013 event: **(a)** maximum sampled flow depth at D4; **(b)** maximum sampled flow velocity at D4. 80

A.1 Preliminary analysis of the numerical response obtained from sampling areas centered at the actual monitoring sensor locations for the 18 July 2013 event, with comparison against recorded flow depth: **(a)** mean sampled flow depth at D3; **(b)** mean sampled flow velocity at D3; **(c)** mean sampled flow depth at D2; **(d)** mean sampled flow velocity at D2. 86
A.2 Preliminary analysis of the numerical response obtained from sampling areas shifted upstream of the monitoring sensor locations for the 18 July 2013 event, with comparison against recorded flow depth: **(a)** mean sampled flow depth upstream of D3; **(b)** mean sampled flow velocity upstream of D3; **(c)** mean sampled flow depth upstream of D2; **(d)** mean sampled flow velocity upstream of D2. 87
A.3 Parametric analysis of the numerical response obtained from sampling areas centered at the actual monitoring sensor locations for the 18 July 2013 event varying μ at fixed ξ, with comparison against recorded flow depth: **(a)** mean sampled flow depth at D3; **(b)** mean sampled flow velocity at D3; **(c)** mean sampled flow depth at D2; **(d)** mean sampled flow velocity at D2. 88
A.4 Preliminary analysis of the numerical response obtained from sampling areas shifted upstream of the monitoring sensor locations for the 18 July 2013 event varying μ at fixed ξ, with comparison against recorded flow depth : **(a)** mean sampled flow depth upstream of D3; **(b)** mean sampled flow velocity upstream of D3; **(c)** mean sampled flow depth upstream of D2; **(d)** mean sampled flow velocity upstream of D2. 89
A.5 Parametric analysis of the numerical response obtained from sampling areas centered at the actual monitoring sensor locations for the 18 July 2013 event varying ξ at fixed μ, with comparison against recorded flow depth : **(a)** mean sampled flow depth at D3; **(b)** mean sampled flow velocity at D3; **(c)** mean sampled flow depth at D2; **(d)** mean sampled flow velocity at D2. 90

A.6 Parametric analysis of the numerical response obtained from sampling areas shifted upstream of the monitoring sensor locations for the 18 July 2013 event varying ξ at fixed μ, with comparison against recorded flow depth : **(a)** mean sampled flow depth upstream of D3; **(b)** mean sampled flow velocity upstream of D3; **(c)** mean sampled flow depth upstream of D2; **(d)** mean sampled flow velocity upstream of D2. 91
A.7 Comparison of the numerical response obtained from sampling areas centered at the actual monitoring sensor locations against recorded flow depth for the 18 July 2013 event considering $\mu = 0.08$ and $\xi = 500$ m/s^2: **(a)** mean sampled flow depth at D3; **(b)** mean sampled flow velocity at D3; **(c)** mean sampled flow depth at D2; **(d)** mean sampled flow velocity at D2. 92
A.8 Comparison of the numerical response obtained from sampling areas shifted upstream of the monitoring sensor locations against recorded flow depth for the 18 July 2013 event considering $\mu = 0.08$ and $\xi = 500$ m/s^2: **(a)** mean sampled flow depth upstream of D3; **(b)** mean sampled flow velocity upstream of D3; **(c)** mean sampled flow depth upstream of D2; **(d)** mean sampled flow velocity upstream of D2. 93
A.9 Comparison of the numerical response obtained from sampling areas centered at the actual monitoring sensor locations against recorded flow depth for the 26 July 2019 event using the rheological parameters calibrated on the 2013 event: **(a)** mean sampled flow depth at D3; **(b)** mean sampled flow velocity at D3; **(c)** mean sampled flow depth at D2; **(d)** mean sampled flow velocity at D2. 94
A.10 Comparison of the numerical response obtained from sampling areas shifted upstream of the monitoring sensor locations against recorded flow depth for the 26 July 2019 event using the rheological parameters calibrated on the 2013 event: **(a)** mean sampled flow depth upstream of D3; **(b)** mean sampled flow velocity upstream of D3; **(c)** mean sampled flow depth upstream of D2; **(d)** mean sampled flow velocity upstream of D2. 95
A.11 Comparison of the numerical response at monitoring section D4 against the recorded flow depth for the 26 July 2019 event using the rheological parameters calibrated on the 2013 event: **(a)** mean sampled flow depth at D4; **(b)** mean sampled flow velocity at D4. 96

List of Tables

2.1 Volume classification of landslides (**Fell**, **1994**). 5
2.2 Abbreviated classification of landslides (**Cruden and Varnes**, **1996**). . . . 6

3.1 Debris-flow events recorded at the Rio Gadria monitoring site between 2011 and 2024. 29

4.1 Target mesh sizes adopted in the computational domain. 52

5.1 Numerical travel times of the debris-flow peak between D3 and D2 and corresponding mean propagation velocities for the investigated Voellmy parameter combinations. 71
5.2 Comparison between numerical and experimental mean propagation velocities along the D4–D3 and D3–D2 channel reaches for the 26 July 2019 event. Numerical velocities were estimated from the travel times of the corresponding simulated flow-depth peaks. 81

1 Introduction

Mountain environments are particularly sensitive to the effects of climate change, with important implications for natural hazards and risk management. Variations in precipitation regimes are among the most relevant consequences, as heavy rainfall events have intensified over many land regions and are projected to become more frequent and intense with increasing global warming (**IPCC**, **2021**). At the same time, rising temperatures contribute to glacier retreat and permafrost degradation in high-mountain regions, with potential consequences for slope stability and sediment availability (**Hock et al.**, **2019**). The combined effects of these processes can influence the occurrence and characteristics of gravity-driven processes, making their assessment increasingly relevant in Alpine environments.

Among gravity-driven processes affecting mountain environments, shallow landslides are particularly relevant because they can evolve into highly mobile flow-like movements. Rainfall represents one of the main triggering factors of shallow slope failures, as water infiltration can progressively modify the hydrological and mechanical conditions, eventually leading to the mobilization of superficial material. After failure, the mobilized mass may evolve into a flow-like movement, whose characteristics depend on the nature of the material involved and on the conditions governing its propagation (**Cruden and Varnes**, **1996**; **Ahmadi-Adli**, **2014**). Among these phenomena, debris flows represent a major hazard in steep mountain catchments because of their rapid propagation, high sediment concentration and high mobility, which allow them to transport large volumes of material over relatively short periods of time and travel considerable distances. During their propagation, they can reach downstream areas, potentially causing severe damage to settlements and infrastructure and posing a significant threat to human life (**Iverson**, **1997**; **Hungr et al.**, **2001**).

Understanding how debris flows propagate and which areas may be affected is a key aspect of hazard assessment and risk mitigation. Runout analysis allows investigating the propagation and deposition phases of the mobilized mass after triggering, providing an estimate of the potential travel distance, spatial extent, flow depth and velocity. These quantities are particularly relevant for hazard zoning, land-use planning and evaluation and design of mitigation measures (**Jakob and Hungr**, **2005**; **McDougall**, **2017**). Different approaches can be adopted to investigate debris-flow runout, ranging from empirical and analytical methods to numerical models (**Hürlimann et al.**, **2008**; **McDougall**, **2017**). Among these, numerical modeling represents a valuable tool for investigating flow propagation and deposition over complex topographies. In particular, depth-averaged continuum

models provide an useful compromise between computational effort and an adequate representation of the main characteristics of flow propagation (**Pirulli**, **2005**; **McDougall**, **2017**).

The reliability of numerical simulations strongly depends on the assumptions adopted to represent the behavior of the flowing mass and the resistance mechanisms governing its propagation. In depth-averaged models, these mechanisms are described through rheological formulations, whose parameters can significantly influence the simulated flow dynamics (**Pirulli**, **2005**; **Pirulli and Mangeney**, **2008**). Their calibration against observations from real events therefore represents an important aspect of debris-flow modeling. In this context, permanently instrumented catchments are particularly valuable, as continuous monitoring data provide a direct basis for comparing numerical and observed flow response.

The Rio Gadria catchment, located in the Autonomous Province of Bolzano in the Italian Alps, provides a suitable setting for this purpose. A permanent monitoring system has been operating in the basin since 2011, allowing several debris-flow events to be recorded through complementary meteorological, hydrological and flow-monitoring instruments (**Comiti et al.**, **2014**). The availability of observations from different events provides the opportunity to calibrate the numerical model against a documented debris flow and to subsequently assess the transferability of the calibrated parameters to another event occurring within the same catchment.

Within this context, the present thesis focuses on the numerical modeling of two debris-flow events recorded in the Rio Gadria catchment, with the main objective of investigating the calibration and transferability of rheological parameters using the monitoring data available for the site. Numerical analyses are performed using RASH3D, a depth-averaged continuum model developed for the runout simulation of rapid flow-like landslides over complex three-dimensional topographies (**Pirulli**, **2005**). The behavior of the moving mass is represented through the Voellmy rheological law, which combines frictional and turbulent resistance mechanisms.

The debris-flow event of 18 July 2013 is selected as the benchmark event for the development and calibration of the numerical model. The model setup requires the definition of the initial source area, the preparation of the topographic input data and the generation of a computational mesh, with different levels of refinement according to the characteristics of the investigated areas. A parametric analysis is then performed by varying the two parameters of the Voellmy rheology. The numerical response is evaluated at the locations of the monitoring sections and compared with the flow-depth hydrographs recorded during the event. Both flow depth and propagation velocity are considered in the interpretation of the numerical response, allowing to identify a parameter combination providing a satisfactory overall reproduction of the monitored event.

Following the calibration of the rheological parameters, the analysis focuses on flow propagation and deposition within the retention basin. Particular attention is devoted to

the interaction between the simulated debris flow and the open filter check dam located downstream of the basin. Two configurations of the filter check dam are investigated: a closed configuration with a continuous barrier and an open configuration reproducing its central slit. Their comparison allows to investigate the influence of the opening on flow propagation and final deposition within the basin.

The second part of the study focuses on the debris-flow event of 26 July 2019. The rheological parameters calibrated for the 2013 benchmark event are applied without further adjustment, and the resulting numerical response is compared with the available monitoring observations. The analysis aims to assess if the parameter combination identified from the back-analysis of a single event can also reproduce the flow dynamics of a different debris flow occurring within the same catchment. The comparison therefore provides the basis for discussing the transferability of the calibrated rheological parameters and the limitations associated with their direct application under different event conditions.

The thesis is organized into six chapters. Following this introduction, Chapter 2 provides the theoretical background required for the study, with particular attention to landslide classification, rainfall-induced shallow landslides, flow-like landslides, and debris-flow triggering and runout processes. Chapter 3 introduces the Rio Gadria catchment, describing its geological, geomorphological and climatic characteristics, the existing mitigation measures, the monitoring system and the debris-flow events considered in this work. Chapter 4 presents the RASH3D numerical framework and describes the development of the numerical models setup for the 2013 and 2019 events. Chapter 5 presents and discusses the numerical results, including the rheological calibration of the 2013 benchmark event, the analysis of flow propagation and deposition within the retention basin for different check-dam configurations for the 2013 debris flow, and the application of the calibrated parameters to the 2019 event. Finally, Chapter 6 summarizes the main conclusions of the study and outlines possible directions for future research.

2 From landslides to debris flows: classification, triggering mechanisms and flow dynamics

This chapter provides the theoretical background necessary to understand the processes investigated in this thesis. It begins with a general overview of landslides and their classification according to the main international classification systems. Particular attention is then given to shallow landslides and their initiation mechanisms, with a focus on rainfall as one of the most common triggering factors. The chapter subsequently examines the evolution of rainfall-induced shallow landslides during the runout phase, when they may transform into flow-like phenomena under favorable geomorphological and hydrological conditions. The main features of flow-like landslides are discussed, highlighting the transition from slides to flows. Finally, the chapter focuses on debris flows since they are the principal subject of this thesis, describing their characteristics, triggering and runout processes as a basis for the numerical modeling presented in the following chapters.

Before discussing landslide processes in detail, it is worth considering some general aspects related to natural slopes, since they are characterized by complex morphology and continuous spatial variability of their geological and geotechnical properties. A detailed geological, hydro-geological and geotechnical investigation is therefore needed to understand the physical and mechanical characteristics of the natural materials composing the slopes. The extension of the investigation must be proportional to the importance and impact of the problem under study also in economic terms. Natural slopes generally experience slower variations in loading conditions and geotechnical models can only provide a partial and approximate representation of physical reality, and are typically affected by a significantly high number of uncertainties (**Turner and Schuster**, **1996**; **Duncan et al.**, **2014**).

2.1 Classification of landslide phenomena

According to the definition proposed by **Cruden** (**1991**), a landslide is "the movement of a mass of rock, debris or earth down a slope". Soil and rock are the two main materials which can made a slope and they present a different behavior with respect to the possible instability. A slope is defined unstable when it is potentially or effectively subjected to any form of movement of soil or rock mass due to gravity or groundwater regime.

Landslides represent one of the major geotechnical hazards affecting mountainous regions. Slope failures constitute a complex problem involving a wide variety of geomaterials under different geological and climatic conditions, causing an environmental, economic and social impact (**Leroueil and Chandler**, **2001**). A more detailed definition of a landslide can be obtained by describing the characteristics of the movement, such as its type, volume, and velocity.

The typological classification is fundamental because later phases of hazard and risk analysis depend on it. Landslides include different types of slope failure, which can be distinguish according to the material involved, the volume associated to them, the related velocity, and the associated energy. Due to the complexity and variability of slope failure, several classification systems have been proposed over time.

A general classification based on the volume of the moved mass was proposed by **Fell** (**1994**), as shown in **Table 2.1**.

Table 2.1: Volume classification of landslides (**Fell**, **1994**).

Description	**Volume** [m^3]
Extremely small	$< 5 \times 10^2$
Very small	$5 \times 10^2 - 5 \times 10^3$
Small	$5 \times 10^3 - 5 \times 10^4$
Medium	$5 \times 10^4 - 5 \times 10^5$
Medium to large	$2.5 \times 10^5 - 1 \times 10^6$
Very large	$1 \times 10^6 - 5 \times 10^6$
Extremely large	$> 5 \times 10^6$

One of the most adopted classification system was introduced by **Varnes** (**1978**), who classified landslide according to type of movement and type of involved material. This classification system has been then review years later by **Cruden and Varnes** (**1996**) following practically the same framework, as shown in **Table 2.2**, where few terms were modified to define a precise and clear terminology for describing landslide phenomena.

Table 2.2: Abbreviated classification of landslides (**Cruden and Varnes**, **1996**).

TYPE OF MOVEMENT	**TYPE OF MATERIAL**		
		ENGINEERING SOILS	
	BEDROCK	*PREDOMINANTLY COARSE*	*PREDOMINANTLY FINE*
Fall	Rock fall	Debris fall	Earth fall
Topple	Rock topple	Debris topple	Earth topple
Slide	Rock slide	Debris slide	Earth slide
Spread	Rock spread	Debris spread	Earth spread
Flow	Rock flow	Debris flow	Earth flow

According to the type of material, rock refers to an intact and hard mass that stays in its natural position before failure, while soils consist of aggregates of mineral particles produced either by weathering of rock or by transport process. Depending on their grain-size distribution, soils are divided into earth and debris. Earth is composed by fine-grained material, with at least 80% of the particles smaller the 2 mm, whereas debris mainly consists of coarse material, with 20-80% of the particles exceeding 2 mm. With respect to the type of movement, landslides are classified according to the kinematics of the displaced mass, describing how movement develops within the unstable mass and providing important information on landslide behavior. According to this criterion, five principal types of movement are recognized as shown in **Figure 2.1**: fall, topple, slide, spread and flow (**Cruden and Varnes**, **1996**).

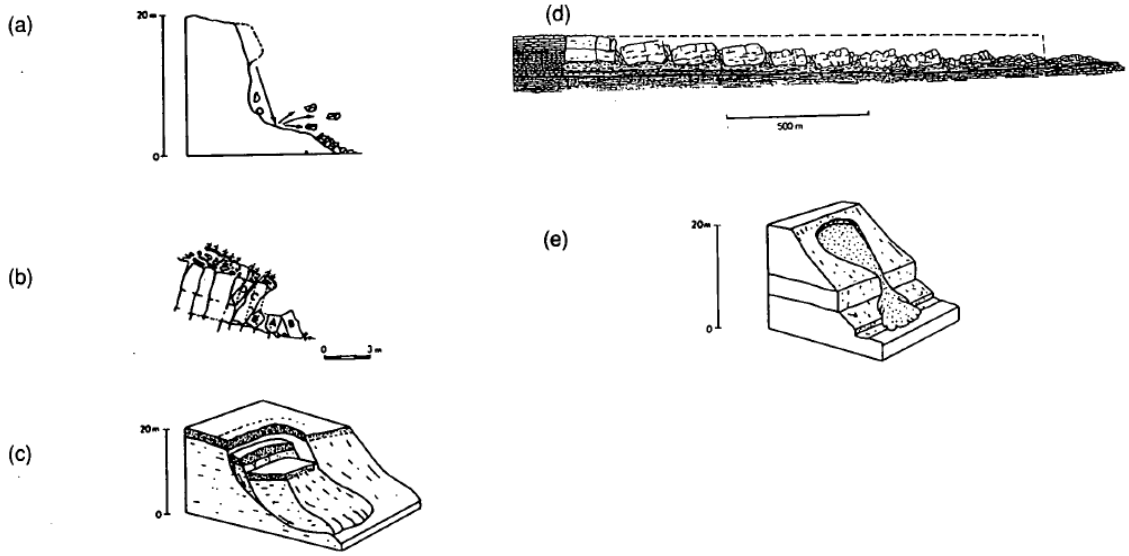


Figure 2.1: Types of landslides: **(a)** fall, **(b)** topple, **(c)** slide, **(d)** spread, **(e)** flow. Source: **Cruden and Varnes** (**1996**)

Cruden and Varnes (**1996**) also introduced a classification based on the velocity of the movement introducing seven classes that define the probable destructive power of landslides (**Figure 2.2** and **Figure 2.3**). This classification is important because it underlines that risk level is not just a function of the volume, but it must be combined with the intensity of the phenomenon.

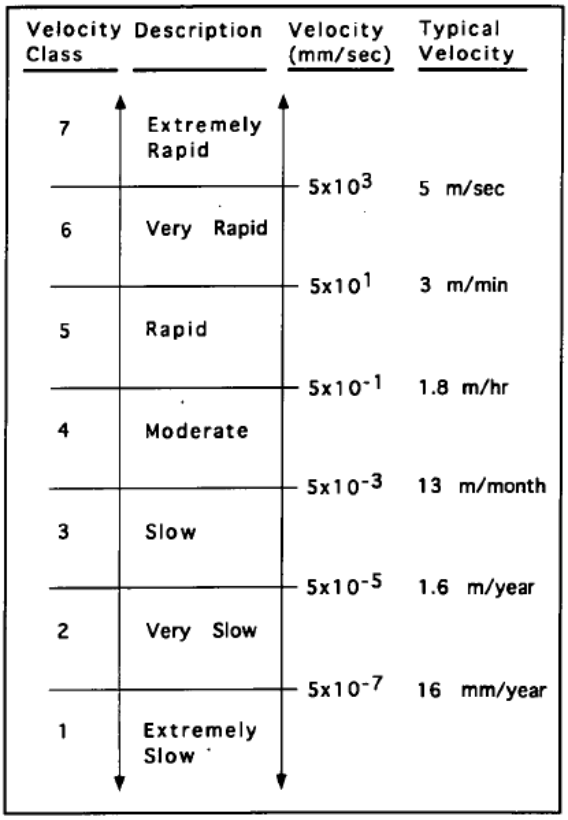


Figure 2.2: Classification based on the rate of movement and attribution of the velocity class (**Cruden and Varnes**, **1996**).

LANDSLIDE VELOCITY CLASS	PROBABLE DESTRUCTIVE SIGNIFICANCE
7	Catastrophe of major violence; buildings destroyed by impact of displaced material; many deaths; escape unlikely
6	Some lives lost; velocity too great to permit all persons to escape
5	Escape evacuation possible; structures, possessions, and equipment destroyed
4	Some temporary and insensitive structures can be temporarily maintained
3	Remedial construction can be undertaken during movement; insensitive structures can be maintained with frequent maintenance work if total movement is not large during a particular acceleration phase
2	Some permanent structures undamaged by movement
1	Imperceptible without instruments; construction possible with precautions

Figure 2.3: Definition of probable destructive significance of different velocity classes (**Cruden and Varnes**, **1996**).

While **Varnes** (**1978**) directly included complex landslides as a distinct category within his classification, **Cruden and Varnes** (**1996**) removed this category from the types of movement. Instead, the term complex was used to describe landslides that involve two or more movement types occurring in sequence, reflecting the fact that a landslide may evolve from an initial movement mechanism into another during their propagation as a consequence of changing mechanical and hydraulic conditions.

2.2 Factors controlling slope instability

Although slope instability is controlled by a combination of geological, geomorphological and hydrological conditions, the occurrence of slope failures depends on the interaction between precondition (or predisposing), preparatory and triggering factors, which constitute the main causes of landslide events (**Figure 2.4**). This classification follows the framework proposed by **Glade et al.** (**2005**). Predisposing factors are related to intrinsic characteristics of the slope and include:

- geological factors such as structural features (faults and fractures), position, schistosity, association and alternation between lithotypes, degradation, alteration, seismic and volcanic events;
- morphological factors related to slope inclination;
- hydro-geological factors involving superficial and underground water circulation, extent and distribution of interstitial pressures.

Preparatory factors are conditions or processes that progressively increase the susceptibility of a slope to instability. They do not immediately trigger the phenomenon, but reduce the

stability of the slope over time. Examples include deforestation, wildfire, climate change and weathering. Triggering factors are instead associated with external events that initiate the instability. Between them it is possible to find:

- climatic and vegetation factors, such as the alternation of long dry season and periods of intense and prolonged rainfall;
- human activity (e.g. excavations, vibrations and explosions);
- seismic and volcanic events.

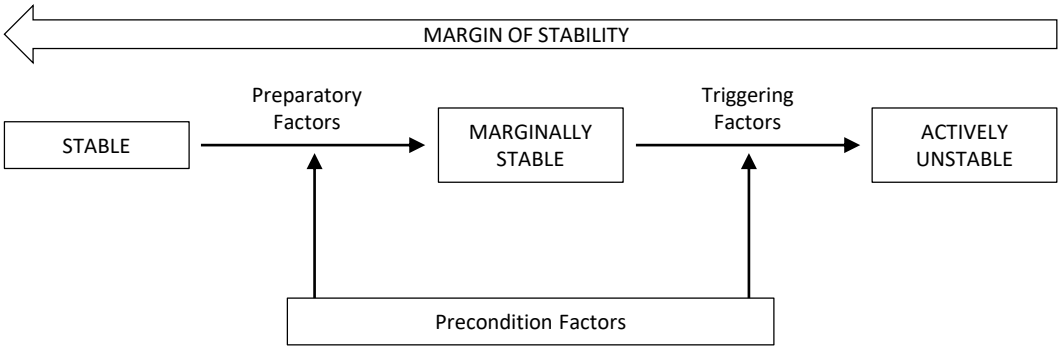


Figure 2.4: Schematization of destabilizing factors acting on a slope. Source: modified from **Glade et al.** (**2005**).

These factors act together to determine both the susceptibility of a slope to failure and the conditions leading to its initiation.

Rainfall events characterized by high intensity and/or prolonged duration represent one of the main triggering factors of shallow landslide in mountainous catchments, directly affecting surface runoff processes, erosion dynamics, and subsurface filtration. Through infiltration processes, rainfall alters the hydrological conditions of the slope, increasing pore-water pressures and reducing the shear strength of the soil. Rainfall-induced shallow landslides commonly represent the initiation mechanism of debris flows and for this reason are discussed in the following section.

2.3 Rainfall-induced shallow landslide

Rainfall-induced shallow landslides generally involve the detachment of a relatively thin layer of soil or weathered material resting on a more resistant substrate. From a physical point of view, rainfall infiltration into unsaturated soils leads to a progressive increase in water content, which subsequently induces a reduction in matric suction and effective stress. This process decreases the shear strength of the soil, progressively reducing the slope factor of safety (FS), defined as the ratio between resisting and driving forces, until failure occurs when the available resisting forces are exceeded (**Figure 2.5**). Since the failure surface usually develops within superficial soil deposits, these phenomena are commonly called shallow landslides (**Hatchinson**, **1988**; **Cruden and Varnes**, **1996**; **Iverson**, **2000**; **Ahmadi-Adli**, **2014**).

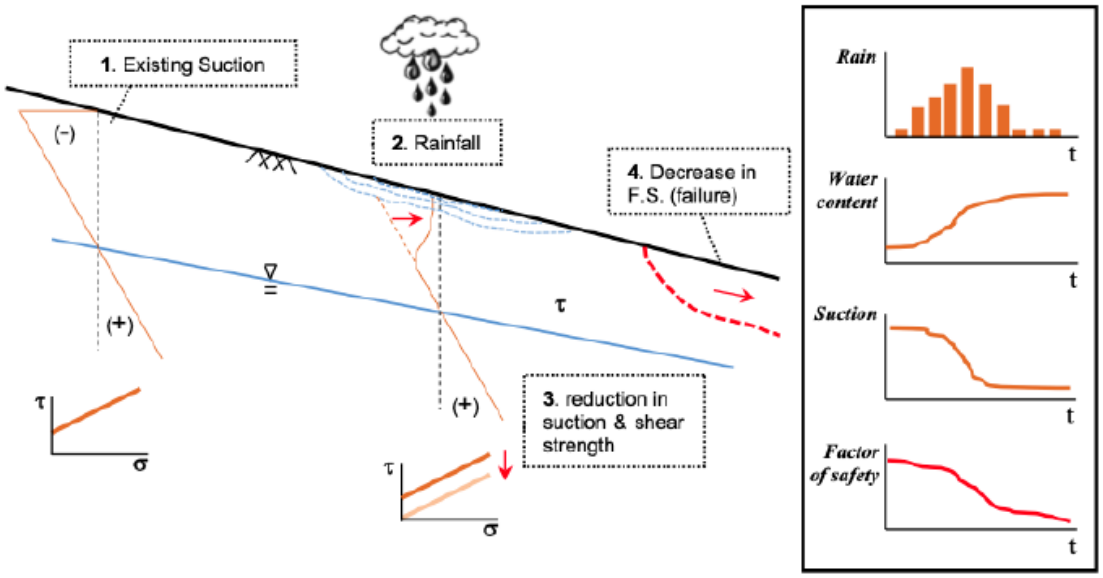


Figure 2.5: Conceptual representation of rainfall infiltration in unsaturated soils and its consequences (**Ahmadi-Adli**, **2014**).

Although shallow landslides may have different styles of movement, rainfall-induced failures most commonly start as translational slides and then under favorable topographic and hydrological conditions may subsequently evolve into a flow-like movement.

According to the classification proposed by **Varnes** (**1978**) and later revised by **Cruden and Varnes** (**1996**), slides are characterized by the downslope displacement of a soil or rock mass along a distinct failure surface or within a relatively thin shear zone. Depending on the geometry of the surface of rupture, slides are commonly divided into rotational and translational. While rotational slides develop along curved and concave failure surfaces, translational slides occur along planar or undulating surfaces of rupture, producing a predominantly translational displacement with limited internal rotation. Translational slides are generally shallower and frequently develop along pre-existing discontinuities or at the interface between different geological materials (**Cruden and Varnes**, **1996**).

Rainfall-induced shallow landslides commonly belong to this latter category because failure develops within the superficial soil cover, where infiltration processes are concentrated. Under favorable hydrological and topographic conditions, continued downslope displacement may progressively break up the internal structure of the sliding mass, especially when velocity or water content increases: the displaced material loses its original coherence and gradually evolves into a flow-like movement rather than remaining a coherent slide (**Cruden and Varnes**, **1996**). This transition provides the link between rainfall-induced shallow landslides and the flow-like phenomena discussed in the following section.

2.4 Flow-like landslides

Among the five types of movement recognized by **Cruden and Varnes** (**1996**), flows are of particular interest. Their propagation is mainly concentrated along the drainage paths of the hydrographic network, but may also extend in other directions. According to **Varnes** (**1978**), flow-type landslides occur in rock masses or loose soils and are characterized by continuous internal deformation of the displaced mass. During movement, the material behaves similarly to a viscous fluid due to the fluidizing action of water, whose presence often plays a key role in promoting its mobility. Deformation are not concentrated along a single rupture surface but are distributed through the moving mass by means of numerous evolving shear zones. The boundary between the moving and the stable material can be a well-defined surface or a zone of progressive shearing, where displacement gradually decreases. Flow-like landslides include a wide spectrum of phenomena characterized by different velocities, rheological behavior and mobility.

Hungr et al. (**2001**) proposed a modified framework specifically dedicated to flow-like landslides. The authors highlighted that classifications based on the observed movement type may be ambiguous, since the kinematics of a flow is often difficult to be reconstructed after the event. Their classification (**Figure 2.6**) therefore integrates additional criteria to better distinguish the different flow processes.

Material	Water Content[1]	Special Condition	Velocity	Name
Silt, Sand, Gravel, Debris (talus)	dry, moist or saturated	- no excess pore-pressure, - limited volume	various	Non-liquefied sand (silt, gravel, debris) flow
Silt, Sand, Debris, Weak rock[2]	saturated at rupture surface content	- liquefiable material[3], - constant water	Ex. Rapid	Sand (silt, debris, rock) flow slide
Sensitive clay	at or above liquid limit	- liquefaction *in situ*,[3] - constant water content[4]	Ex. Rapid	Clay flow slide
Peat	saturated	- excess pore-pressure	Slow to very rapid	Peat flow
Clay or Earth	near plastic limit	- slow movements, - plug flow (sliding)	< Rapid	Earth flow
Debris	saturated	- established channel[5], - increased water content[4]	Ex. Rapid	Debris flow
Mud	at or above liquid limit	-fine-grained debris flow	> Very rapid	Mud flow
Debris	free water present	- flood[6]	Ex. Rapid	Debris flood
Debris	partly or fully saturated	- no established channel[5], - relatively shallow, steep source	Ex. Rapid	Debris avalanche
Fragmented Rock	various, mainly dry	- intact rock at source, - large volume[7]	Ex. Rapid	Rock avalanche

[1] Water content of material in the vicinity of the rupture surface at the time of failure.
[2] Highly porous, weak rock (examples: weak chalk, weathered tuff, pumice).
[3] The presence of full or partial *in situ* liquefaction of the source material of the flow slide may be observed or implied.
[4] Relative to *in situ* source material.
[5] Presence or absence of a defined channel over a large part of the path, and an established deposition landform (fan). Debris flow is a recurrent phenomenon within its path, while debris avalanche is not.
[6] Peak discharge of the same order as that of a major flood or an accidental flood. Significant tractive forces of free flowing water. Presence of floating debris.
[7] Volume greater than 10,000 m^3 approximately. Mass flow, contrasting with fragmental rock fall.

Figure 2.6: Classification of flow-like landslides (**Hungr et al., 2001**).

Hungr et al. (**2001**) classify flow-like landslides based on:

- the type of material involved (**Figure 2.7**), emphasizing its formation processes rather than relying exclusively on grain-size criteria;
- velocity of the event, distinguishing slow-moving processes (e.g. earth flows) from extremely rapid phenomena such as debris flows, mud flows and debris avalanches;
- additional characteristics, including water content, event volume, the relationship between plasticity index and natural water content, the potential development of excess pore-water pressure, the presence of pre-existing paths or channels and the influence of flowing water.

Origin	Character	Condition[1]	Name
SORTED (marine, lacustrine, fluvial, eolian, volcanic, anthropogenic)	Non-cohesive (Plastic Limit < 5%)	Dry or Saturated	- Gravel - Sand - Silt
	Cohesive (Plastic Limit > 5%)	- Plastic (I_L< 0.5) - Liquid (I_L> 0.5)	- Clay - Sensitive Clay
UNSORTED (residual, colluvial, glacial, volcanic, anthropogenic)	Non-cohesive (Plastic Limit < 5%)	Dry or Saturated	- Debris[2]
	Cohesive (Plastic Limit < 5%)	- Plastic (I_L< 0.5) - Liquid (I_L> 0.5)	- Earth - Mud
PEAT	Organic	Saturated	- Peat
ROCK	Fragmented	Dry or Saturated	- Rock

[1] Related to the material found in the vicinity of the rupture surface at the time of failure, if it can be determined. In many cases, the material condition must be deduced from the behavior of the landslide, especially velocity.
[2] Debris may contain a considerable proportion of organic material.

Figure 2.7: Material involved in flow-like landslides (**Hungr et al., 2001**).

As shown in **Figure 2.6**, debris flows represent only one category within the broad group of flow-like landslides. Nevertheless, due to their high mobility, long runout distances and destructive potential, they are among the most hazardous flow processes. For this reason, the following section focuses specifically on debris flows, which are the focus of this thesis.

2.5 Definition and characteristics of debris flows

Among the different categories of flow-like landslides introduced in the previous section, debris flows are characterized by the movement of debris, which, according to **Hungr et al.** (**2001**), consists of loose material, which may be either saturated or dry depending on the conditions that precede failure. It may be produced by different geological and geomorphological processes, such as weathering, mass wasting, glacial transport, volcanic activity and anthropogenic waste. Debris can also contain organic material.

Debris flows are characterized by two distinct phases (**Figure 2.8**): the triggering (or detachment) process and the subsequent dynamic phase, commonly known as runout. The former takes place within the detachment zone and is driven by a combination of conditions that lead to failure once the internal shear strength of the material is exceeded, thus initiating the instability. The latter concerns the propagation and deposition stages (**Jakob and Hungr**, **2005**).

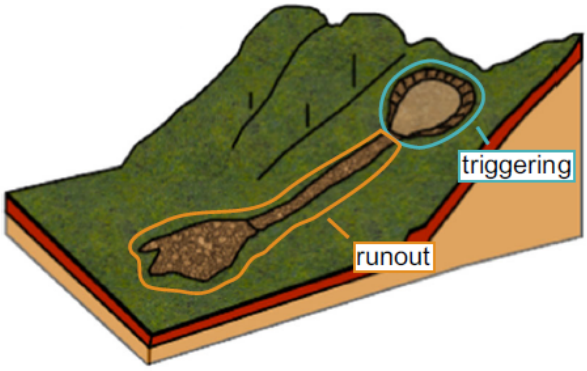


Figure 2.8: Schematic representation of the triggering and runout phases. Source: modified from **La Porta et al.** (**2024**).

One of the most distinctive characteristics of debris flows is the simultaneous interaction between solid and fluid phase. As highlighted by **Iverson** (**1997**), their behavior cannot be explained considering only grain interactions or only fluid forces, but the motion results from the combined action of both components. This interaction explains both the mobility of debris flows and their destructive capacity, allowing them to transport coarse material over long distances while generating high impact forces on possible obstacles along their path.

The triggering and runout phases are addressed individually in the following subsections, where the main processes and factors governing each phase are discussed.

2.5.1 Triggering analysis

Identifying the areas potentially affected by slope failure represents a fundamental step in the assessment of debris-flow initiation. Different approaches have been developed to identify the portions of a catchment that are more prone to instability, each relying on different assumptions and levels of complexity. According to **Guzzetti et al.** (**1999**), these approaches can be grouped into five main categories: geomorphological mapping, landslide inventory analysis, heuristic or index-based approaches, physically-based methods, and statistical approaches. The main characteristics of these approaches are summarized below:

- geomorphological mapping relies on the interpretation of geomorphological evidence by experienced investigators to identify existing and potential slope instability conditions;
- landslide inventory analysis infers future instability from the spatial distribution of past and present landslides, assuming that previous failures provide useful information on future occurrences;
- heuristic or index-based approaches assign relative weights to the known factors that control slope instability on the basis of their importance in causing slope failure. Their reliability depends on investigators knowledge and their field experience;
- physically-based methods simulate the mechanical and hydrological processes governing slope failure through geotechnical and hydrological models;

- statistical approaches establish empirical relationships between past landslide occurrences and the variables that control slope instability to estimate the spatial probability of future failures.

Despite their methodological differences, these approaches generally rely on the assumption that future slope failures are more likely to occur under conditions similar to those associated with past and present instability (**Guzzetti et al.**, **1999**).

2.5.2 Runout analysis

During the runout phase, the mobilized mass interacts directly with the slope along the propagation zone until deposition occurs. This phase governs the post-failure evolution of the phenomenon, determining the potential travel distance, the impacted areas, and the overall characteristics of the flow in terms of volume, velocity, and energy (**Jakob and Hungr**, **2005**).

Debris flows are very rapid to extremely rapid flows that typically propagate along pre-existing steep and confined channels, progressively entraining water and sediments from the bed and banks of the channel. (**Hungr et al.**, **2001**; **Hungr et al.**, **2014**). This process may increase the volume of the flowing mass and strongly influences the magnitude of the event. During propagation, debris flows commonly present one or more surges characterized by fronts rich of boulders and coarser material followed by a finer and more fluid tail (**Figure 2.9**). As described by **Hungr** (**2000**) the flow rapidly segregates into distinct phases and the surge wave can be structurally subdivided into three main elements:

- the front which is located at the advanced edge of the flow. It's predominantly composed of a highly unsaturated accumulation of coarse boulders. This coarse front induces the highest shear stress on the channel bed, acting as the primary agent for sediment entrainment and bed erosion;
- the body (or central part) which represents the core of the moving mass, where the flow reaches its maximum development. Here, the material exhibits a smaller, finer grain size compared to the front, and the mixture seams to have a hyperconcentrated fluid behavior. Within this zone, the initial stages of deposition begin to take place;
- the tail which is the final portion of the flow, characterized by a progressively diluted and lower-energy flow, which leads to the eventual deposition of the material on the debris fan.

Once the flow reaches less steep areas, boulders and coarse material may deposit, often forming lateral levees, while more fluid and finer fraction continues to propagate downstream (**Hungr et al.**, **2001**; **Hungr et al.**, **2014**).

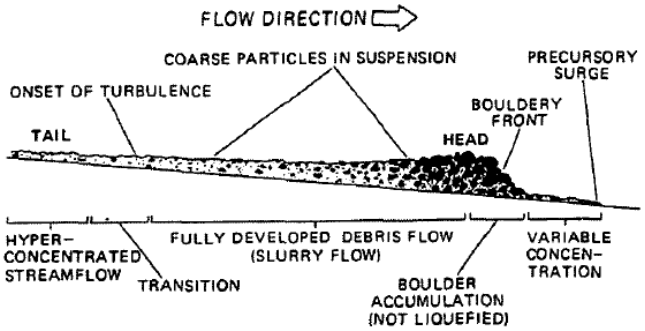


Figure 2.9: Scheme of a surge wave of a debris flow (**Hungr et al.**, **2001**).

The prediction of debris-flow propagation represents a fundamental component of hazard and risk assessment. Because these phenomena can travel at high velocities and impact areas located far from the initiation zone, runout analysis is used both to reconstruct past events (back-analysis) and to predict the behavior of potential future ones (forward-analysis). These analyses support hazard zoning, land-use planning and the design of mitigation measures such as barriers and retention structures (**McDougall**, **2017**).

Debris-flow runout can be investigated using different approaches, which can be classified into different categories: empirical methods, analytical methods, simple flow-routing methods, and numerical methods (**Hürlimann et al.**, **2008**; **McDougall**, **2017**). The main characteristics of these approaches are summarized below:

- empirical models are useful to have a preliminary indication of what is expected. They are not based on mathematical formulation but they are just an interpretation of documented debris-flow events and empirical correlations depend on the set of events (e.g. geographical area, type and number of events);
- analytical models are based on simplified description of flow motion using idealized geometry and assumptions. They are not able to provide information on time-dependent and space-dependent properties of the event;
- simple flow-routing methods estimate the propagation path of a debris flow by routing over a digital elevation model (DEM) according to topographic gradients. These approaches generally rely on single or multiple-flow direction algorithms to identify the most probable flow trajectories. Owing to their computational efficiency, they are particularly suitable for preliminary hazard mapping, although they do not explicitly reproduce the physical processes that govern debris-flow propagation;
- numerical methods solve the governing equations of mass and momentum conservation that describe the motion of the flowing mass in order to simulate debris-flow propagation and deposition. They allow to pass from a multi-component model that accounts for water, fine and coarse grain material and other possible elements displaced by the moving mass, to a discrete ensemble of particles or to an equivalent continuum fluid, trying find the most realistic representation of the phenomena respectively through a discrete or continuum model. The latter can be further distinguished according to the adopted modeling framework into depth-averaged models and three-dimensional models. The former are based on the vertical integration of the governing

conservation equations over the flow depth, reducing the three-dimensional problem to two spatial dimensions. This simplification considerably decreases the computational effort while preserves an accurate representation of debris-flow propagation over a complex topography. The latter solve the governing equations throughout the entire flow volume, providing a more detailed representation of the internal flow dynamics and allowing flow–obstacle interactions to be reproduced more realistically. Their higher computational effort generally limits their application to detailed local-scale analyses.

Within numerical approaches, different modeling frameworks can also be coupled to combine their respective capabilities. Examples include the coupling of continuum and discontinuum models to account for different aspects of debris-flow behavior (**McDougall**, **2017**).

Among these formulations, depth-averaged models have become one of the most widely adopted approaches for debris-flow runout simulations because they provide an effective compromise between computational effort and predictive capability over complex terrain. The modeling framework adopted in this thesis belongs to this category and is presented in detail in Chapter 4.

3 Case study

3.1 Geographical framework

The Rio Gadria catchment is located in the Upper Val Venosta, in the Autonomous Province of Bolzano–South Tyrol, northern Italy (**Figure 3.1**).

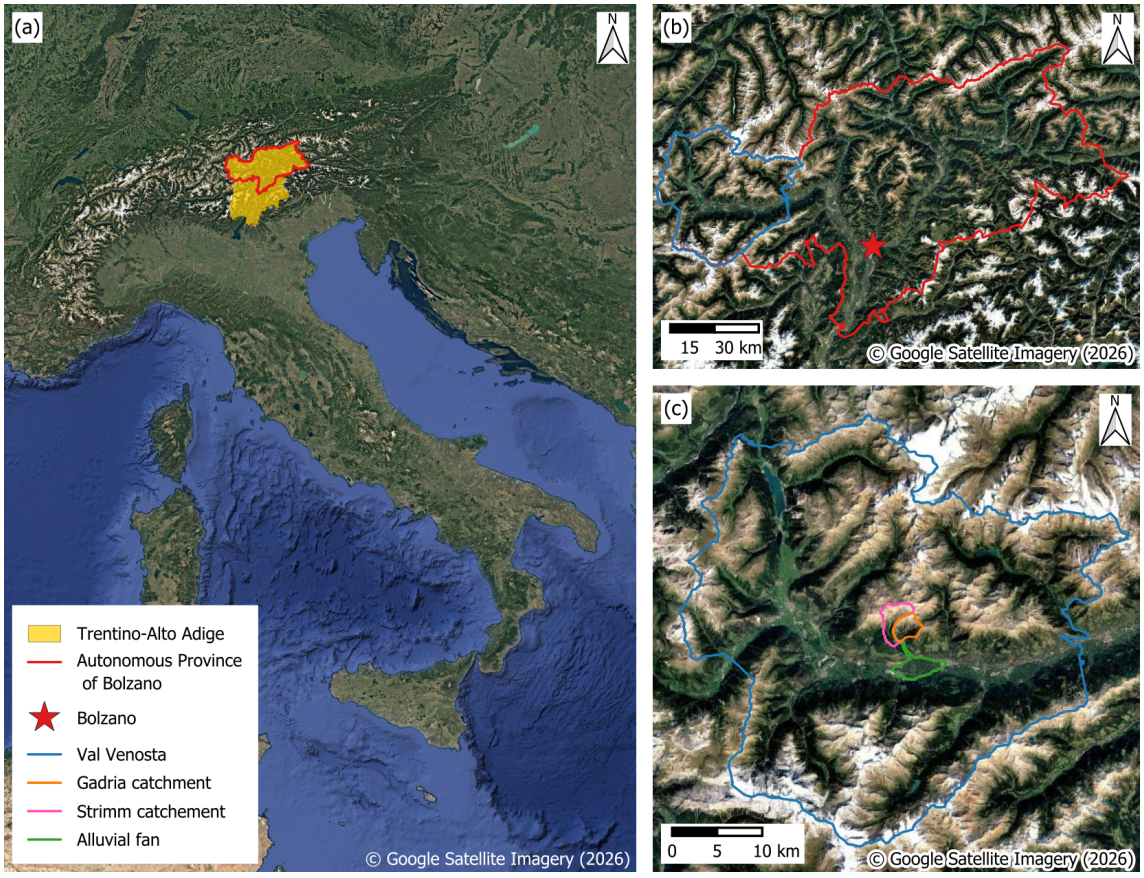


Figure 3.1: Geographical context of the study area. **(a)** Trentino Alto-Adige region and Autonomous Province of Bolzano; **(b)** Autonomous Province of Bolzano showcasing the Val Venosta area; **(c)** detailed view of Val Venosta, emphasizing Gadria catchment, Strimm basin and alluvial fan at the confluence between the two.

The basin covers an area of approximately 6.3 km^2 and extends from 1,394 m to 2,945 m above sea level (**Figure 3.2**). The catchment is characterized by particularly steep terrain, with an average slope exceeding 79% (**Figure 3.3**), which strongly influences the formation of runoff, channel erosion, and the initiation of debris flows.

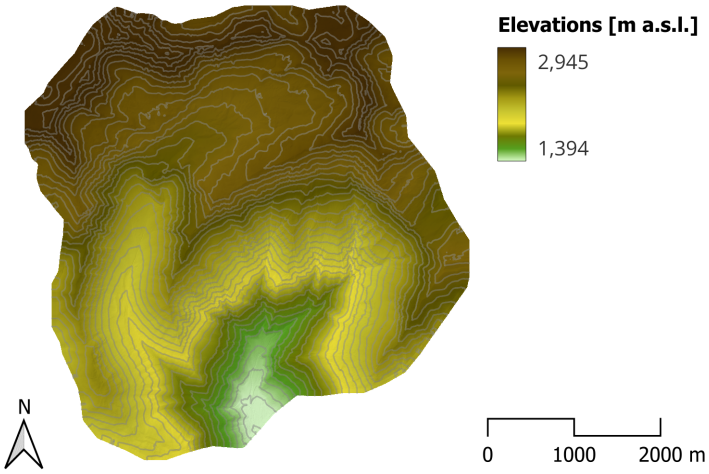


Figure 3.2: Altimetric map of the Rio Gadria basin.

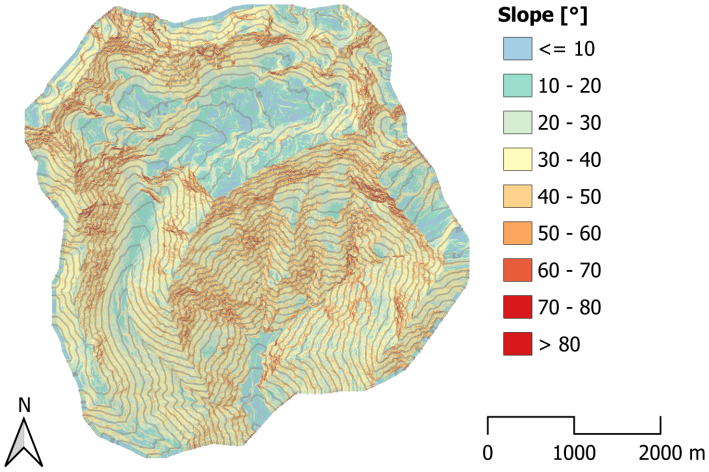


Figure 3.3: Slope map in degrees (°) of the Rio Gadria basin.

The adjacent Strimm basin (**Figure 3.1c**) occupies an area of approximately 8.5 km^2, reaches a maximum elevation of 3,197 m a.s.l., and exhibits an average slope of approximately 62%. The two streams converge near the apex of a large alluvial fan, covering approximately 10.9 km^2 (**Comiti et al., 2014**).

Despite their geographical proximity and similar climatic conditions, the two basins exhibit different morphology and sediment transport regimes. The Gadria catchment is characterized by frequent debris-flow activity along the main channel, while the Strimm basin is predominantly characterized by bedload transport processes, with debris flows occurring only occasionally in its steepest parts (**Cavalli et al., 2013**). In **Figure 3.4** it is possible to see in detail the two basins, the two main streams and the alluvial fan which includes the zone between the towns of Alliz, Lasa and Silandro.

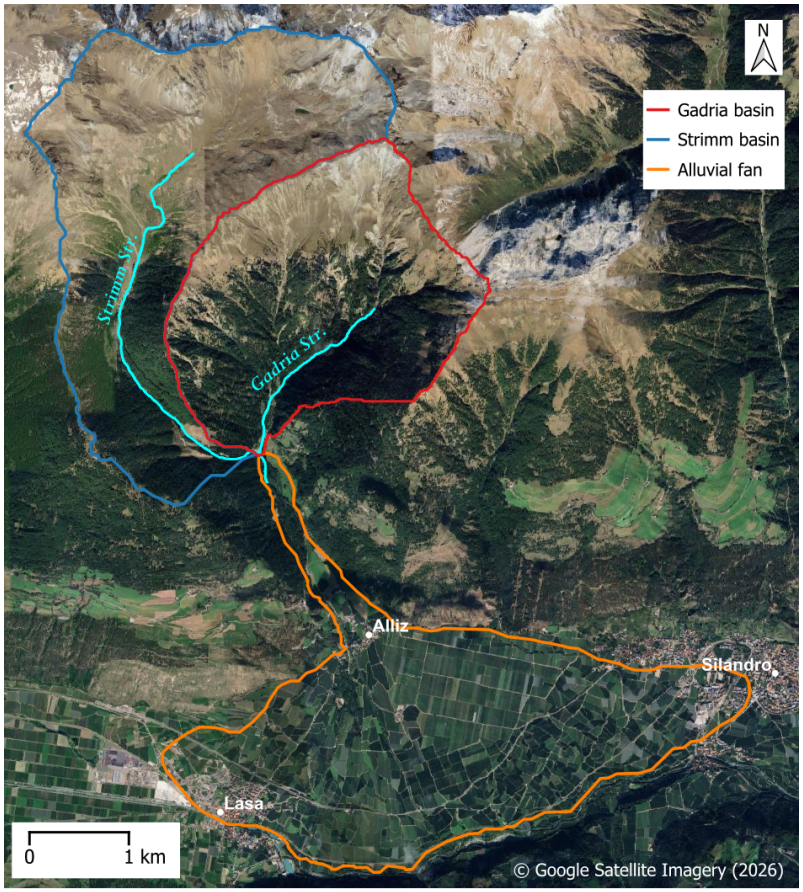


Figure 3.4: Map and location of the Gadria-Strimm catchments and their alluvial fan.

3.2 Geological and Geomorphological setting

3.2.1 Geological setting

The Gadria basin is located within the central sector of the Val Venosta, a glacial depression situated in the Austroalpine territory of the Eastern Alps. The geological framework of the area is controlled by the Venosta Shear Zone and it is predominantly composed of metamorphic rocks consisting mainly of gneiss and schist, with subordinate occurrences of amphibolites, orthogneiss and marble. The structural setting is strongly influenced by regional tectonic features and an extensive fracture network. These discontinuities strongly govern both the development of the drainage network and the strength of the rock mass, favoring the processes of weathering and slope instability. The catchment is predominantly underlain by paragneiss which is locally affected by pegmatitic intrusions and phyllonitic alteration zones associated with low-grade metamorphism. In the southern part of the basin, orthogneiss becomes progressively more dominant and exhibits a more pronounced mylonitic character toward the Venosta Shear Zone. The geological boundaries between these lithological units are often hidden by thick Quaternary sediment deposits that cover large portions of the catchment (**Comiti et al., 2014**).

3.2.2 Geomorphological characteristics

The geomorphological setting of the Rio Gadria catchment results from the interaction of glacial, periglacial, fluvial and slope-related processes. The basin is characterized by steep slopes, deeply incised channels and extensive sediment source areas which favor efficient sediment transfer from the hillslopes to the drainage network, contributing to the frequent occurrence of debris-flow activity (**Comiti et al.**, **2014**).

The development of current landscape has been strongly influenced by Quaternary glaciations. During the Last Glacial Maximum, the Adige Glacier occupied the Val Venosta, reaching its maximum extent approximately 17 thousand years ago. Subsequent deglaciation promoted the accumulation and remobilization of extensive glacial and glaciofluvial deposits, which still represent an important source of sediment within the catchment (**Brardinoni et al.**, **2018**).

A clear example of the ongoing paraglacial adjustment within the catchment is represented by the extensive kame terraces located in the upper part of the basin. These glacial deposits rest on highly weathered and fractured bedrock and have been subject to continuous erosion since glacier retreat. Their progressive dissection has led to the formation of steep gullies and badland-like topography, promoting intense erosion and sediment mobilization. The availability of large volumes of unconsolidated material from these deposits is considered a key factor controlling the high frequency of debris-flow activity in the Rio Gadria catchment (**Comiti et al.**, **2014**). **Figure 3.5** shows some views of the Gadria catchment.

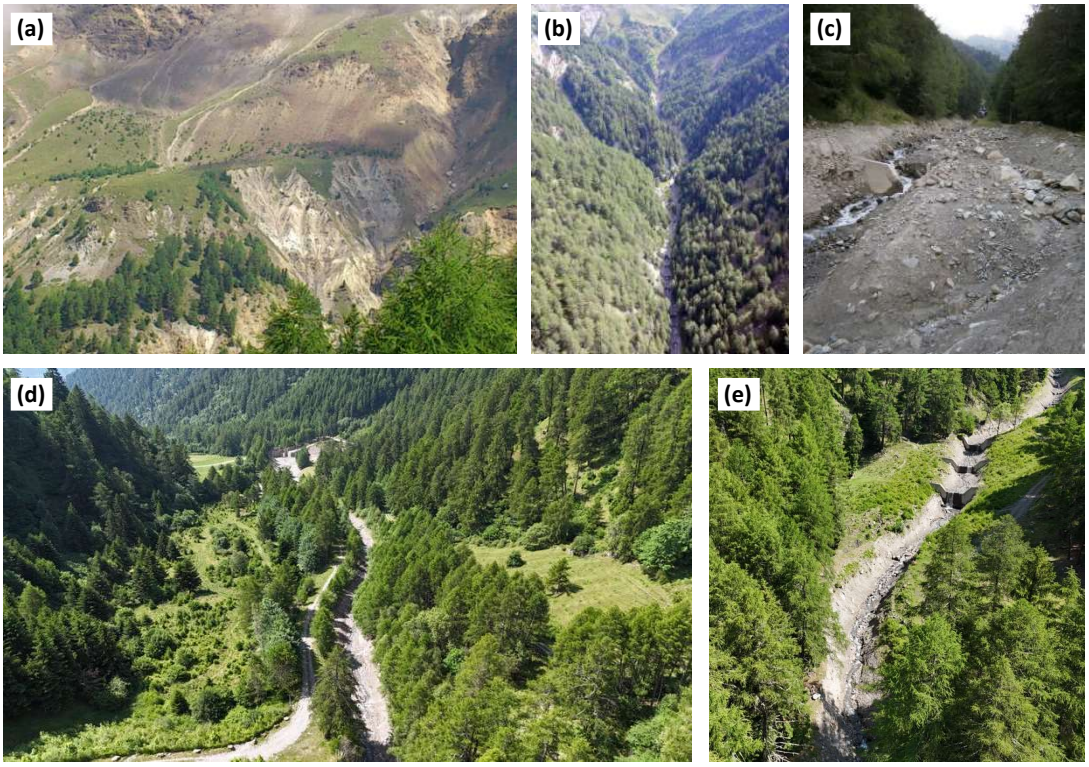


Figure 3.5: View of the Gadria basin: **(a)** kame terraces deposits (**Comiti et al.**, **2014**); **(b)** main channel in the upper part of the basin (**Comiti et al.**, **2014**); **(c)** main channel in the lower part of the basin within the instrumented part (**Comiti et al.**, **2014**); **(d)** main channel from above looking at the deposition basin (**Provincia Autonoma di Bolzano - Alto Adige**, **2026a**); **(e)** detail of the channel in the central part (**Provincia Autonoma di Bolzano - Alto Adige**, **2026a**).

Land cover within the catchment is highly heterogeneous and reflects the strong altitudinal and geomorphological gradients that characterize the basin, as shown in **Figure 3.6**. According to the land-use classification provided by **Provincia Autonoma di Bolzano - Alto Adige** (**2026a**), forest represents the dominant land-cover class, occupying approximately 47.5% of the catchment area. Grasslands account for 27.6%, while rocks and debris-covered zones are mainly concentrated in the upper sectors of the basin and respectively cover 6.5% and 15.5% of the total area. Zones classified as meadows and wooded pastures constitute only a minor fraction of the catchment, representing approximately 2.9%.

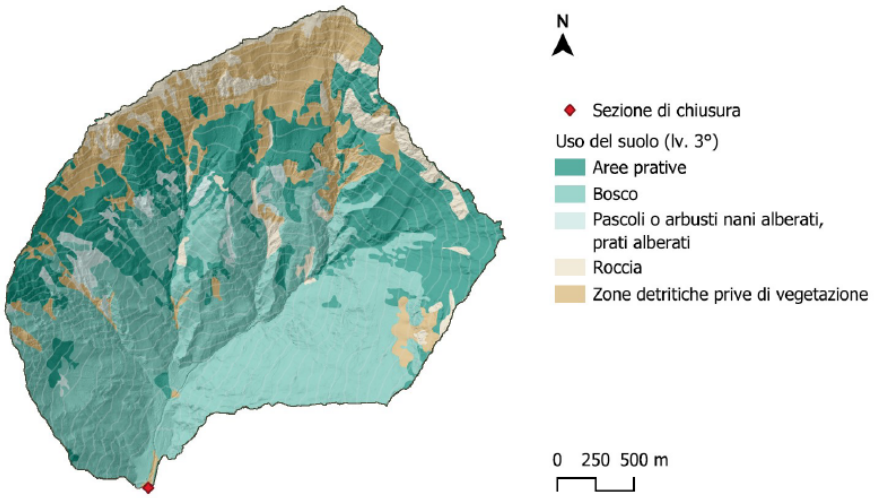


Figure 3.6: Land cover map of the Rio Gadria basin (**Bressan**, **2024**).

The spatial distribution of land-cover classes reflects the geomorphological organization of the basin. Forests and grasslands are mainly concentrated at lower elevations and on relatively stable slopes, whereas rock outcrops, debris deposits and vegetated surfaces prevail in the headwater areas. These upper sectors host many of the active sediment source areas that contribute to debris-flow initiation and sediment supply within the basin.

The pathways and efficiency of sediment transport within the catchment have been assessed through a geomorphometric analysis of spatial sediment connectivity (**Cavalli et al.**, **2013**). Compared with nearby basins, the Gadria catchment exhibits a relatively uniform pattern with an higher degree of connectivity in the upper parts of the basin itself. This configuration facilitates the rapid delivery of sediment through gullies and deeply incised channels, increasing the potential for debris-flow triggering and propagation.

Sediment originating in the Gadria basin is transported downstream and deposited in the alluvial fan described before. It belongs to a group of large Alpine alluvial fans whose origin can be attributed to the contribution of catastrophic slope failures, as well as to the long-term accumulation and redistribution of glacial and glaciofluvial deposits through debris flows and fluvial process (**Comiti et al.**, **2014**).

3.3 Climate characteristics of the basin

The Gadria basin is located within one of the driest inner-Alpine regions of the European Alps. The climatic conditions of the upper Val Venosta are strongly influenced by the surrounding mountains, which create a marked rain-shadow effect by limiting the penetration of both northern and southern moist air masses. As a consequence, precipitation at the valley floor are relatively low compared with other Alpine regions (**Comiti et al.**, **2014**).

Precipitation in the Gadria catchment exhibits a strong elevation dependency, progressively increasing with altitude. Mean annual precipitation increases from approximately 480 mm at the valley floor to about 662 mm at 1,754 m a.s.l. For the higher portions of the

basin (2,000–2,500 m a.s.l.), where many sediment source areas are located, mean annual precipitation is estimated to reach approximately 800–900 mm based on short records, although long-term observations are currently unavailable. The intensity of sub-daily extreme rainfall events is also strongly influenced by altitude. Snow cover generally lasts from mid-November until mid-April, contributing to the seasonal hydrological regime of the basin (**Comiti et al.**, **2014**; **Coviello et al.**, **2021**).

3.4 Debris-flow mitigation interventions

The Gadria catchment has been affected by debris-flow activity since several centuries. A historical and documentary investigation conducted by **Raich** (**2011**) identified 64 events between approximately 1400 and 2010, several of which caused damage to settlements, agricultural areas and infrastructures on the valley floor. As a consequence, a series of mitigation measures have been implemented over the centuries to reduce debris-flow hazard and improve channel stability.

The first documented human interventions date back several centuries and mainly consisted of channel modifications and sediment removal works aimed at managing sediment deposition and protecting inhabited areas. More substantial hydraulic and torrent-control measures were introduced between the nineteenth and twentieth centuries, including channel deflection works to divert it in the fan farther from the village of Lasa, which had been repeatedly affected by debris-flow events, as well as slope stabilization interventions, reforestation programs, and the construction of numerous consolidation check dams along the main channel and its tributaries (**Comiti et al.**, **2014**). Currently, over 100 consolidation check dams are present within the catchment, exhibiting varying degrees of functionality. An example of this structures is shown in **Figure 3.7**.



Figure 3.7: Detailed view of some consolidation check dams (**Provincia Autonoma di Bolzano - Alto Adige**, **2026a**).

A major step in the mitigation strategy was the construction of a open-filter check dam (**Figure 3.8**) at the confluence of the Rio Gadria and Rio Strimm in 1975 at the fan apex. The structure incorporates a retention basin capable of storing several tens of thousands of cubic meters of sediment (**Comiti et al., 2014**). The slit dam is approximately 9 m high and presents a trapezoidal opening, 4 m wide at the top and 2 m wide at the bottom, equipped with a mechanical filter consisting of ten horizontal steel bars (**Simoni et al., 2017**), as shown in **Figure 3.8**. Since its construction, the structure has played a fundamental role in mitigating debris-flow hazard and has become a key component of the basin management system, preventing debris flows from reaching the alluvial fan and endangering downstream settlements. However, it also interrupts sediment continuity, reducing sediment supply to the Adige River and contributes to channel incision and morphological alteration downstream (**Simoni et al., 2017**). Frequent events lead to the progressive filling of the retention basin. Consequently, regular sediment removal is necessary to maintain the storage capacity of the basin, resulting in annual maintenance costs of approximately 200,000 €/year for the Autonomous Province of Bolzano (**Comiti et al., 2014**).



Figure 3.8: Views of the filter check dam: **(a)** photo taken from downstream; **(b)** photo taken from above after an event including the deposition basin. Sources: **(a) Bressan (2024)**, **(b) Provincia Autonoma di Bolzano - Alto Adige (2026a)**

.

Due to its strategic position and its importance for debris-flow management, the area surrounding the filter check dam was later selected as the main location for the installation of a comprehensive monitoring network.

3.5 The open-air laboratory of Rio Gadria basin

Monitoring activities play a fundamental role in the investigation and management of geomorphological hazards. Depending on their goals, monitoring systems may be designed either for scientific research, aimed to improve the understanding of process dynamics, or for operational purpose such as hazard assessment and risk mitigation through early warning applications (**Dei Cas et al., 2021**). The design of a monitoring network is influenced by several factors, including the type of processes under investigation, their magnitude and kinematic behavior, the characteristics of the involved material and the

specific goals of the monitoring programme.

In debris-flow research, monitoring is particularly important because these phenomena exhibit high spatial and temporal variability and are strongly controlled by local topographic, geological, and climatic conditions (**Comiti et al., 2014**). Long-term and continuous observations collected in instrumented catchments provide helpful information on event occurrence, volumes, discharge, flow velocity, flow depth, and other characteristics that are essential for hazard assessment, land-use planning, and the design of mitigation measures. In addition, long-term datasets allow to investigate the hydrological conditions that trig debris-flow events and to define rainfall thresholds for the development of warning systems.

Monitoring data also support the implementation of both structural and non-structural risk mitigation strategies (**Comiti et al., 2014**). While structural measures such as check dams, retention basins, and diversion channels are important components for debris-flow management, increasing attention has been dedicated to non-structural measures, including hazard zoning and warning systems, which depend mainly on the availability of reliable monitoring data. Although structural interventions are widely used to protect settlements and critical infrastructure, they are often associated with high construction and maintenance costs, operational constraints, and potential impacts on sediment continuity. Moreover, they cannot completely eliminate debris-flow hazard, leaving a residual level of risk. Non structural measures aim to reduce exposure and vulnerability through long-term planning strategies, such as land-use regulation, or through short-term actions based on early warning systems. In this context, continuous and accurate monitoring represents a key component of debris-flow risk management.

Despite their scientific and operational relevance, instrumented basins are relatively uncommon, and the amount of field data available is still limited compared to other geomorphological and fluvial processes (**Comiti et al., 2014**). For this reason, dedicated monitoring sites represent essential open-air laboratories for advanced understanding of debris-flow mechanical and rheological behavior, allowing to calibrate numerical models for simulating runout, improving the reliability of predictive models, and testing innovative warning technologies.

A permanent monitoring system was installed in the Gadria basin in 2011 (**Comiti et al., 2014**). The monitoring network, shown in **Figure 3.9**, designed and installed by the Civil Protection Agency (Provincial Operations Center and Mountain Basins Operations Unit) in collaboration with the Free University of Bolzano and the IRPI[1] Institute of the CNR[2], includes a range of complementary instruments such as rain gauges, stage sensors radar, geophones, video cameras, piezometers, soil-moisture probes. These devices continuously record meteorological, hydrological, and geomorphological variables, providing the collection of long-term datasets on both debris-flow triggering conditions and flow dynamics. The system integrates both stand-alone instruments and sensors connected to a centralized data acquisition network. In the lower part of the catchment, several

[1]Istituto di Ricerca per la Protezione Idrogeologica

[2]Consiglio Nazionale delle Ricerche

monitoring instruments are installed at specific sections along the channel, referred to as D1, D2 and D3, whose locations are shown in **Figure 3.9b**. Photos of the instrumented channel reach are shown in **Figure 3.10**. The monitoring instruments are described in the following subsections.

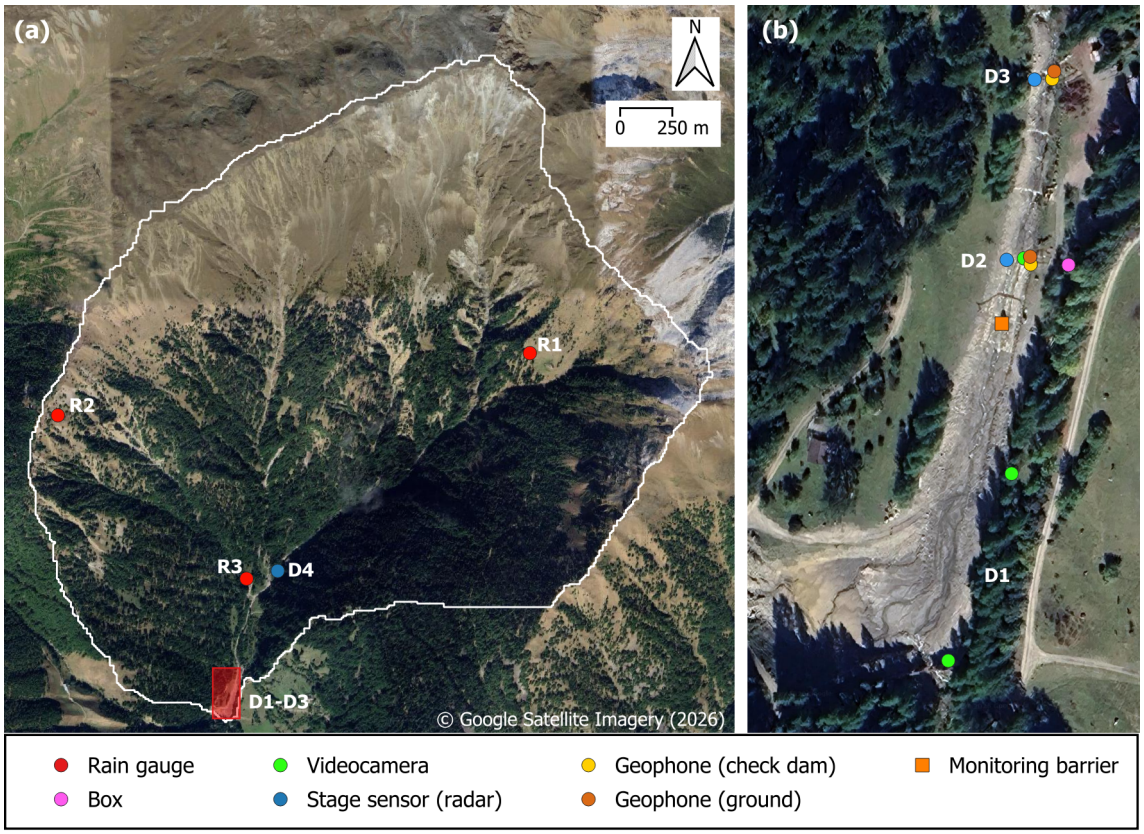


Figure 3.9: Spatial distribution of the monitoring instruments installed in the Gadria basin: **(a)** overview of the catchment and its installations; **(b)** detailed view of the red area in figure (a).

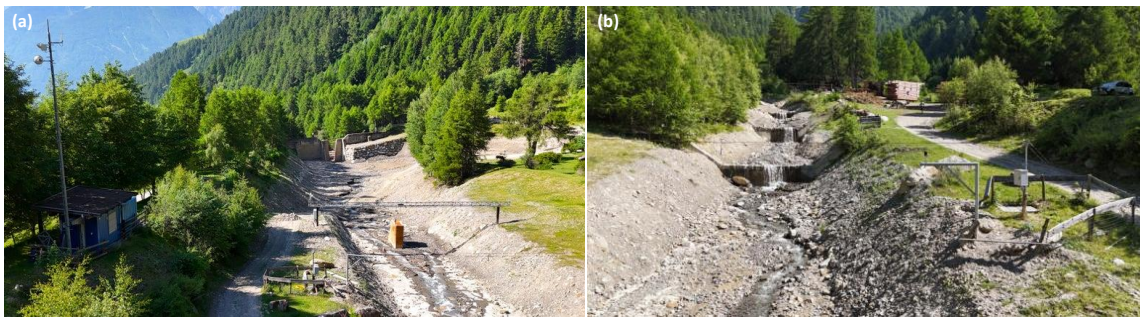


Figure 3.10: View of instrumented sections upstream the retention basin: **(a)** photo of sections D2 and D3 from downstream; **(b)** photo from upstream of section D2 and D1, comprehensive of monitoring barrier, retention basin and its filter check dam. Source: **Provincia Autonoma di Bolzano - Alto Adige (2026a)**

The monitoring network is supported by a central control station, identified as the box in **Figure 3.9**. This facility is accessible and hosts the data acquisition and management system responsible for collecting, storing and transmitting information from various sensors

installed throughout the area. Instruments installed along the main channel are connected to the central station either directly or through radio communication. Since GSM[3] coverage is unavailable within the basin, communication between remote instruments and the control station is based mainly on a dedicated radio network, allowing real time transmission of monitoring data and warning information and alert message directly to local authorities. To ensure data preservation instruments are equipped with local dataloggers for on-site storage also in case of transmission interruption. The monitoring infrastructure combines devices powered by the electrical line and autonomous energy supply systems charged by batteries or solar panel and was designed to allow the integration of additional sensors as monitoring requirements evolve (**Comiti et al., 2014**).

Debris flows recorded in the Gadria catchment display marked differences in terms of volume, surge sequence, flow duration, and propagation dynamics. The basin experiences approximately one or two debris-flow events per year, offering a unique opportunity to investigate the variability of debris-flow behavior under nearly identical boundary conditions. In most events the debris-flow front follows a intumescence. In some cases, however, the main front is preceded by a distinct precursory surge, characterized by moderate sediment concentration and pronounced turbulence[4]. **Table 3.1** summarizes the monitored events between 2011 and 2024 and their volume.

[3]Global System for Mobile Communications.

[4]Qualitative description based on personal communication with Dr. Lorenzo Marchi (CNR-IRPI).

Table 3.1: Debris-flow events recorded at the Rio Gadria monitoring site between 2011 and 2024.

Event	Estimated volume (m^3)	Reference
05/08/2011	2,400	**Comiti et al. (2014)**
18/07/2013	10,000	**Comiti et al. (2014)**
15/07/2014	11,600	**Coviello et al. (2019)**
8/05/2015	12,600	**Coviello et al. (2019)**
12/07/2016	2,400	**Coviello et al. (2021)**
26/07/2016	1,000	**Coviello et al. (2021)**
10/07/2017	5000	**Nagl et al. (2019)**
08/08/2017	4600	**Coviello et al. (2021)**
19/08/2017	5000	**Nagl et al. (2019)**
21/07/2018	-	-
11/06/2019	7,750	**Marchi et al. (2023)**
26/07/2019	6,700	**Marchi et al. (2023)**
02/08/2020	9,700	**Marchi et al. (2023)**
10/08/2020	15,350	**Marchi et al. (2023)**
12/08/2020	16,700	**Marchi et al. (2023)**
25/07/2022	-	-
07/08/2022	-	-
10/08/2022	-	-
12/07/2023	-	-
21/06/2024	-	-
19/07/2024	-	-
21/07/2024	-	-

3.5.1 Rain gauges

Precipitation in the Gadria basin is monitored through a network of three rain gauges (R1, R2 and R3 in **Figure 3.9a**) installed at different elevations (R1 at 2,160 m a.s.l., R2 at 2,320 m a.s.l., R3 at 1,500 m a.s.l.). The instruments record rainfall data at one-minute intervals and transmit the measurements to the central monitoring system via radio communication (**Comiti et al., 2014**). In addition to ground-based measurements, rainfall data can be derived from weather radar observations. However, the complex topography surrounding the basin limits the visibility of the weather radar antenna operated by the Autonomous Province of Bolzano at Monte Macaion. To overcome this limitation, radar-based precipitation estimates can be obtained from a radar installation located on the Valluga peak (2,809 m a.s.l.) in Austria.

The importance of high-resolution rainfall monitoring has been demonstrated in the Gadria catchment, where the network of rain gauges installed in the upper part of the basin allowed a detailed reconstruction of precipitation conditions associated with debris-flow events. These observations provided the basis for characterizing the spatial variability of rainfall and facilitated the identification of the rainfall conditions associated with debris-flow initiation. Based on a dataset of triggering rainfall events, **Marchi et al. (2019)** proposed a

local intensity–duration threshold expressed as:

$$I = 8 \cdot D^{-0.96} \tag{3.1}$$

where I is the mean rainfall intensity in mm/h and D is the rainfall duration in hours. Despite its utility, the threshold is not able to perfectly discriminate between triggering and non-triggering rainfall events. Several storms exceeded the critical threshold without generating debris flows, while at least one documented event (26 July 2016) occurred under unusually low rainfall intensity and cumulative precipitation. These observations suggest that rainfall characteristics alone cannot fully explain debris-flow occurrence and that additional factors, including sediment availability, moisture conditions, and short-term changes in sediment supply, may significantly influence the triggering process.

3.5.2 Stage sensors radar

Continuous measurements of flow depth are essential for the quantitative analysis of debris flows, as they allow to represent debris-flow hydrographs and to estimate key flow parameters such as velocity, discharge and volume. These measurements provide valuable information on the temporal evolution of debris-flow events and contribute to a better understanding of flow dynamics (**Dei Cas et al., 2021**).

Flow depth in the Gadria channel is monitored by radar stage sensors installed at the monitoring sections D2, D3, and D4 (**Figure 3.9**). The sensors are mounted above the channel and acquire measurements at one-second intervals, allowing continuous observations of debris-flow passage (**Comiti et al., 2014**). During the period 2011–2013, however, only the sensors located at the two downstream sections (D2 and D3) were operational. Instead, since 2019, the additional upstream monitoring section (D4) has been installed. Radar stage measurements are also used to estimate debris-flow velocity by comparing the timing of the flow signal recorded at D3 and D2. The two monitoring stations are separated by approximately 80 m along the channel thalweg, within a reach characterized by a sequence of consolidation check dams and an average bed slope of about 16%.

These sensors allow measurements of flow depth without direct contact with the mass, reducing the risk of damage during extreme events. Installed above the channel, as shown in **Figure 3.11**, these sensors determine the distance between the instrument and the flow surface, allowing continuous monitoring under hazardous conditions without direct exposure to the moving debris mass. When combined with channel geometry and velocity measurements, stage data can also be employed to estimate discharge and sediment transport rates, providing a basis for detailed quantitative analyses of debris-flow processes (**Dei Cas et al., 2021**).

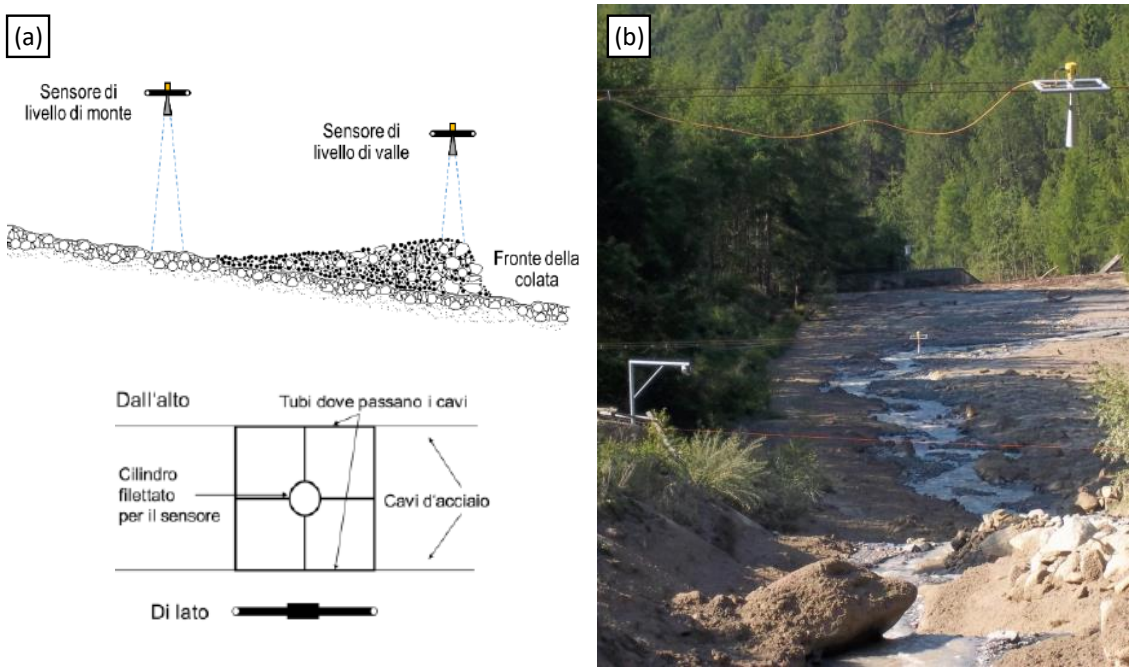


Figure 3.11: Stage sensor radar: **(a)** scheme of the position of the two radar sensors in the instrumented area and detail of the geometry sensor (**Dei Cas et al.**, **2021**); **(b)** Photo taken after an occurred event to highlight the position of stage radar sensor with respect the main channel (**Provincia Autonoma di Bolzano - Alto Adige**, **2026a**).

3.5.3 Geophones

Geophones are passive sensors able to detect ground vibrations generated by the passage of debris flows. They operate by converting ground motion into an electrical signal, which is subsequently digitalized and recorded by a data acquisition system. For debris-flow monitoring applications, single-axis geophones with natural frequencies of 4.5 or 10 Hz are commonly employed. The recorded signal is typically sampled at frequencies of at least 100 Hz in order to adequately capture the temporal characteristics of the vibrations generated by the flow. One of the main advantages of geophones is their relatively low cost and their possibility to be installed in safe places. Since they are inserted into the ground or positioned at a safe distance from the channel, they are less exposed to damage than sensors installed directly within the flow path. Furthermore, geophones are capable of detecting the approaching debris flow before it reaches the instrumented area, thereby providing additional time for warning systems (**Dei Cas et al.**, **2021**).

In the Gadria basin, vertical geophones have been installed at monitoring sections D2 and D3 (**Figure 3.9b**) since 2012 (**Comiti et al.**, **2014**). At each section, one sensor is embedded in loose soil, while the other is attached to the concrete structure of a consolidation check dam. This configuration was adopted to investigate different responses to vibrations induced by debris flow on different materials. The sensors (**Figure 3.12**) are characterized by a natural frequency of 10 Hz, selected on the basis of previous studies investigating the frequency content of ground vibrations generated by debris flows. Dominant frequencies

generally fall within the range of 10-80 Hz, with lower frequencies typically associated with the surge peak and higher frequencies with the flow tail. Consequently, 10 Hz geophones are considered suitable for capturing the full spectrum of vibrations expected during debris-flow events. The recorded signal is analyzed in terms of mean wave amplitude and is recorded at 1-second intervals by a datalogger. Together with radar stage measurements, geophone data can be used to estimate debris-flow velocity and provide information on event magnitude after appropriate calibration procedures.



Figure 3.12: Detail of one of the vertical 10-Hz geophones (**Coviello et al., 2019**).

3.5.4 Video cameras

Video cameras represent a helpful tool for debris-flow monitoring, as they provide direct observations of flow dynamics. Their main advantage is the possibility of visually documenting the evolution of the events, allowing a better interpretation of the underlying physical processes. Thanks to high resolution and elevated frame rate, they are able to capture the rapid changes that occur during debris-flow propagation and to identify important flow features. Video recordings can be used to investigate variations in sediment concentration and grain-size composition, both between different events and within the same debris flow. They also allow flow transitions detection, such as the beginning of turbulence, which frequently characterizes the final stages of an event. In addition, cameras can document the presence of precursory surges, secondary pulses, temporary flow interruptions, and the transport of timber by the flow (**Dei Cas et al., 2021**).

Night-time monitoring requires additional equipment: typically artificial lighting systems such as spotlight are installed and they activate automatically by rainfall sensors or other triggering devices as shown in **Figure 3.13**. Adequate illumination is essential to ensure continuous observation during intense storms, when debris flows are most likely to occur (**Dei Cas et al., 2021**).



Figure 3.13: Video camera and spotlight installed at site (**Dei Cas et al.**, **2021**).

Video recordings can also provide quantitative information. In particular, surface flow velocities can be estimated through Large-Scale Particle Image Velocimetry (LSPIV), a technique that tracks the displacement of visible features between consecutive frames and measures two dimensional velocities (**Theule et al.**, **2018**; **Dei Cas et al.**, **2021**).

In the Gadria basin, three video cameras are installed at monitoring sections D1 and D2 (**Figure 3.9b**). Two cameras are located at D1, providing complementary views of the debris retention basin, allowing the observation of flow deposition and sediment accumulation processes, since the lower one frames the deposition basin from downstream while the upper one maps the retention zone from the left including the confluence area with the Strimm torrent. The third camera is installed at D2 and is oriented upstream towards the channel looking at the monitored section D3 where radar stage sensors and geophones are present. This configuration enables the visual documentation of debris-flow propagation and supports the interpretation of the measurements collected by the other monitoring instruments. All cameras are equipped with spotlights that are automatically activated by rain gauges during rainfall events (**Comiti et al.**, **2014**).

3.5.5 Hydrological monitoring tools

In addition to the instruments previously described, specific tools were installed within the area to investigate hydrological conditions of the site and their potential influence on debris-flow initiation. These installations were designed to monitor pore-water pressure, groundwater variation, and soil moisture, providing information on moisture conditions and hydrological processes. Two monitoring areas were identified within the Gadria catchment. The first zone, located in the upper part of the basin, consists of steep channel heads characterized by absence of vegetation and abundant loose sediment including coarse soil and large boulders. Several pore-pressure transducers were installed below the ground surface to monitor water-pressure variations. The second site is located on a vegetated hillslope near the divide with the Strimm basin and was instrumented with piezometers equipped with pressure transducers and soil-moisture sensors installed at different depths. These instruments were intended to investigate the spatial and temporal variability of groundwater levels and soil moisture conditions within the catchment (**Comiti et al.**, **2014**).

3.5.6 Monitoring barrier

A monitoring barrier was installed in 2016 along the centerline of the channel (**Figure 3.14a**), near the fan apex, 200 m upstream of the retention basin, in a portion where the mean slope of the channel is about 6 °. The system, as it is possible to see in **Figure 3.14b**, consists of a reinforced concrete pylon, approximately 3 m high and 1 m wide, anchored to a foundation embedded in the channel subsoil. A disconnected transverse check dam level with the ground is located in front of the barrier, resulting in the second concrete component of the monitoring structure. To measure the forces exerted by debris flows, two force plates with dimensions of 1 × 1 m were installed on the channel bed as shown in **Figure 3.14c**. One plate is positioned immediately upstream of the barrier, while the second is located 2 m above. Each plate is supported by four load pins with a nominal capacity of 100 kN and operates at a sampling frequency of 2.4 kHz. In addition, both force plates are equipped with pressure transducer that record basal pore-fluid pressure within the flowing material. Flow depth is monitored using two ultrasonic sensors operating at 100 Hz. As it is possible to see in **Figure 3.14c**, one sensor is installed above the force plate beside the barrier, while the other is positioned directly in front of the barrier. The combined measurements of flow depth and normal force provide the basis for estimating a time and depth-averaged bulk density of the debris-flow mixture. The barrier is instrumented with an array of 14 load cells installed on its upstream vertical face as shown in **Figure 3.14d**. These sensors, with nominal capacities ranging between 1 and 2 MN, are vertically placed at intervals of 0.20 m, with the lowest sensor located 0.25 m above the channel bed. This configuration allows for a more detailed assessment of impact forces during the event. To prevent damage and contamination caused by fine sediments and mud, the sensor array is protected by a thick steel plate directly connected to both the load cells and the concrete structure, thereby minimizing potential damping effects. The load cells acquire data at a frequency of 4.8 kHz. Flow velocity upstream the barrier was estimated through particle-tracking analysis of video recordings collected during debris-flow events. The cameras installed perpendicular to the channel provided images that were afterwards used to determine surface flow velocities (**Nagl et al., 2022**).

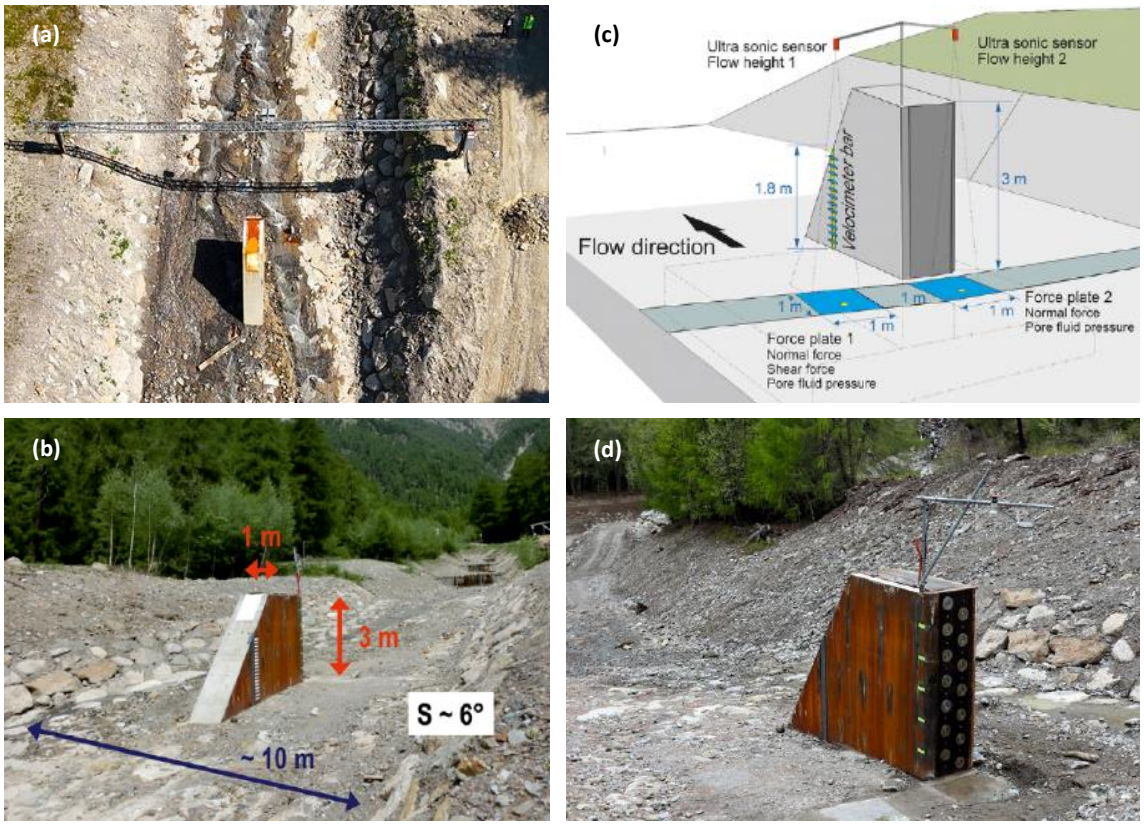


Figure 3.14: Monitoring barrier in the centerline of the channel: **(a)** photo of the barrier taken from above (**Provincia Autonoma di Bolzano - Alto Adige**, **2026a**); **(b)** photo of the barrier taken downstream it (**Nagl et al.**, **2020**); **(c)** Illustration of the monitoring barrier and sensors position (**Nagl et al.**, **2020**); **(d)** photo of monitoring barrier from August 2017 taken upstream it (**Nagl et al.**, **2022**).

3.6 Description of the analyzed events

3.6.1 July 18, 2013 event

The debris flow that occurred on 18 July 2013 was triggered by a short-duration convective storm that affected only the northeastern area of the basin, producing a highly localized rainfall distribution. At the upstream rain gauge (R1 in **Figure 3.9a**), a cumulative rainfall of 23 mm was recorded over 33 minutes, as shown in **Figure 3.15**. Considering the time elapsed before the debris-flow front reached the monitoring station, the effective triggering rainfall was 17.2 mm in only 15 minutes, corresponding to an average rainfall intensity of 69 mm/h and a maximum 10-minute intensity of 14.7 mm. In contrast, the rain gauge R3 (see **Figure 3.9a**) recorded little more than 5 mm over the same time period (**Figure 3.15**), highlighting the strong spatial variability of precipitation typical of localized convective storms. Radar series confirmed that the rainfall was concentrated over the debris-flow initiation area, emphasizing the importance of extensive rainfall monitoring for the reliable detection of triggering conditions (**Comiti et al.**, **2014**).

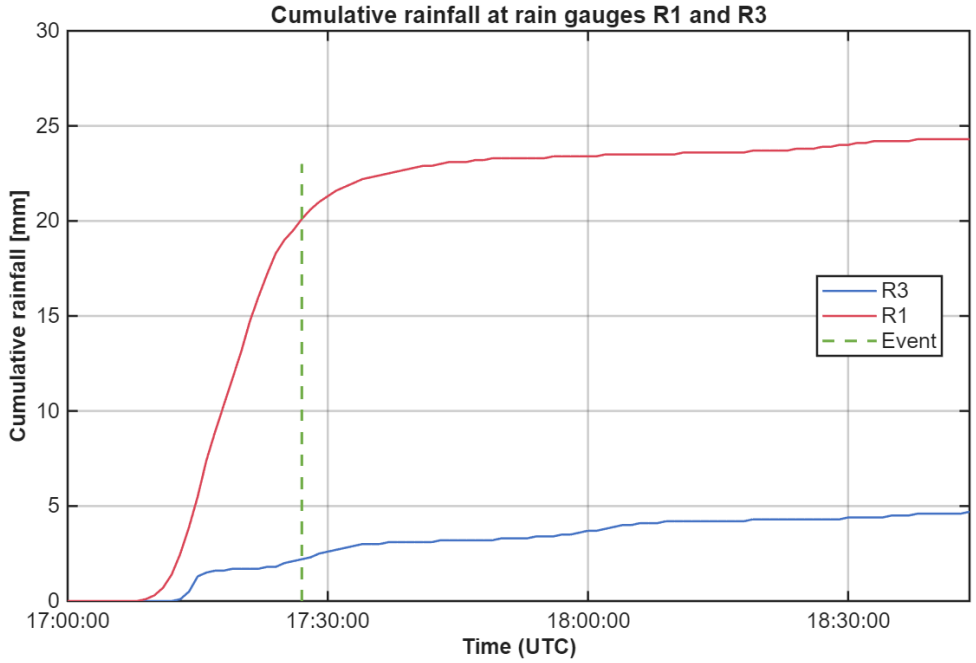


Figure 3.15: Cumulative precipitation curve of July 18, 2013

As shown in **Figure 3.16**, which contains the flow-height time series recorded at monitoring sections D2 and D3, the event exhibited the characteristic behavior of an alpine debris flow, with hydrographs characterized by a sharp ascending branch, rapid recession and short duration (**Comiti et al., 2014**). Based on the flow-stage records acquired by the radar stage sensors, the event lasted approximately 20 minutes.

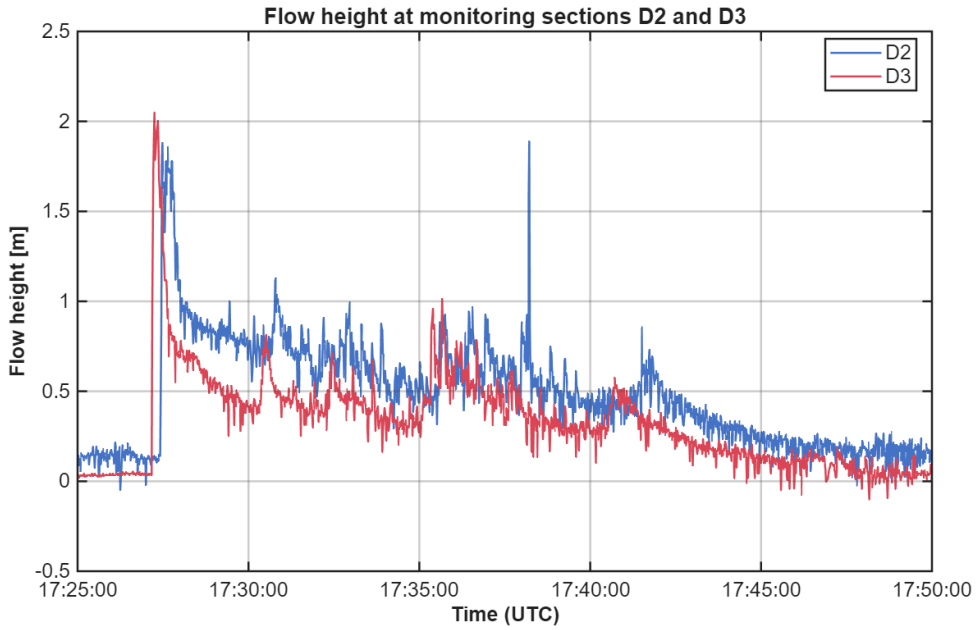


Figure 3.16: Hydrograph at station D2 and D3 of the July 18, 2013 debirs-flow event.

Flow observations through video cameras frames (see **Figure 3.17**) and radar measurements revealed a coarse, bouldery front approximately 2 m deep, followed by a sequence of smaller and more fluid surges that transported isolated large boulders. Before the arrival

of the debris-flow front, the flow remained low and limpid. Along the monitored path, the event was predominantly erosive, with significant channel-bed entrainment contributing to the increase in sediment volume during propagation (**Comiti et al.**, **2014**).



Figure 3.17: Frames of the July 2013 debris flow from the video cameras at section D1 and D2: **(a)** snapshot of the front arrival at D1 downstream video camera; **(b)** frame of the front arrival at D1 upstream video camera which is looking through the deposition basin; **(c)** picture of the deposition basin after the event from D1 upstream video camera; **(d)** snapshot showing the initial front at D2; **(e)** frame of the central part of the event at D2; **(f)** picture of an advanced surge carrying a big boulder at D2. Source: personal communication with University of Bolzano

The velocity of the event was estimated using two distinct approaches (**Comiti et al.**, **2014**). The former is based on the travel time of debris-flow peaks between the monitored cross sections D2 and D3, located approximately 80 m apart. Flow velocity is obtained by

dividing the distance between the D3 and D2 by the time interval taken by the same surge to travel that distance. Peaks were manually identified by the stage hydrographs recorded by the radar sensors (**Figure 3.16**). To avoid errors in the velocity estimation, isolated peaks, that can be attributed to the passage of large boulders under the sensors, were excluded from the analysis. The latter is based on a cross-correlation analysis of the flow-depth time series recorded at the two monitoring sections D3 and D2. This technique estimates the propagation time lag between the hydrographs by maximizing their correlation, providing an objective estimate of the mean surge velocity. The peak-travel-time method yielded an average flow velocity of approximately 5.7 m/s, whereas the cross-correlation analysis provided a slightly lower estimate of 5.0 m/s. (**Comiti et al., 2014**).

Later on, **Theule et al.** (**2018**) estimated surface flow velocity of the front of the July 2013 debris flow through visual measurement on orthorectifed images and LSPIV[5] technique. The analysis was performed using frames acquired by the upstream video camera installed at section D1, looking at the deposition basin which provided the most suitable positioning for this approach. The estimated average surface velocity of the debris-flow front was 4.4 m/s for both approaches.

The total volume of the 2013 debris-flow event was estimated at approximately 10,000 m^3, obtained by summing the volumes of the individual surges estimated from the recorded hydrograph at section D2 by integrating the product of the flow cross-sectional area and the surge velocity over the surge duration. An independent topographic assessment based on terrestrial laser scanner (TLS) surveys of the retention basin indicated a deposited sediment volume of approximately 8,000 m^3. The slightly lower value is consistent with field observations showing that part of the debris flow passed through the open filter check dam and with the different sediment concentration between the moving debris flow and the final deposited material (**Comiti et al., 2014**).

3.6.2 July 26, 2019 event

Unlike the 2013 event, the rainfall responsible for the 26 July 2019 debris flow was more uniformly distributed across the catchment. As shown in **Figure 3.18**, the upstream rain gauge R1 recorded a cumulative rainfall of approximately 10.4 mm, while rain gauge R3 measured nearly 9.8 mm over the duration of the event. Rainfall at R1 increased rapidly before reaching a nearly constant value, after which only negligible additional precipitation was recorded. The debris-flow initiation occurred when the cumulative rainfall had already reached its final value at R1, whereas R3 continued to register light rainfall after the event. Compared with the 2013 debris flow, the similar cumulative rainfall measured at both rain gauges suggests that precipitation was not confined to the debris-flow source area.

[5]Large-scale particle image velocimetry.

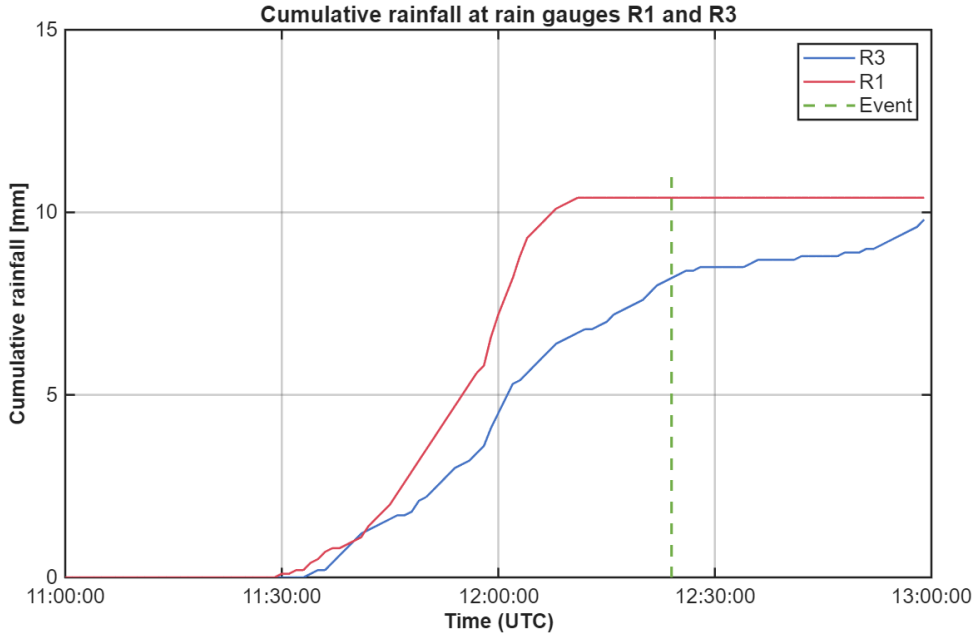


Figure 3.18: Cumulative precipitation curve of July 26, 2019

As observed for the 2013 event, the 2019 debris flow was characterized by a bouldery front, with the diameter of the largest boulders being comparable to the flow depth. The passage of the front was followed by sixteen closed-spaced surges, which displayed a muddier composition without large boulders (**Nagl et al., 2022**). Unlike the 2013 event, however, the front followed a initial precursory surge characterized by moderate sediment concentration and pronounced turbulence. **Figure 3.19** presents radar stage hydrograph records for the three monitoring stations (D2, D3 and D4) over the entire duration of the event, while **Figure 3.20** shows selected frames acquired by the video cameras.

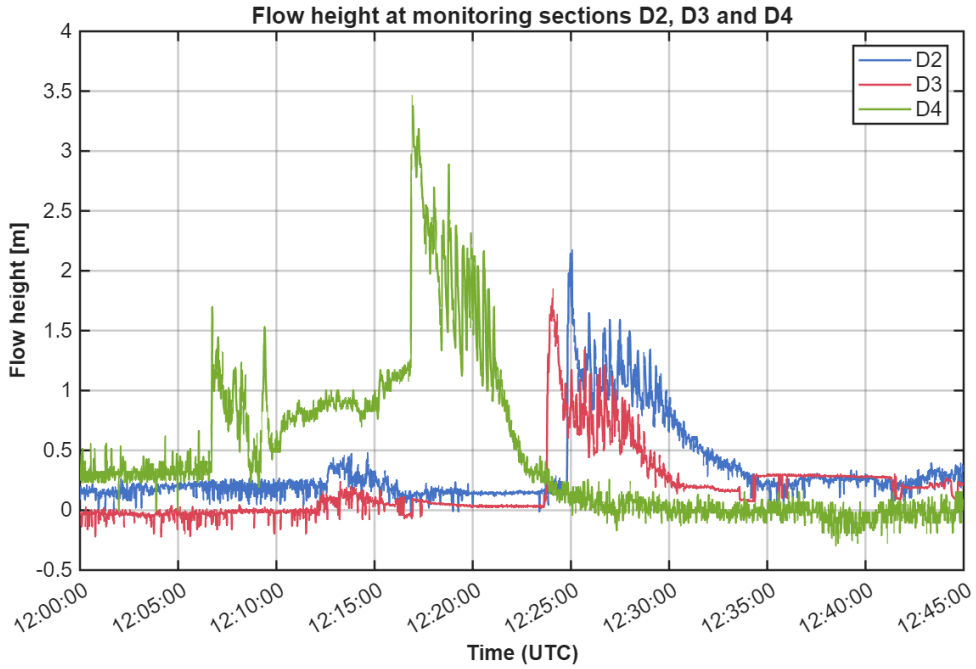


Figure 3.19: Hydrograph at station D2 and D3 of the July 26, 2019 debirs-flow event.



Figure 3.20: Frames of the July 2019 debris flow from the video cameras at section D1 and D2: **(a)** snapshot of the front arrival at D1 downstream video camera; **(b)** frame of the front arrival at D1 upstream video camera which is looking through the deposition basin; **(c)** picture of the deposition basin after the event from D1 upstream video camera; **(d)** snapshot showing the precursory flow before the front arrival; **(e)** frame of the initial front at D2; **(f)** picture of the central part of the event at D2. Source: personal communication with University of Bolzano

Previous analyses of the Gadria monitoring data reported that debris-flow fronts generally travel faster along the D3–D2 reach than along the upstream D4–D3 reach, despite their similar average channel slope. This behavior has been attributed to the wider cross sections and locally reduced channel gradient in the central portion of the D4–D3 reach, close to the confluence with two tributaries (**Marchi et al., 2023**). However, such behavior was not observed during the 2019 event, for which comparable mean flow velocities were

estimated in the two reaches, equal to approximately 1.3 m/s between D4 and D3 and 1.4 m/s between D3 and D2. As for the 2013 event, the mean flow velocity was estimated by dividing the distance between the monitoring sections (D4–D3 and D3–D2) by the travel time of the debris-flow front between the corresponding stations.

The total volume of the 2019 debris-flow event was estimated at approximately 6,700 m^3, obtained by integrating the product of the mean flow velocity of the main surges in the D3–D2 reach and the corresponding flow cross-sectional area over the duration of the event. The cross-sectional area was derived from the flow-stage measurements recorded at station D3, assuming a deposit-free channel cross section (**Marchi et al.**, **2023**).

4 Numerical modeling of debris-flow events

This chapter presents the numerical modeling framework adopted to back-analyze the monitored debris-flow events in the Rio Gadria catchment. The simulations were performed using the RASH3D numerical code, which is introduced in the first section together with its main modeling assumptions. Subsequently, the preparation of the numerical model for the benchmark event of 18 July 2013 is described, including the identification of the source area, the generation of the topographic input data and the computational mesh. Finally, the modeling approach adopted for the 26 July 2019 event is presented. Since this event is used to assess the transferability of the calibrated rheological parameters under different debris-flow conditions, only the aspects that differ from the benchmark configuration are discussed.

4.1 RASH3D numerical code

RASH3D is a numerical code developed for the simulation of the runout of rapid flow-like landslides over complex three-dimensional topographies. The code is based on a continuum mechanics approach and on the Saint-Venant hypothesis for shallow flows, allowing the propagation of the moving mass to be simulated over irregular three-dimensional terrain (**Pirulli**, **2005**, **2010**). The formulation implemented in RASH3D relies on a number of simplifying assumptions. Within this framework, the real heterogeneous moving mass is represented as an equivalent continuum, thus avoiding the explicit description of the interactions among its individual solid and fluid components. This simplification makes it possible to describe the behavior of complex flow-like phenomena through a single-phase formulation (**Figure 4.1**).

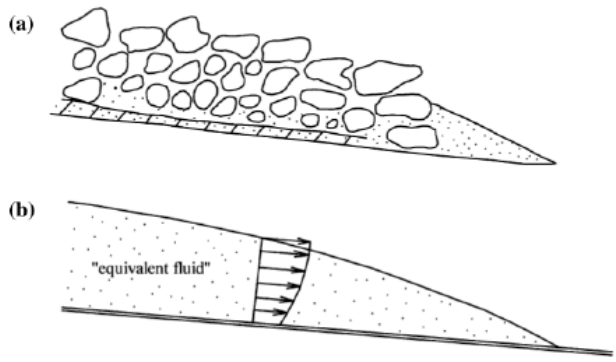


Figure 4.1: From a complex moving mass to an equivalent continuum (**Pirulli and Mangeney**, **2008**): **(a)** heterogeneous flowing mass; **(b)** equivalent fluid.

The equivalent material is assumed to be incompressible, with density considered constant in time and space (**Pirulli**, **2005**). The motion of the continuum flux can be described through the three-dimensional balance equations of mass and momentum. Under the assumption of constant density, conservation of mass can be expressed as

$$\nabla \cdot \mathbf{v} = 0 \tag{4.1}$$

while conservation of momentum can be written in vector form as

$$\rho \left[\frac{\partial \mathbf{v}}{\partial t} + (\mathbf{v} \cdot \nabla)\mathbf{v} \right] = \nabla \cdot \boldsymbol{\sigma} + \rho \mathbf{g} \tag{4.2}$$

where $\mathbf{v} = (v_x, v_y, v_z)$ is the three-dimensional velocity vector,

$$\boldsymbol{\sigma} = \begin{bmatrix} \sigma_{xx} & \sigma_{xy} & \sigma_{xz} \\ \sigma_{yx} & \sigma_{yy} & \sigma_{yz} \\ \sigma_{zx} & \sigma_{zy} & \sigma_{zz} \end{bmatrix}$$

is the Cauchy stress tensor, ρ is the density of the equivalent continuum, and $\mathbf{g} = (g_x, g_y, g_z)$ is the gravitational acceleration vector. The momentum balance therefore represents a system of three equations, one for each spatial direction, which together with the mass-conservation equation describe the three-dimensional motion of the equivalent continuum, resulting in a system of four scalar equations (eqs. (4.3) to (4.6)) that cannot be analytically solved without introducing additional simplifying assumptions.

$$\frac{\partial v_x}{\partial x} + \frac{\partial v_y}{\partial y} + \frac{\partial v_z}{\partial z} = 0 \tag{4.3}$$

$$\rho \left[\frac{\partial v_x}{\partial t} + \frac{\partial (v_x^2)}{\partial x} + \frac{\partial (v_x v_y)}{\partial y} + \frac{\partial (v_x v_z)}{\partial z} \right] = - \left[\frac{\partial \sigma_{xx}}{\partial x} + \frac{\partial \sigma_{yx}}{\partial y} + \frac{\partial \sigma_{zx}}{\partial z} \right] + \rho g_x \tag{4.4}$$

$$\rho \left[\frac{\partial v_y}{\partial t} + \frac{\partial (v_y v_x)}{\partial x} + \frac{\partial (v_y^2)}{\partial y} + \frac{\partial (v_y v_z)}{\partial z} \right] = - \left[\frac{\partial \sigma_{xy}}{\partial x} + \frac{\partial \sigma_{yy}}{\partial y} + \frac{\partial \sigma_{zy}}{\partial z} \right] + \rho g_y \tag{4.5}$$

$$\rho\left[\frac{\partial v_z}{\partial t}+\frac{\partial(v_z v_x)}{\partial x}+\frac{\partial(v_z v_y)}{\partial y}+\frac{\partial(v_z^2)}{\partial z}\right]=-\left[\frac{\partial \sigma_{xz}}{\partial x}+\frac{\partial \sigma_{yz}}{\partial y}+\frac{\partial \sigma_{zz}}{\partial z}\right]+\rho g_z \tag{4.6}$$

However, solving the complete three-dimensional problem would require the spatial and temporal evolution of the velocity and stresses throughout the entire moving mass. RASH3D adopts a depth-averaged formulation based on the shallow-flow approximation. In this approach, the characteristic flow depth, H, is assumed to be much smaller than the characteristic longitudinal dimension, L, as illustrated in **Figure 4.2**. The motion is consequently assumed to develop predominantly along the basal topography.

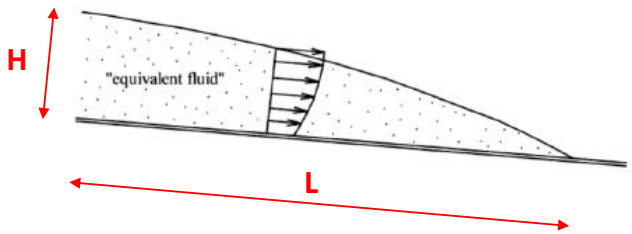


Figure 4.2: Scheme of the equivalent fluid with its characteristic dimensions. Source: modified from **Pirulli and Mangeney** (**2008**).

A further simplifying assumption consists in neglecting the velocity component normal to the basal surface, so that

$$\mathbf{v}\cdot\mathbf{n}=0 \tag{4.7}$$

where $\mathbf{n}$ is the unit vector normal to the local topographic surface. These simplifying assumptions allow the governing equations to be integrated over the flow depth and the three-dimensional distributions of the variables to be replaced by their corresponding depth-averaged quantities (**Pirulli**, **2005**).

As a consequence of depth averaging, information on the variation of velocity and stresses throughout the flow depth is no longer explicitly represented. The original three-dimensional system is reduced to one mass-conservation equation and two momentum equations along the directions tangent to the topographic surface presented in eqs. (4.8) to (4.10). These three equations are called depth-averaged equations or shallow-water equations.

$$\frac{\partial h}{\partial t}+\frac{\partial \overline{v_x}h}{\partial x}+\frac{\partial \overline{v_y}h}{\partial y}=0 \tag{4.8}$$

$$\rho\left[\frac{\partial(\overline{v_x}h)}{\partial t}+\frac{\partial(\overline{v_x^2}h)}{\partial x}+\frac{\partial(\overline{v_x v_y}h)}{\partial y}\right]=-\frac{\partial(\overline{\sigma_{xx}}h)}{\partial x}+T_x+\rho g_x h \tag{4.9}$$

$$\rho\left[\frac{\partial(\overline{v_y}h)}{\partial t}+\frac{\partial(\overline{v_y v_x}h)}{\partial x}+\frac{\partial(\overline{v_y^2}h)}{\partial y}\right]=-\frac{\partial(\overline{\sigma_{yy}}h)}{\partial x}+T_y+\rho g_y h \tag{4.10}$$

Here, h is the flow depth, $\overline{v_x}$ and $\overline{v_y}$ are the depth-averaged velocity respectively in x and y direction, $\overline{\sigma_x}$ and $\overline{\sigma_y}$ are the corresponding depth-averaged normal stresses and the terms T_x and T_y are the shear components accounting both for friction at the base of the flowing mass and for internal energy dissipation during propagation.

RASH3D therefore describes the propagation of the equivalent continuum over three-dimensional terrain rather than the complete three-dimensional internal dynamics of the moving mass. In this sense, the three-dimensional character of RASH3D refers to the complex topographic surface over which the flow propagates, while the governing equations themselves are depth-averaged (**Pirulli**, **2005**, **2010**).

The resulting system of conservation equations is solved within an Eulerian framework over an unstructured triangular computational mesh through a kinetic numerical scheme based on a finite-volume approach (**Pirulli**, **2005**; **Pirulli et al.**, **2017**). The use of an unstructured mesh allows complex topographies to be represented and the spatial resolution to be locally adapted according to the required level of detail.

The balance equations must be complemented by constitutive equations, also referred to as rheological laws, which describe the mechanical behavior of the equivalent fluid under different flow conditions and differ according to the energy dissipation mechanism considered. In depth-averaged models, the rheological behavior is introduced through the basal resistance terms T_x and T_y appearing in the momentum equations (eqs. (4.9) and (4.10)). These terms provide the closure required for the system of governing equations. In general, the basal resistance component, T_i, can be expressed as

$$T_i = -\tau sgn(\overline{v_i}) \qquad i = x, y \tag{4.11}$$

where τ denotes the magnitude of the basal shear stress, while $sgn(\overline{v_i})$ accounts for the direction of the resistance relative to the depth-averaged velocity component $\overline{v_i}$.

The choice of the rheological law therefore determines how the mechanisms responsible for energy dissipation during propagation are represented within the numerical model. Depending on the characteristics of the moving material, energy dissipation may be associated with different mechanisms, including basal friction, viscous effects and turbulent or collisional interactions. Different rheological formulations account for these mechanisms, either individually or through their combination. For consistency, the different rheological formulations are here recast in terms of the basal shear stress magnitude τ, while the corresponding resistance components are obtained according to eq. (4.11).

The simplest formulation is the frictional, or Coulomb, law (**Pirulli et al.**, **2015**), in which the resistance is entirely governed by basal friction. The basal resistance is proportional to the normal stress through a friction coefficient $\mu = \tan\varphi$ where φ is the apparent basal friction angle. It can be expressed as

$$\tau = \sigma_n \cdot \tan\varphi \tag{4.12}$$

where σ_n is the normal stress. For a simple inclined surface characterized by a slope angle

θ, the relation between the friction angle and the slope determines if the mass can come to rest. If $tan(\varphi) < tan(\theta)$, the downslope component of gravity exceeds the frictional resistance and the moving mass cannot rest on the inclined surface. On the other hand, if $tan(\varphi) > tan(\theta)$ the frictional resistance can balance the driving force, allowing the material to stop (**Mangeney et al., 2000**). Since the frictional rheology does not include a viscous contribution, its application is mainly associated with highly granular flows, such as debris avalanches, where the solid phase largely predominates over the liquid phase.

As the liquid phase becomes increasingly significant, viscous effects may play an important role in the flow behavior and should therefore be taken into account. The simplest constitutive model accounting for viscosity is the Newtonian rheology (**Bird et al., 2007**), in which the shear stress is directly proportional to the shear rate. Under laminar flow conditions, this relationship can be expressed as

$$\tau = \eta \frac{dv}{dz} \tag{4.13}$$

where η is the dynamic viscosity, assumed to be constant for a Newtonian fluid and dv/dz represents the shear rate (the velocity gradient in the direction normal to the bed). Consequently, the relationship between shear stress and shear rate is linear, with a slope equal to the dynamic viscosity. However, the applicability of the Newtonian model to landslide propagation is generally limited, since flow-like landslides, such as debris flows, typically exhibit non-Newtonian behavior and may be better represented by rheological models accounting for plastic or dilatant behavior.

An extension of the Newtonian model is provided by the Bingham rheology, which is suitable for materials characterized by a yield stress τ_y (**La Porta et al., 2024**). Unlike a Newtonian fluid, a Bingham material starts to deform only when the applied shear stress exceeds this threshold. Its rheological behavior can be expressed as

$$\begin{cases} \dfrac{dv}{dz} = 0, & \tau \leq \tau_y, \\ \tau = \tau_y + \eta \dfrac{dv}{dz}, & \tau > \tau_y, \end{cases} \tag{4.14}$$

where τ_y is the yield stress, η is the dynamic viscosity and dv/dz represents the shear rate (the velocity gradient in the direction normal to the bed). Below the yield stress, no shear deformation occurs, whereas above this threshold the material exhibits a viscous behavior, with the shear stress increasing linearly with the shear rate.

A further rheological formulation accounts for energy dissipation associated with turbulent effects and particle interactions (**Julien and Lan, 1991**). In this case, the shear stress increases quadratically with the shear rate and can be expressed as

$$\tau = \zeta \left(\frac{dv}{dz} \right)^2 \tag{4.15}$$

where ζ is a coefficient associated with turbolent and collisional energy dissipation, while

dv/dz represents the shear rate. This formulation therefore represents a nonlinear behavior in which the resistance increases more rapidly as the shear rate increases.

More complex rheological models can be obtained by combining different resistance mechanisms. Among these, the Voellmy rheology combines a frictional contribution with a turbulent contribution (**Pirulli et al.**, **2015**). Originally developed for snow avalanches, this formulation has subsequently been widely adopted for the simulation of flow-like landslides. According to the notation adopted, the magnitude of the basal shear stress is expressed as

$$\tau = \sigma_n \tan \varphi + \zeta \left(\frac{dv}{dz} \right)^2 \tag{4.16}$$

where σ_n is normal stress, φ is the apparent basal friction angle, ζ is the coefficient associated with the quadratic velocity-dependent term, and dv/dz represents the shear rate.

In RASH3D, different constitutive laws can therefore be adopted according to the mechanical behavior assumed for the equivalent fluid (**Pirulli**, **2005**).

4.2 Model setup for the 18 July 2013 event

4.2.1 Identification of the source area

The present study does not include an analysis of debris-flow triggering. For this reason, the source area adopted in the numerical model was defined using information available from previous studies. In particular, the Management Priority Index (MPI) map developed by **D'Agostino and Bertoldi** (**2014**) was considered. This map was obtained through an index-based approach, as described in Chapter 2, combining field surveys and high-resolution LiDAR data to identify and rank sediment source areas according to their capability to deliver debris-flow material to a selected outlet. The MPI combines three complementary indicators accounting for the susceptibility of the catchment to generate debris flows, the triggering potential, and the sediment volume that can potentially be delivered to the selected outlet. The resulting MPI map (**Figure 4.3a**) provides a spatial distribution of the areas characterized by the highest potential sediment contribution according to their management priority.

Since the objective of the present work is the numerical modeling of the 18 July 2013 debris-flow event, the MPI map alone was not considered sufficient to define the release area adopted in the numerical model. Therefore, it was combined with the initiation area proposed by **Finis et al.** (**2017**) for the same event, shown in **Figure 4.3b**.

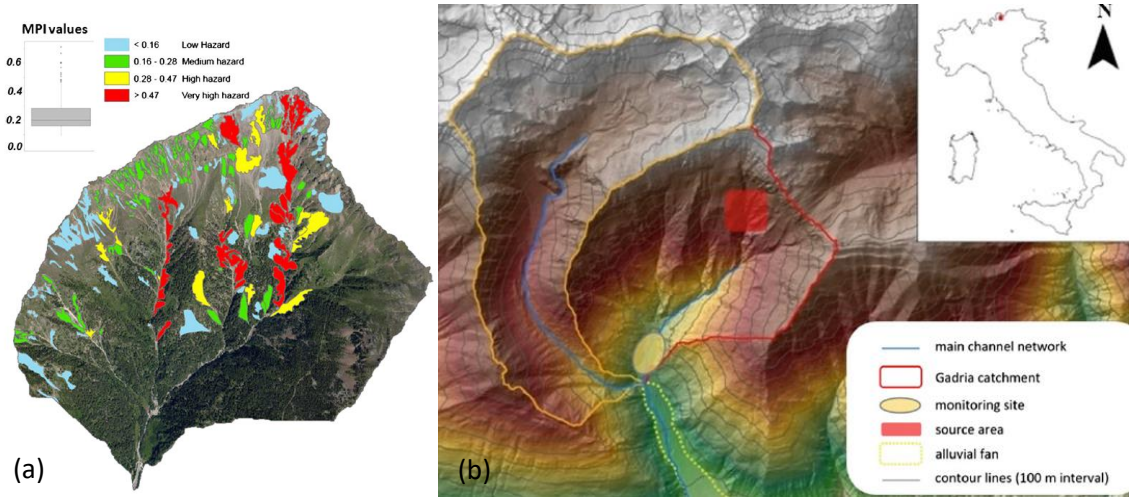


Figure 4.3: Source datasets used for the identification of the triggering area adopted in the numerical model: **(a)** MPI map proposed by **D'Agostino and Bertoldi** (**2014**); **(b)** Gadria basin system with indication of the initiation area of the 18 July 2013 debris-flow event (modified from **Finis et al.** (**2017**)).

Both maps were georeferenced in QGIS and converted into vector layers. A layer including only the sectors classified as Very High Hazard (MPI > 0.47) was extracted from the MPI map proposed by **D'Agostino and Bertoldi** (**2014**), while a second layer was created from the polygonal initiation area identified by **Finis et al.** (**2017**). The source area adopted in the present study was then obtained by selecting the portions of the high-priority MPI areas located within the initiation polygon. This procedure allowed the definition of an initiation area consistent both with the geomorphological assessment of the sediment source areas and with the documented initiation zone of the benchmark event. The source area obtained through the procedure described above is shown in **Figure 4.4** and was subsequently adopted for the numerical simulations.

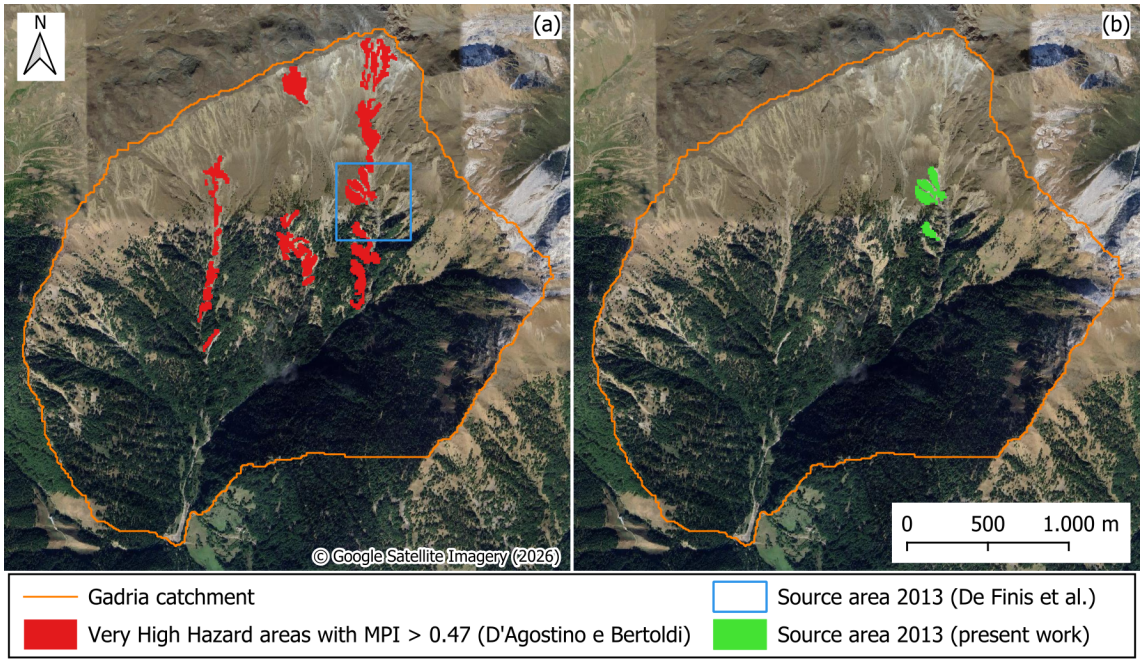


Figure 4.4: Source area adopted for the numerical simulation of the 18 July 2013 debris-flow event: **(a)** Very High Hazard sediment source areas (MPI > 0.47) identified by **D'Agostino and Bertoldi** (**2014**) together with the polygonal initiation area proposed by **Finis et al.** (**2017**); **(b)** final release area obtained after intersecting the two datasets and adopted in the present study.

4.2.2 Topographic input data

The numerical model was built using a 1 m resolution Digital Terrain Model (DTM) derived from an airborne LiDAR[1] survey carried out over the Rio Gadria catchment in July 2011 (**Paganini et al., 2011**)[2]. The survey was conducted by the OGS[3] institute on behalf of the CNR–IRPI and covered an area of approximately 7 km^2. The acquisition was designed to achieve a nominal point density greater than 8 points per m^2, with a horizontal accuracy of ±25 cm and a vertical accuracy of ±10 cm. It should be noted that the available DTM does not represent the topography immediately preceding the benchmark event considered in this study. With respect to the LiDAR acquisition, only one debris-flow event occurred before 18 July 2013 (5 August 2011), potentially modifying the morphology of portions of the catchment. Since no more recent topographic survey was available, the 2011 DTM was adopted as the best available representation of the pre-event topography.

The original `.xyz` file was first inspected in QGIS. As shown in **Figure 4.5a**, the LiDAR survey covered an area considerably larger than the Gadria catchment and the domain adopted for the numerical simulations. Moreover, several portions of the DTM

[1] Light Detection and Ranging.

[2] The LiDAR dataset was kindly made available by Prof. Andrea Andreoli (Libera Università di Bolzano).

[3] Istituto Nazionale di Oceanografia e di Geofisica Sperimentale.

were not covered by the survey and so affected by missing elevation data as shown in detail in **Figure 4.5b**. Because some of these gaps were located within the area potentially affected by the simulated debris flow, they were reconstructed before the preparation of the numerical model using a triangulation with linear interpolation algorithm (Surfer), which performs a Delaunay triangulation of the available points, estimating grid node values based on the slope of each resulting triangle and interpolates the missing elevations from the surrounding triangular faces. To avoid introducing unnecessary modifications to the original terrain, the interpolation was restricted to the selected modeling domain.

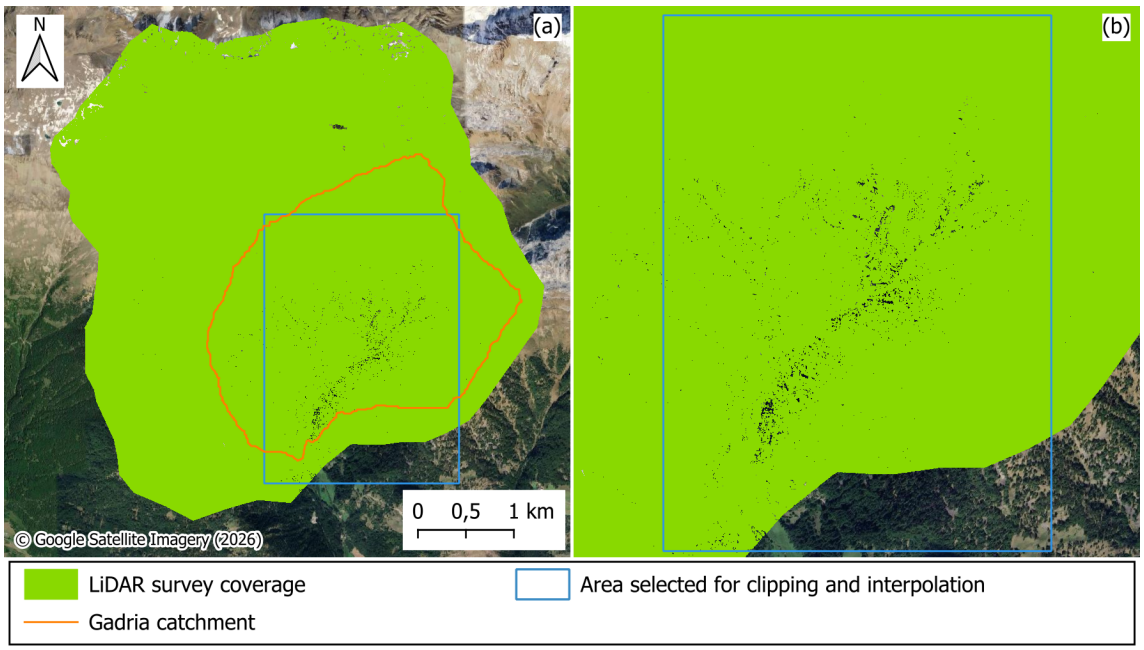


Figure 4.5: Preparation of the topographic input data: **a** Extent of the LiDAR survey, Gadria catchment and modeling domain; **(b)** Detail of the selected area showing missing elevation data.

The obtained DTM was subsequently imported back into QGIS and converted into a point shapefile to facilitate the assignment of the model input parameters. The flow thickness (h) associated with the source area layer described in the previous subsection was transferred to the corresponding DTM points layer, while all points outside the source area were assigned a value of $h = 0$ m. Assuming a uniform distribution of the released material over the selected source area, the initial released thickness was computed as

$$h = \frac{V}{A} \tag{4.17}$$

where $V = 10{,}000$ m^3 is the total debris-flow volume reported by **Comiti et al. (2014)** for the 18 July event and adopted in the simulations, $A \approx 24{,}380$ m^2 is the extent of the selected source area. This resulted in a uniform thickness of approximately 0.41 m.

4.2.3 Mesh generation

Generation of the computational mesh

RASH3D solves the governing equations on an unstructured triangular computational mesh. Therefore, before running the numerical simulations, the topographic dataset described in the previous subsection must be discretized into a finite-element mesh suitable for the numerical solver. The mesh was generated using a MATLAB preprocessing workflow coupled with the open-source software Gmsh. In this first configuration, the open filter check dam was not represented in the computational mesh.

Gmsh is an open-source finite-element mesh generator. Local mesh sizing can be prescribed to modify the mesh resolution with respect to the input DTM by refining or coarsening the mesh in areas of particular interest, such as the initiation area, the instrumented channel reach, the deposition basin and the slit of the open filter check dam.

A MATLAB preprocessing script was used to prepare all the input files required by Gmsh and RASH3D. Starting from the processed DTM, the script generated the computational domain, imported the refinement or coarsening areas, created the Gmsh geometry file and, once the mesh had been generated, interpolated the terrain elevations into the mesh nodes. Finally, the mesh was exported both in the native RASH3D format and in a text format suitable for visualization in QGIS.

As with all numerical models, the computational time increases with the number of mesh elements. Different characteristic mesh sizes were therefore assigned to specific regions of the computational domain in order to balance numerical accuracy and computational cost, thus keeping the simulation time within acceptable limits. Furthermore, the implementation of RASH3D supports computational meshes that contain up to approximately one million nodes. Consequently, preserving the original DTM resolution over the entire computational domain is not feasible, making the adoption of a variable mesh size necessary.

The adopted settings are summarized in **Table 4.1**. Three regions with different sizes of mesh elements were identified within the computational domain (**Figure 4.6**), while a 20 m target element was assigned to the outer boundary. Then, the resulting computational mesh is shown in **Figure 4.7**.

Table 4.1: Target mesh sizes adopted in the computational domain.

Region	**Mesh size (m)**	**Purpose**
Outer boundary	20	Reduce the computational cost outside the area of interest
Initiation area and upper channel	2	Adequate terrain representation while limiting the number of mesh elements
Instrumented channel reach	1	Preserve the original DTM resolution in the monitoring area where numerical and observed data are compared
Deposition basin	2	Adequate representation of the deposition area while reducing the computational effort

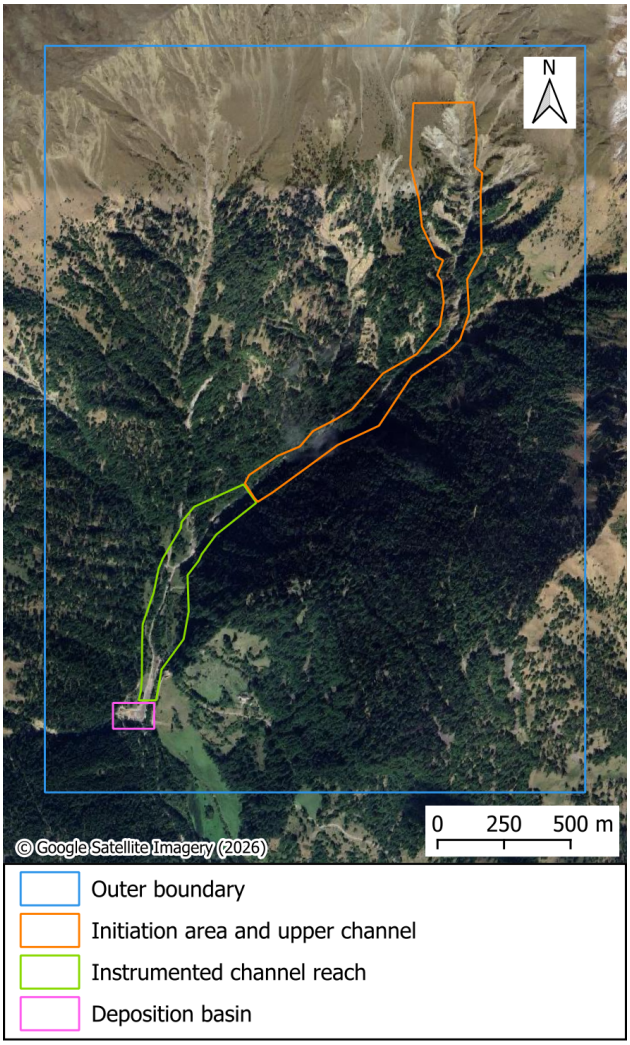


Figure 4.6: Mesh sizing regions adopted for the generation of the mesh. The figure shows the outer boundary of the computational domain together with the three areas assigned different target mesh sizes.

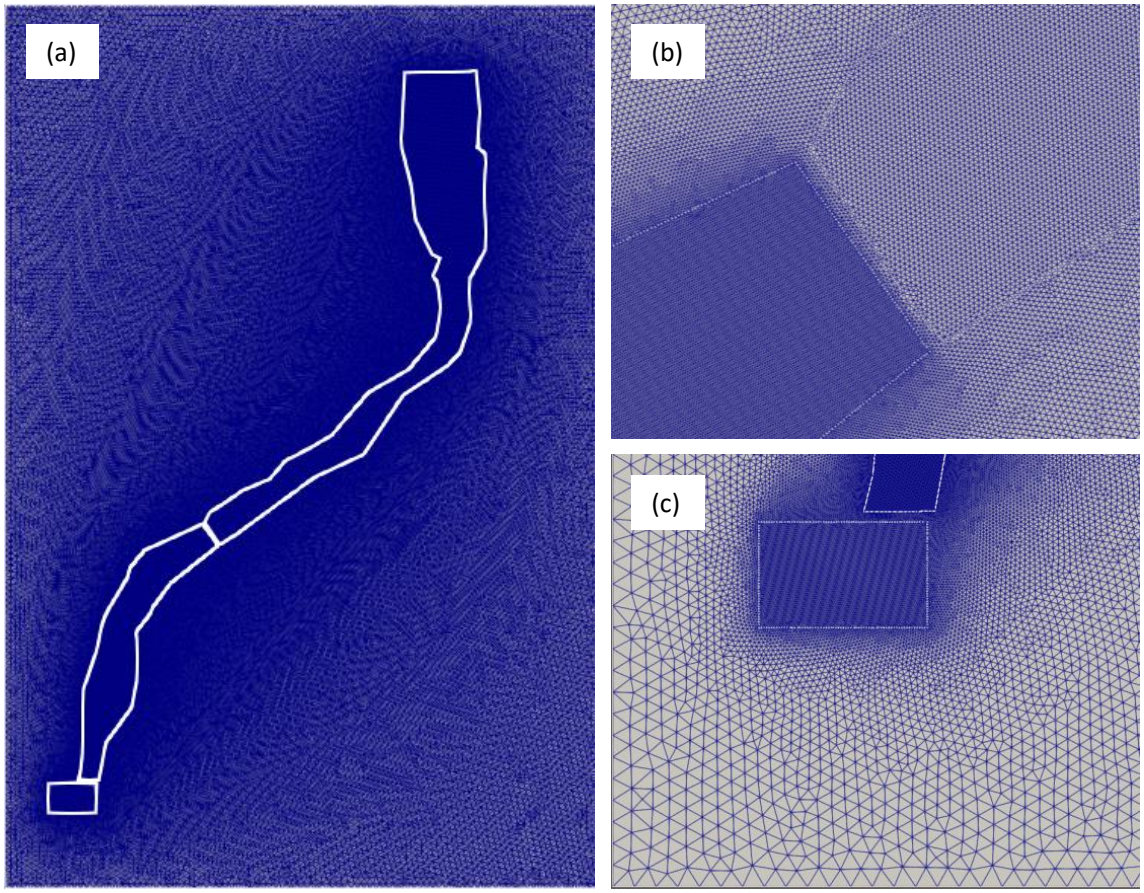


Figure 4.7: Computational mesh adopted for the numerical simulation of the 18 July 2013 event: **(a)** Overview of the unstructured triangular mesh over the computational domain; **(b)** detail of the transition between different mesh size regions; **(c)** detail of the transition between the outer boundary and the deposition basin mesh size region.

Representation of the open filter check dam

The mesh configuration described in the previous subsection was initially generated without explicitly representing the open filter check dam, preserving the natural terrain topography derived from the DTM at its location. This first configuration was adopted to analyze the propagation of the debris flow and to compare the numerical results with the monitoring data collected along the instrumented channel reach. Following the back-analysis of the 18 July 2013 event against the available monitoring data, two additional mesh configurations were generated to investigate the influence of the open filter check dam on the simulated flow dynamics. For both mesh configurations, the mesh size settings were kept unchanged with respect to the reference mesh configuration except for the deposition basin, where the target element size was reduced from 2 m to 1 m to recover the original DTM resolution, providing a finer discretization around the check dam and improving the representation of the flow-structure interaction.

The check dam was not introduced by modifying the Digital Terrain Model, but it was added directly on the computational mesh after its generation by modifying the elevations

(z) of the mesh nodes located within the planimetric footprint of the barrier and its opening (**Figure 4.8**).

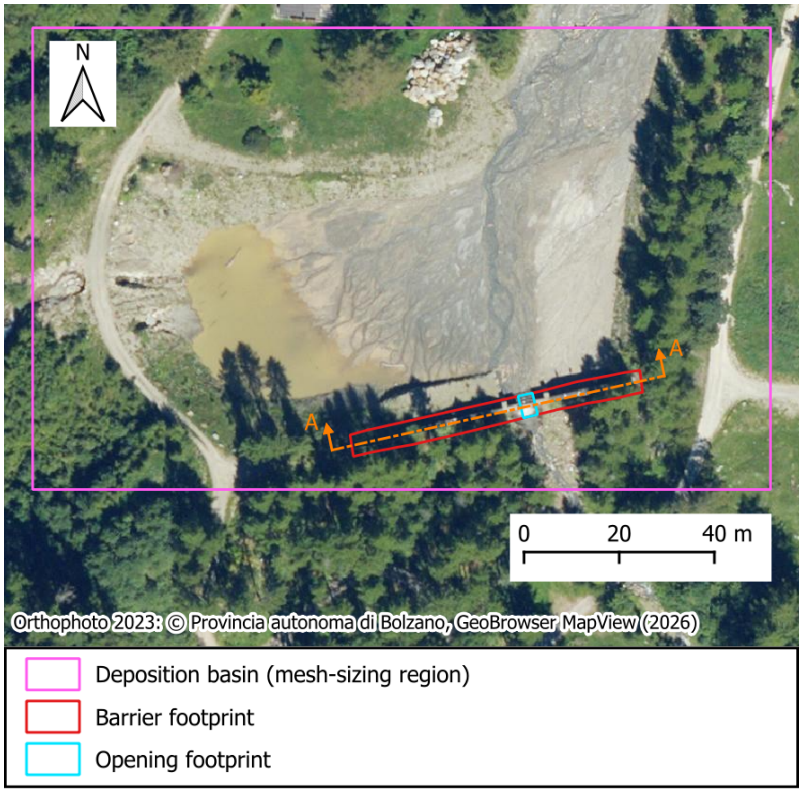


Figure 4.8: Barrier and opening footprints adopted for the representation of the open filter check dam in the computational mesh with indication of the deposition basin contour used for the sizing of the mesh.

As described in Chapter 3, the slit dam is approximately 9 m high and presents a trapezoidal opening, 4 m wide at the top and 2 m wide at the bottom, equipped with a mechanical filter consisting of ten horizontal steel bars (**Simoni et al., 2017**). The latter were not represented in the numerical model, as their detailed geometry was not considered compatible with the level of spatial discretization adopted in the present study. To simplify the geometry while preserving the overall characteristics of the structure, the opening was approximated by a rectangular section 3 m wide. This value represents an intermediate solution between the two limiting configurations. A 4 m wide opening would correspond to the most critical condition, allowing the largest amount of debris-flow material to pass through the barrier, while a 2 m opening would maximize the retaining effect. Furthermore, the height of the rectangular opening, set equal to 8 m, was selected to preserve a 1 m high basal sill in the numerical model to account for the presence of a base at the bottom of the opening. In this way the area of the opening ($A = 24$ m^2) is equal to the area of the trapezoidal opening, neglecting the presence of the horizontal steel bars.

The first mesh configuration represents the check dam as a closed obstacle, without considering the vertical opening. The barrier height was assumed equal to 9 m. To generate the closed configuration, the lowest terrain elevation along the longitudinal alignment of the barrier ($z = 1390.4$ m) was selected as the reference level and increased by 9 m, as

shown in **Figure 4.9**. Subsequently, all mesh nodes located within the barrier footprint were assigned the resulting elevation only if their original level was lower than the top of the barrier, thereby producing a continuous obstacle with a constant z coordinate (z = 1399.4 m).

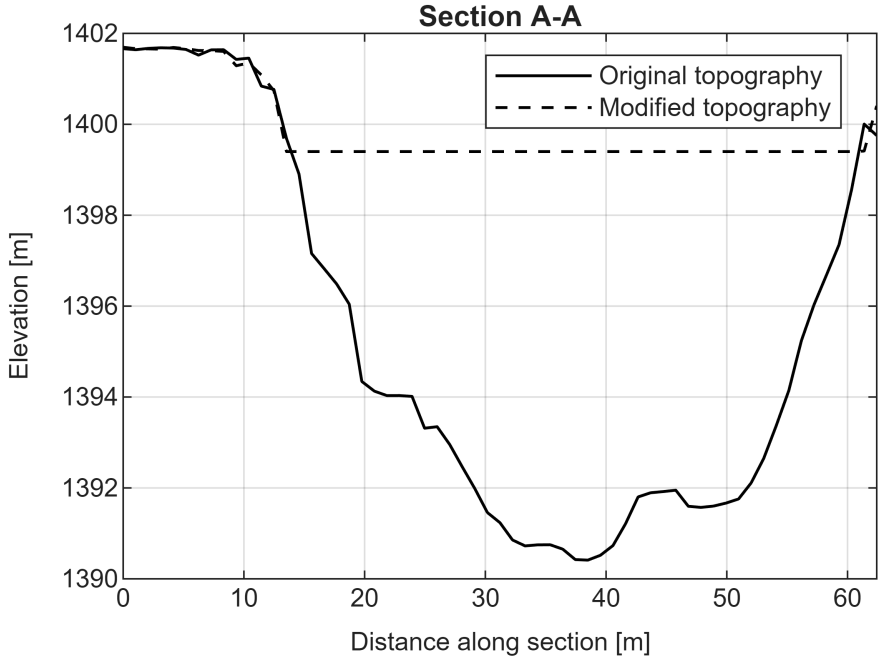


Figure 4.9: Longitudinal section of the barrier embedded in the original topography.

In the second configuration, the opening was explicitly represented. A new computational mesh was generated by introducing an additional local mesh-sizing region corresponding to the opening footprint shown in **Figure 4.8**. This footprint was first used to prescribe a target mesh element size of 0.5 m, allowing an adequate geometric representation of the 3 m wide opening. Once the mesh had been generated, the same footprint was used to identify the mesh nodes whose elevations were lowered by 8 m to reach a constant final level (z = 1391.4 m). This procedure created the simplified rectangular opening, preserving the basal sill of 1 m.

Figure 4.10 shows a three-dimensional view of the two configurations used to model the filter check dam.

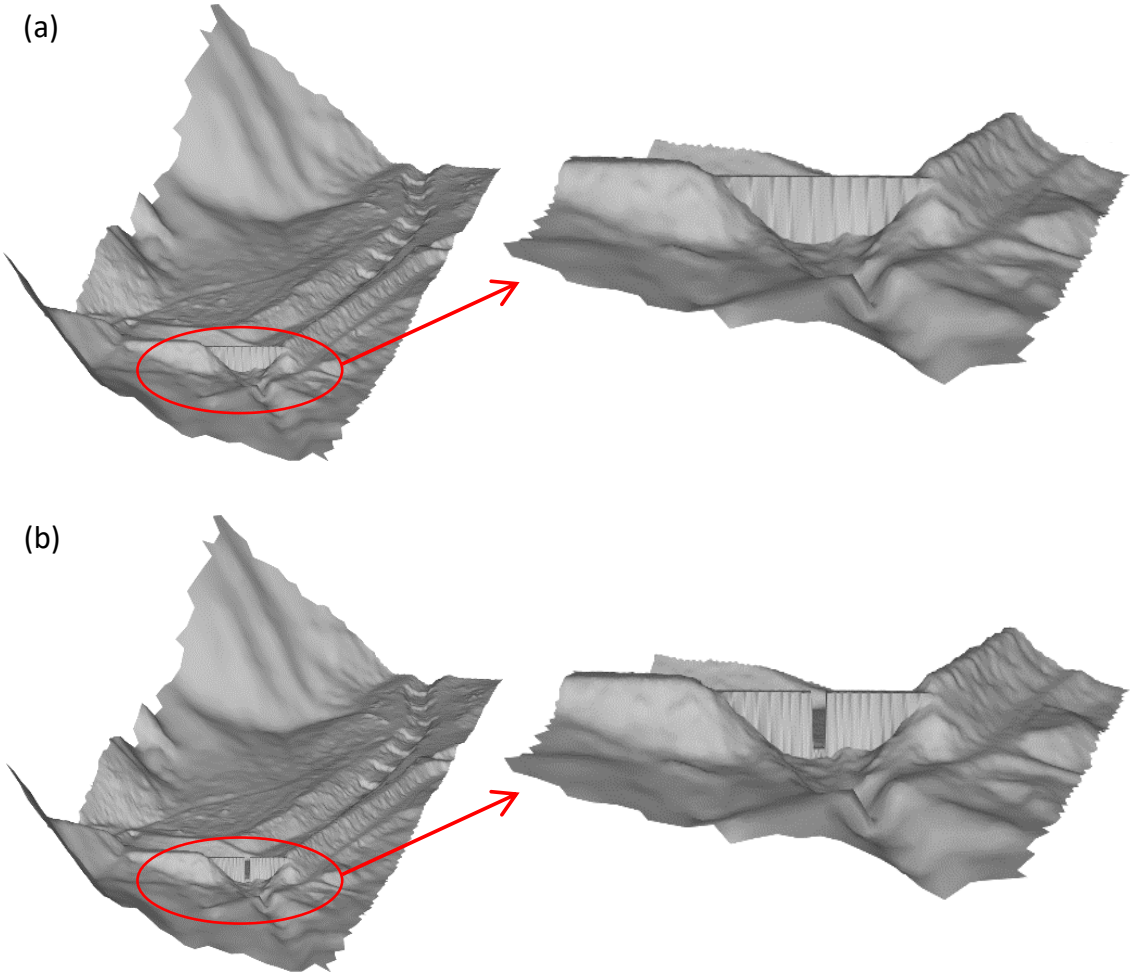


Figure 4.10: Three-dimensional view of the modeled check dam embedded in the topography: **(a)** closed barrier configuration; **(b)** open barrier configuration.

4.2.4 Rheological law

Among the rheological formulations available in RASH3D, the Voellmy law was adopted in the present study to simulate the propagation of the 18 July 2013 debris-flow event in the Gadria basin. As introduced in Section 4.1, this formulation combines frictional and turbulent resistance mechanisms (see eq. (4.16)). For its application in RASH3D, the two resistance mechanisms are expressed in terms of the friction coefficient μ and the turbulence coefficient ξ. The magnitude of the basal shear stress is expressed as

$$\tau = \rho g h \mu + \frac{\rho g v^2}{\xi} \tag{4.18}$$

where ρ is the density of the flowing mass, g is the gravitational acceleration, h is the flow depth, and v is the magnitude of the depth-averaged velocity. The friction coefficient is defined as $\mu = \tan\varphi$, where φ denotes the apparent basal friction angle, while ξ is

the turbulence coefficient, expressed in m/s^2. Consequently, increasing μ enhances the frictional resistance, while increasing ξ reduces the velocity-dependent contribution.

The Voellmy rheology was selected for its ability to account simultaneously for frictional and velocity-dependent resistance mechanisms. The latter allows the resistance to vary with the dynamic conditions of the flow, increasing as the flow velocity increases. This combined configuration is particularly suitable for describing the high mobility that characterizes rapid flow-like landslides as debris flows. The two parameters therefore use different controls on flow propagation and deposition and were treated as calibration parameters in the present study for the 2013 event (see Section 5.1).

4.3 Model setup for the 26 July 2019 event

The numerical model for the 26 July 2019 event was prepared following the same workflow adopted for the 18 July 2013 benchmark event. Therefore, only the aspects that differ from the previous setup are described in this section, while all the other modeling assumptions, preprocessing procedures and numerical settings were kept unchanged.

4.3.1 Identification of source area

Contrary to the benchmark event, no detailed study of the debris-flow source area is available in the literature for the 26 July 2019 event. Nevertheless, **Marchi et al.** (**2023**) report that the upper monitoring station, installed in 2018, is located approximately 500 m downstream of the initiation area of debris flows (**Figure 4.11a**). Although the geometry of this initiation area is not specified, its location suggests that the event originated within the tributary channel zone associated with the 2013 release area.

Based on these observations, the source area adopted in the present study for the 2019 event was defined at the confluence between the identified tributary channel and the Rio Gadria main channel. As shown in **Figure 4.11b**, the highlighted tributary corresponds to the channel along which the upper monitoring station is installed. The release area was positioned at the channel confluence rather than within the upper initiation zone to introduce the released material directly into the main channel.

The polygon that identifies the source area was delineated using the channel as longitudinal reference and its lateral boundaries were defined according to the local morphology, following the surrounding contour lines to preserve the natural confinement of the valley. This criterion allowed the initial debris-flow mass to remain confined within the channel while avoiding the inclusion of the adjacent hillslopes. The resulting source area adopted for the numerical simulation is shown in **Figure 4.11b**.

The adopted source area should therefore be regarded as a numerical initialization area rather than a reconstruction of the actual debris-flow initiation zone. This modeling choice provides a representation of the debris-flow mass entering the Rio Gadria main channel, which is consistent with physical reality, while avoiding assumptions regarding the exact location and extent of the initiation area that cannot be supported.

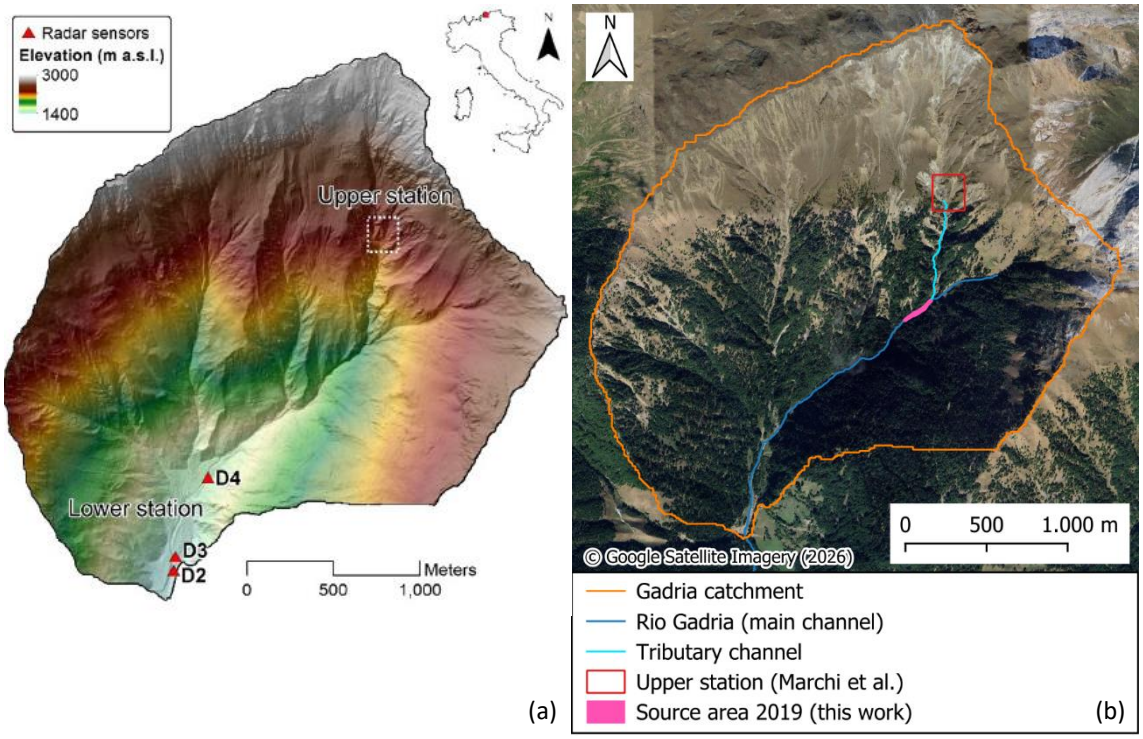


Figure 4.11: Identification of the source area adopted for the numerical simulation of the 26 July 2019 debris-flow event: **(a)** map of the Gadria catchment with details regarding instruments location at the lower station and contour of the zone that identifies the upper station (**Marchi et al.**, **2023**); **(b)** overview of the Gadria catchment with identification of the the upper station zone contour, the main channel and its tributary and the source area for the 2019 event.

4.3.2 Topographic input data

The preparation of the topographic input data follows exactly the same workflow adopted for the 18 July 2013 event (Subsection 4.2.2). Therefore, the same LiDAR-derived DTM, the interpolation of the missing elevation data and the preprocessing procedure were retained without modification.

The same LiDAR DTM adopted for the benchmark event was also used for the 26 July 2019 simulations, as no more recent pre-event topographic dataset was available within the material provided for this study. Compared with the 2013 event, the time interval between the LiDAR survey and the 2019 debris flow is considerably longer, during which several events occurred in the Gadria catchment. Consequently, local geomorphological changes associated with repeated erosion and deposition processes are not represented in the adopted topography. This limitation should be considered when interpreting the numerical results, as the actual terrain morphology at the time of the event may have differed locally from the one represented by the adopted DTM. Although this limitation may affect the local accuracy of the simulations, the employed DTM provides a consistent topographic basis for comparing the numerical response of the two debris flows.

The assignment of the initial flow thickness followed the same procedure described for the benchmark event. A value of $h = 0$ m was assigned to all DTM points outside the

selected source area, whereas a uniform thickness within the source area was computed according to eq. (4.17). In this case the volume of the debris flow was set equal to 6,700 m^3 according to **Marchi et al.** (**2023**), while the extension of the selected source area was chosen in order to have a released thickness ranging between 1 m and 1.5 m. The area was approximately equal to 5380 m^2 resulting in a flow thickness of 1.25 m. Finally, the resulting DTM togheter with the released flow thickness were exported in the same format adopted for the 18 July 2013 simulations.

4.3.3 Mesh generation

The computational mesh was generated following the same workflow adopted for the benchmark event (Subsection 4.2.3). Although a new unstructured mesh was generated to account for the different input data, including the release area and the associated initial flow thickness, the computational domain, the target mesh sizes and the extent of the local refinement or coarsening regions were kept unchanged. Contrary to the 2013 configurations, only the mesh representing the natural topography was considered, and no simulations including the geometry of the check dam were performed.

4.3.4 Rheological law

The Voellmy rheology adopted for the 18 July 2013 benchmark event was also employed for the 26 July 2019 debris flow. The calibration of the rheological parameters for the benchmark event and their subsequent application to the 2019 event are discussed in Chapter 5.

5 Results and discussion

This chapter presents and discusses the results of the numerical simulations performed for the 18 July 2013 and 26 July 2019 debris-flow events. The analysis is organized into three main parts. First, the 2013 benchmark event was investigated within the instrumented channel reach between the D3 and D2 monitoring sections, with the aim of calibrating the Voellmy rheological parameters through comparison with the available recorded monitoring data. The selected parameter combination is then used to investigate flow propagation and deposition within the retention basin, considering the different configurations of the open filter check dam described in the previous chapter. Finally, the same rheological parameters are applied to the 2019 event to assess their transferability between different debris-flow events occurring within the same catchment.

5.1 18 July 2013 event: flow dynamics and rheological calibration

To compare the numerical results with the monitoring data recorded at D3 and D2, a circular sampling area with a radius of 1 m was defined around the the known coordinates of each stage radar sensor[1]. For each RASH3D output, all the mesh nodes that fell within the sampling area were selected and both the maximum and mean values of flow depth (h) and flow velocity (v) were extracted. The resulting values were then used to construct numerical time series at D3 and D2 sections. Model outputs were saved at 10 s intervals over a total simulated time of 2000 s.

The maximum and mean values provided comparable temporal trends and led to the same overall interpretation of the numerical response. To avoid redundant graphical information, only the maximum values are therefore presented. Maximum values were selected to preserve the local peak response within the sampling area centered on the monitoring sensors without the spatial smoothing introduced by averaging. The corresponding results obtained from the mean values are reported in Appendix A, providing an additional verification of the results and confirming the robustness of the observed trends.

[1]The sensors coordinates were kindly provided by Dr. Marco Martini and Dr. Pierpaolo Macconi (both from Centro Funzionale provinciale dell'Agenzia per la Protezione Civile della Provincia Autonoma di Bolzano).

As a preliminary step, the possibility of transferring rheological parameters previously adopted in the literature for the numerical modeling of the same event was investigated. The Voellmy rheological parameters $\mu = 0.12$ and $\xi = 600$ m/s^2, adopted by **Finis et al. (2017)**, were therefore initially assigned to the numerical model developed in this study. The purpose of this simulation was not to validate the calibration proposed in the previous study by other authors, but rather to investigate if a set of parameters already applied to the same event could be directly transferred to the numerical setup developed in the present work.

The numerical response obtained with this combination of parameters was examined at both monitoring sections and is shown in **Figure 5.1**. While the simulation at D3 did not exhibit a marked accumulation of material, a substantially different behavior emerged at D2, where the simulated material progressively accumulated in the proximity of the monitoring section. This behavior was characterized by a persistent increase in flow depth and by a sudden reduction in velocity, in contrast to the behavior observed during the real event. A second simulation was therefore performed by decreasing the turbulence coefficient from $\xi = 600$ to 500 m/s^2, while maintaining $\mu = 0.12$. Although this modification affected the numerical response, the accumulation at D2 persisted, suggesting that reducing only the turbulent resistance was not sufficient to prevent the loss of mobility observed at this section.

The different numerical responses obtained at D3 and D2 resulted in a more detailed investigation of the local topography at the two monitoring sections. Although the mean channel slope between D3 and D2 is approximately 16%, the longitudinal profile along the channel reveals pronounced local variations in bed inclination. In particular, both monitoring sections are located in proximity to marked topographic steps, as illustrate in **Figure 5.2d-e**, so that the flow conditions at the stage radar sensors locations may be strongly influenced by rapid local changes in channel slope.

This effect is particularly relevant at D2 where the local bed inclination immediately downstream of the step is approximately 6°. For $\mu = 0.12$, the equivalent friction angle is higher than the channel slope immediately after D2. This fact provides an explanation for the pronounced flow deceleration and accumulation predicted by the numerical model at D2. At D3, despite the presence of a comparable local change in bed slope, the channel inclination downstream of the step does not decrease below the corresponding friction angle, and the same accumulation behavior is therefore not observed.

These results indicate that both monitoring sections are located in portions of the channel characterized by pronounced local variations in channel bed geometry. The simulated flow response is therefore strongly influenced by the local topography, with potentially significant variations in both flow depth and velocity over relatively short distances.

Based on this observation, two additional simulations were performed with a lower friction coefficient, $\mu = 0.10$, combined with $\xi = 600$ and 500 m/s^2 (**Figure 5.1**) to assess if the accumulation observed at D2 persisted when the frictional resistance is reduced. For both values of ξ, reducing μ to 0.10 prevented the accumulation previously observed at D2, indicating the strong influence of the friction coefficient on the local flow response.

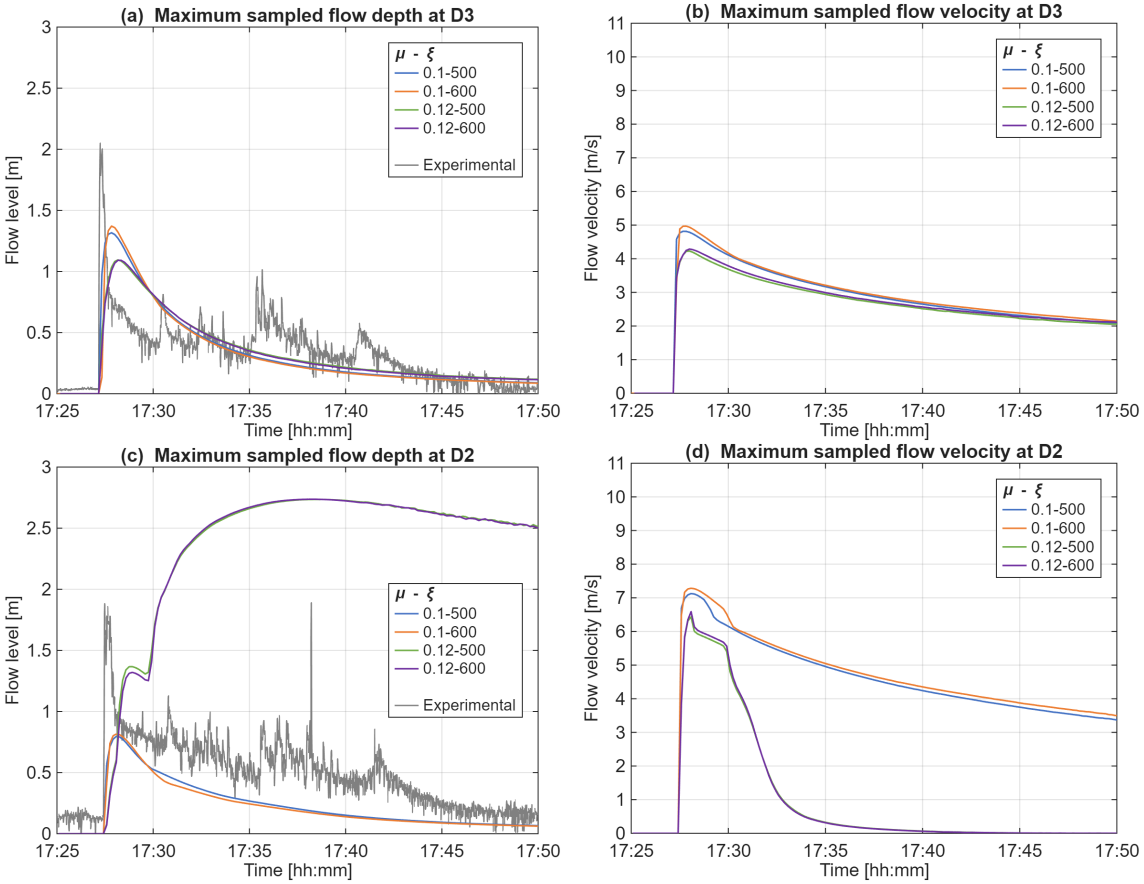


Figure 5.1: Preliminary analysis of the numerical response obtained from sampling areas centered at the actual monitoring sensor locations for the 18 July 2013 event, with comparison against recorded flow depth : **(a)** maximum sampled flow depth at D3; **(b)** maximum sampled flow velocity at D3; **(c)** maximum sampled flow depth at D2; **(d)** maximum sampled flow velocity at D2.

Given the strong local topographic variability, the sensitivity of the numerical response to the position of the sampling areas was further investigated, by moving the two sensors and their respectively circular sampling areas slightly upstream of the ones corresponding to D3 and D2, maintaining the same radius of 1 m but positioning each area entirely before the corresponding step (**Figure 5.2**). These virtual displacements were introduced exclusively as a diagnostic test and did not represent a modification of the actual monitoring locations. The purpose was to study the influence of local topography on flow dynamics and to verify if the numerical response was physically consistent with the change in bed inclination.

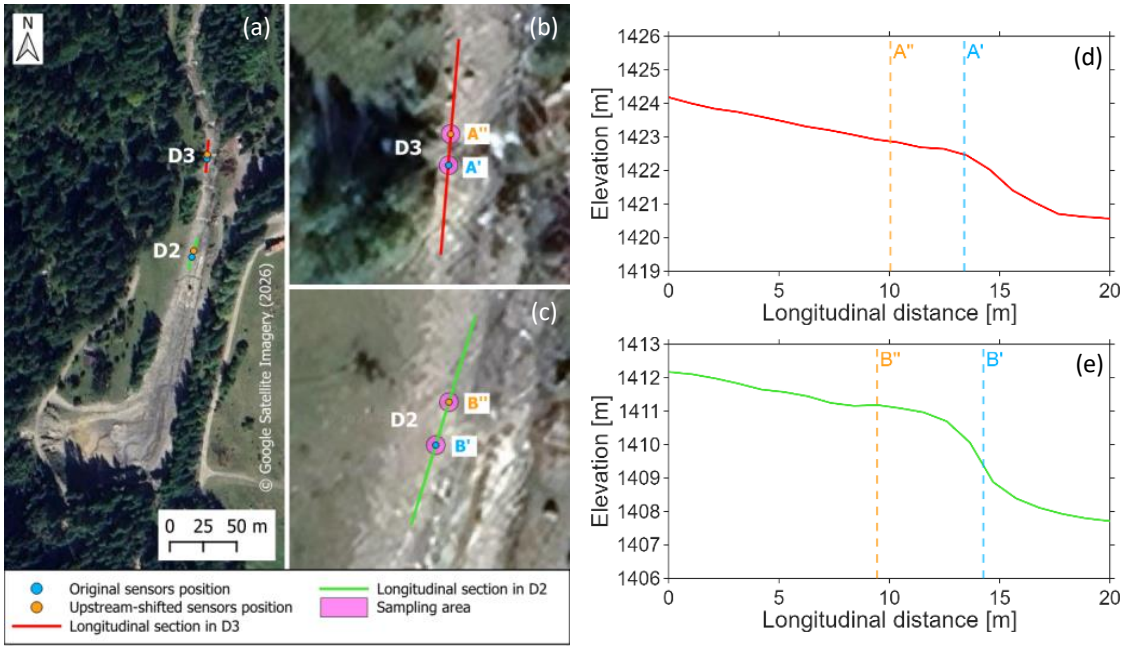


Figure 5.2: Location of the D3 and D2 monitoring sections and local channel topography: **(a)** overview of the instrumented channel reach; **(b, c)** detail of the original and upstream-shifted stage radar sensors and their relative sampling areas respectively at D3 and D2; **(d, e)** corresponding longitudinal elevation profiles highlighting the position of the local topographic steps and stage radar sensors position.

At both monitoring sections, moving the sampling area upstream of the topographic step produces a modification of the numerical response, as shown in **Figure 5.3**. The predicted velocities decrease due to the lower local channel slope upstream the topographic steps, while the corresponding flow depths generally increase. The simultaneous decrease in velocity and increase in flow depth is consistent with flow continuity, since, for comparable discharge and channel geometry, a lower flow velocity is associated with a greater flow depth. At D2, the excessive accumulation observed at the actual monitoring section is significantly reduced.

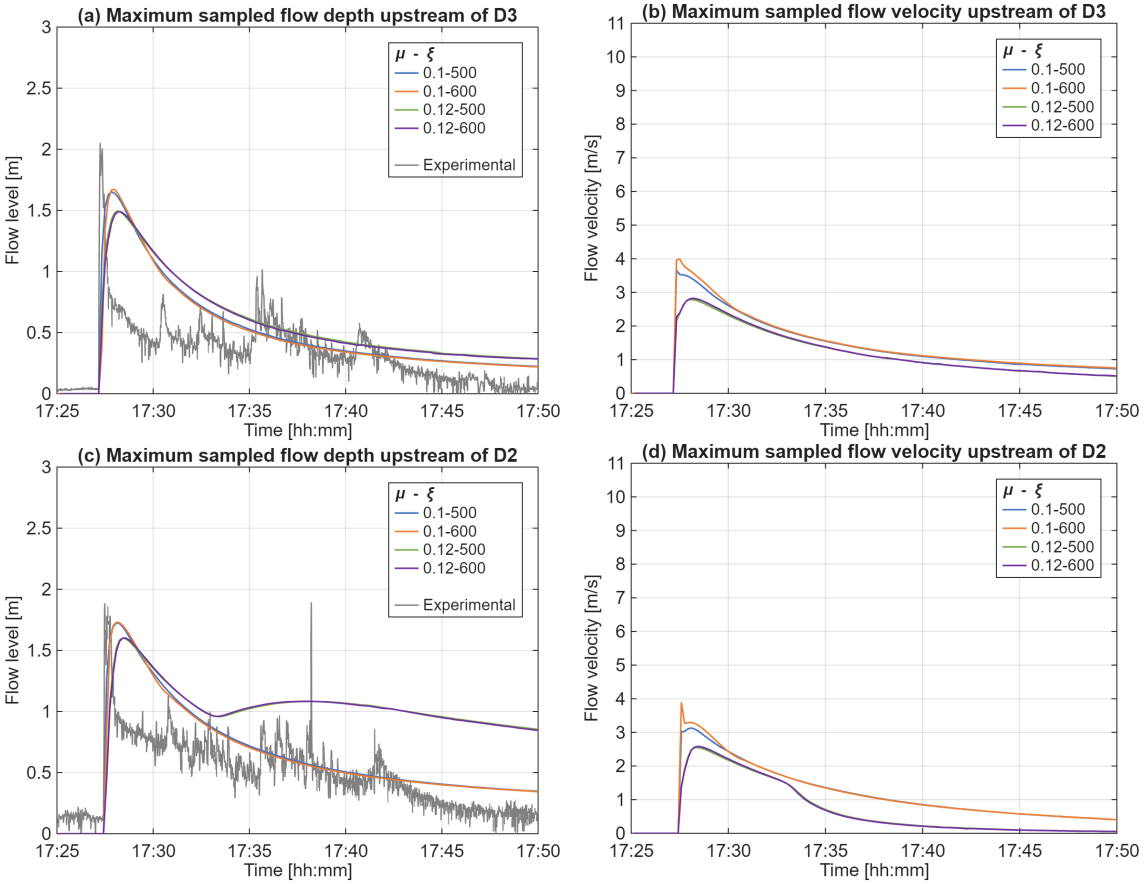


Figure 5.3: Preliminary analysis of the numerical response obtained from sampling area shifted upstream of the monitoring sensor locations for the 18 July 2013 event, with comparison against recorded flow depth: **(a)** maximum sampled flow depth upstream of D3; **(b)** maximum sampled flow velocity upstream of D3; **(c)** maximum sampled flow depth upstream of D2; **(d)** maximum sampled flow velocity upstream of D2.

The response obtained by performing the same virtual displacement in D3, where no accumulation was observed, is particularly relevant as it indicates that the changes in h and v reflect a general sensitivity of the numerical solution to local topography. The virtual displacement therefore provides a diagnostic assessment of the model response, rather than representing an alternative monitoring location for the calibration.

This preliminary analysis highlights an important difference between the objectives of the present study and those of **Finis et al.** (**2017**). The parameter combination adopted in their work was assessed with respect to the overall reproduction of the event, including its maximum flow depth and velocity, whereas the present study focuses specifically on the local and time-dependent dynamic response of the debris flow within the instrumented channel reach. The availability of stage radar measurements at D3 and D2 allows to evaluate the temporal evolution of the simulated flow by a direct comparison with the recorded stage hydrographs. As a consequence, a combination of parameters suitable for reproducing the overall characteristics of the event does not necessarily provide the same level of agreement when the analysis focuses on the local flow dynamics. For this reason a dedicated parametric analysis was performed to investigate the influence of the

two Voellmy rheological parameters on the flow behavior and to identify a combination capable of reproducing the monitored debris-flow response at both D3 and D2.

The parametric analysis was performed in order to distinguish the effects of the friction and turbulence coefficients on the numerical response. The friction coefficient was first varied while maintaining ξ constant, with particular attention to the reproduction of the observed peak flow depth. Subsequently, the influence of the turbulence coefficient was investigated at fixed μ, focusing primarily on the post-peak evolution of the hydrograph. Overall, the investigated parameter ranges were $\mu = 0.05$–0.10 and $\xi = 100$–$1000\ \mathrm{m/s^2}$. The combination $\mu = 0.10$ and $\xi = 500\ \mathrm{m/s^2}$ was selected as the starting point of the analysis. Keeping ξ constant, the friction coefficient was progressively reduced to investigate its influence on the temporal evolution of h and v and, in particular, on the magnitude of the simulated peak flow depth. At the original monitoring locations, decreasing μ generally increases the simulated velocity, consistently with the reduction in frictional resistance. A systematic influence is also observed on the flow depth: decreasing μ increases the simulated peak of h, although the magnitude of this effect progressively reduces for the lowest investigated values, indicating a tendency of the peak response to stabilize. Results are shown below in **Figure 5.4**.

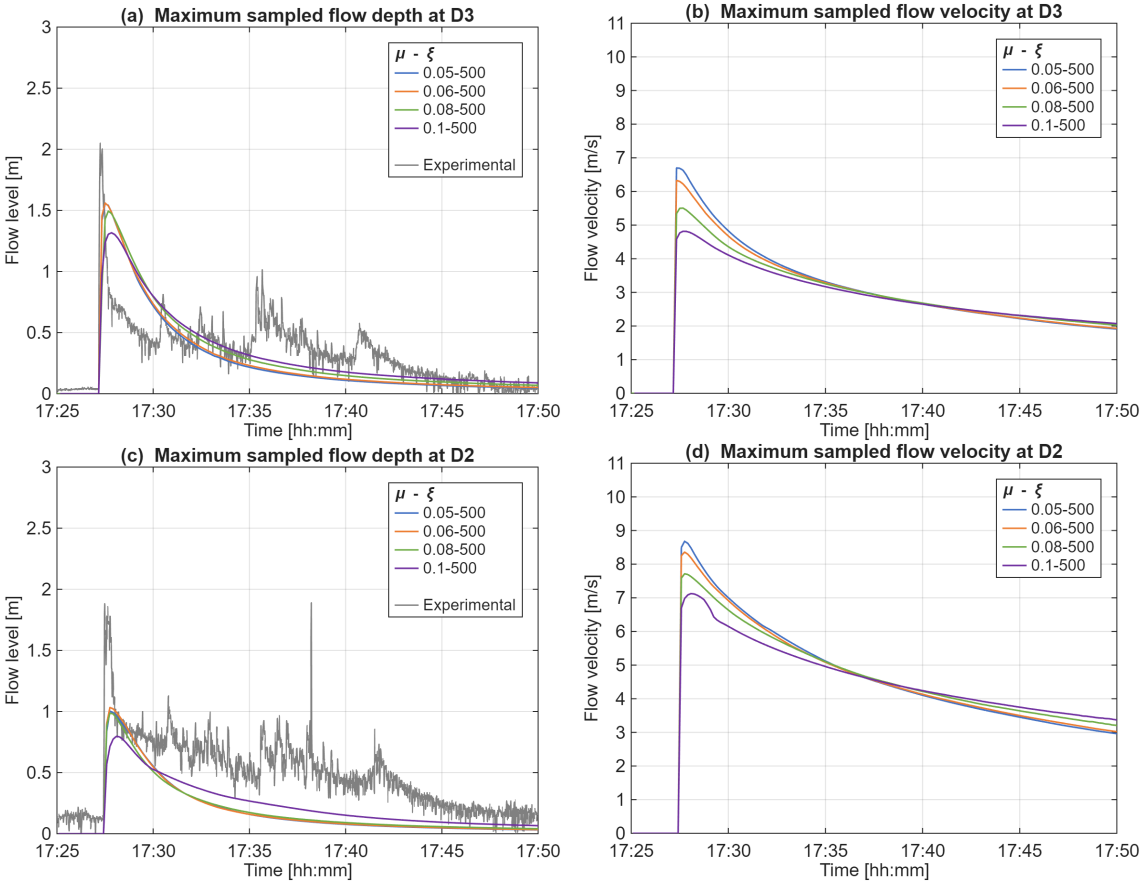


Figure 5.4: Parametric analysis of the numerical response obtained from sampling areas centered at the actual monitoring sensor locations for the 18 July 2013 event varying μ at fixed ξ, with comparison against recorded flow depth: **(a)** maximum sampled flow depth at D3; **(b)** maximum sampled flow velocity at D3; **(c)** maximum sampled flow depth at D2; **(d)** maximum sampled flow velocity at D2.

The same parameter combinations were then examined using the sampling areas located upstream of the topographic steps. Results are shown in **Figure 5.5**. As already observed in the preliminary analysis, the change in the position of the sampling area substantially affects the local response. In particular, the dependence of the peak flow depth on μ differs from that observed at the actual sensor locations: lower values of μ produce peak depths that are comparable to or lower than those obtained for higher values of the friction coefficient, rather then the progressive increase observed at the on-step locations. This behavior indicates that the effect of the rheological parameters on local flow depth cannot be interpreted independently of the channel topography, since changes in bed slope affect the local relationship between flow depth and velocity. Overall, the predicted velocities are lower than those obtained at the actual sensor locations, consistently with the lower local channel slope. However, the effect of μ on velocity remains consistent, with lower friction coefficients producing greater flow mobility and, consequently, higher velocities.

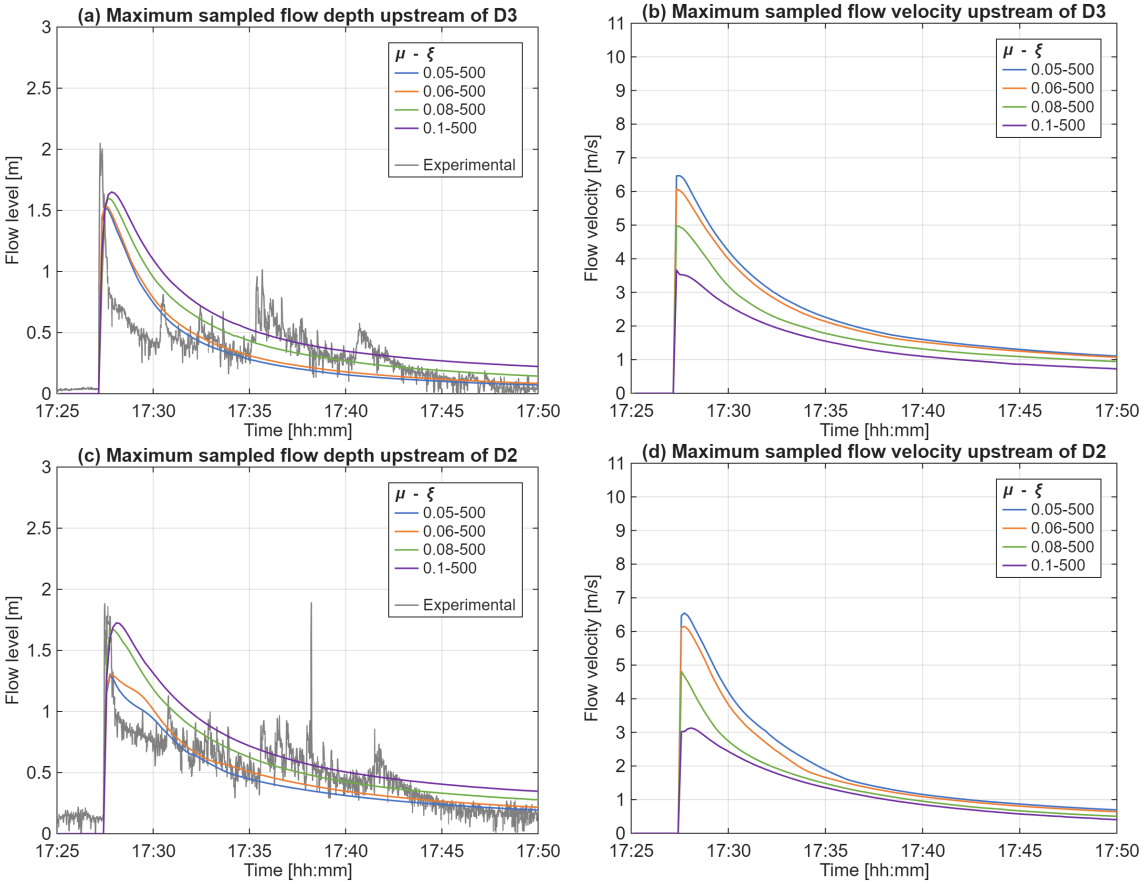


Figure 5.5: Parametric analysis of the numerical response obtained from sampling areas shifted upstream of the monitoring sensor locations for the 18 July 2013 event varying μ at fixed ξ, with comparison against recorded flow depth : **(a)** maximum sampled flow depth upstream of D3; **(b)** maximum sampled flow velocity upstream of D3; **(c)** maximum sampled flow depth upstream of D2; **(d)** maximum sampled flow velocity upstream of D2.

Variations in μ also affect the post-peak evolution, with higher friction coefficients generally producing a slower decrease in flow depth. However, the recession limb is also influenced by the turbulence coefficient; for this reason, its effect was investigated in greater detail by varying ξ.

Once the sensitivity to the friction coefficient had been established, $\mu = 0.06$ was selected as a reference value to isolate the influence of the turbulence coefficient. At this value, the simulated peak flow depth showed limited susceptibility to further reductions in μ, making it suitable for investigating more clearly the effect of ξ on the temporal evolution of the numerical series. This value was therefore used as a diagnostic configuration and did not represent the final calibrated friction coefficient.

The turbulence coefficient was varied between 100 and 1000 m/s^2. Results are shown in **Figure 5.6** and **Figure 5.7**. In contrast to the previous analysis, particular attention was given to the post-peak evolution of the flow-depth curves and their ability to reproduce the recession limb of the experimental hydrographs. Increasing ξ results in higher simulated velocities at both monitoring sections and for both sampling positions. This behavior is consistent with the Voellmy rheological formulation, in which the resistance depending

on the velocity is inversely proportional to ξ: higher values of the turbulence coefficient therefore correspond to a lower resistance to motion and greater flow mobility.

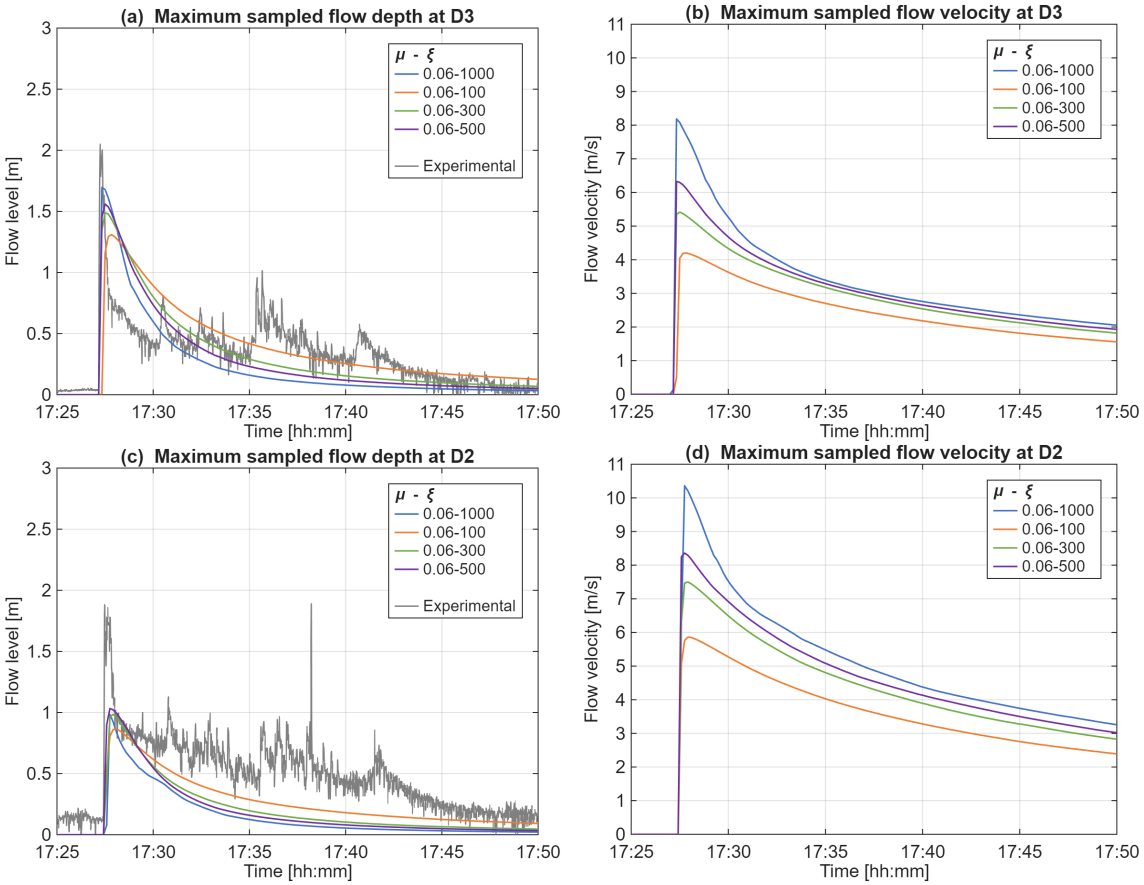


Figure 5.6: Parametric analysis of the numerical response obtained from sampling areas centered at the actual monitoring sensor locations for the 18 July 2013 event varying ξ at fixed μ, with comparison against recorded flow depth : **(a)** maximum sampled flow depth at D3; **(b)** maximum sampled flow velocity at D3; **(c)** maximum sampled flow depth at D2; **(d)** maximum sampled flow velocity at D2.

The influence on flow depth is strongly dependent on local topography. At the original monitoring locations, increasing ξ generally produces a more pronounced peak followed by a steeper post-peak decrease, resulting in a sharper hydrograph.

On the contrary, when the response is sampled upstream of the topographic steps, the ordering of the peak depths changes. A further effect of moving the sampling areas upstream is the increase in the simulated post-peak flow depths. At both D3 and D2, this generally improves the agreement between the numerical recession limb and the experimental hydrograph. These results also demonstrate that the local response results from the combined influence of rheology and bed geometry rather than from the rheological parameters alone.

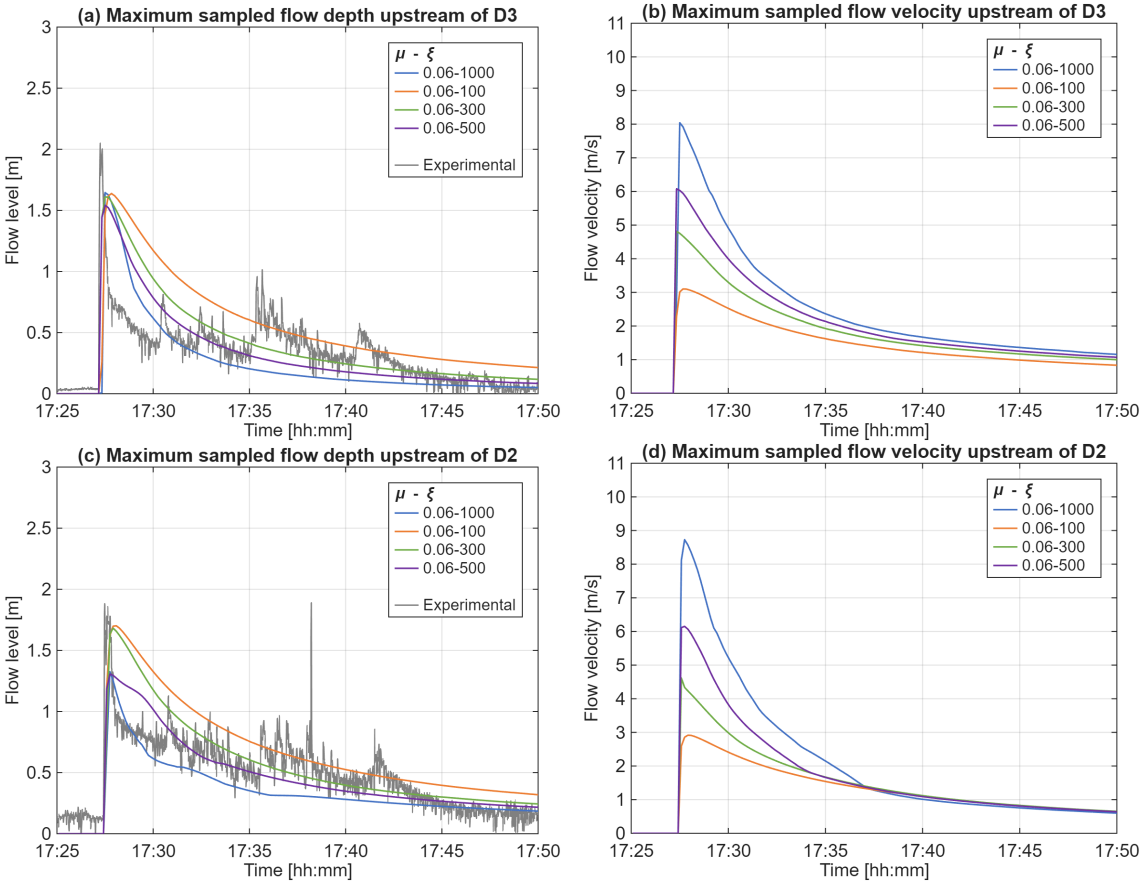


Figure 5.7: Parametric analysis of the numerical response obtained from sampling areas shifted upstream of the monitoring sensor locations for the 18 July 2013 event varying ξ at fixed μ, with comparison against recorded flow depth : **(a)** maximum sampled flow depth upstream of D3; **(b)** maximum sampled flow velocity upstream of D3; **(c)** maximum sampled flow depth upstream of D2; **(d)** maximum sampled flow velocity upstream of D2.

Flow depth was used as the primary calibration variable because continuous stage measurements recorded at site were available at both monitoring sections. Velocity provided an additional criterion for evaluating the consistency of the simulations. For each parameter combination, the mean propagation velocity between D3 and D2 was estimated from the travel time of the corresponding simulated peak, following the same procedure previously described in Section 3.6:

$$v_{\mathrm{D3-D2}} = \frac{L_{\mathrm{D3-D2}}}{\Delta t_{\mathrm{D3-D2}}} \tag{5.1}$$

where L_{D3-D2} is the distance between the two monitoring sections and Δt_{D3-D2} is the travel time of the corresponding peak from D3 to D2. The peaks used to determine the numerical travel times were identified from the flow-depth time series extracted at the actual sensor locations. The resulting numerical velocities (**Table 5.1**) were compared with the experimental value of 5.7 m/s estimated from the propagation of the debris-flow peak between the two monitoring sections and obtained from a peak travel time of 14 s over the 80 m distance between D3 and D2.

Table 5.1: Numerical travel times of the debris-flow peak between D3 and D2 and corresponding mean propagation velocities for the investigated Voellmy parameter combinations.

μ	ξ [m/s^2]	$\Delta t_{\mathrm{D3-D2}}$ [s]	$v_{\mathrm{D3-D2}}$ [m/s]
0.05	500	10	8.0
0.06	500	10	8.0
0.08	500	10	8.0
0.10	500	20	4.0
0.06	100	30	2.7
0.06	300	20	4.0
0.06	1000	10	8.0

Since the numerical outputs were saved at 10 s intervals, simulated peak arrival times are constrained by the same temporal resolution. This is reflected in the estimated travel times, which occur approximately in multiples of 10 s, resulting in discrete propagation-velocity estimates of approximately 8.0, 4.0, and 2.7 m/s. Consequently, these values cannot reproduce the temporal precision of the experimental measurements and should not be interpreted as precise estimates of the propagation velocity. Nevertheless, most simulations provide velocities of the same order of magnitude as the experimental value of approximately 5.7 m/s. For this reason, the estimated propagation velocities were used as an additional consistency criterion rather than as the primary calibration target.

The two parametric analysis stages were not intended to determine the optimal values of μ and ξ independently. Rather, they were used to characterize their respective influence on the numerical response. The final parameter combination was therefore selected by considering simultaneously the reproduction of the peak flow depth, the post-peak evolution of the hydrograph at both monitoring sections, the influence of the local topographic steps, and the consistency of the simulated propagation velocities.

On this basis, the combination $\mu = 0.08$ and $\xi = 500$ m/s^2 provided the best overall reproduction of the monitored debris-flow response and was selected as the reference rheological parameter set for the subsequent analyses. The comparison in **Figure 5.8** and **Figure 5.9** further illustrates the role of local topography in the simulated response.

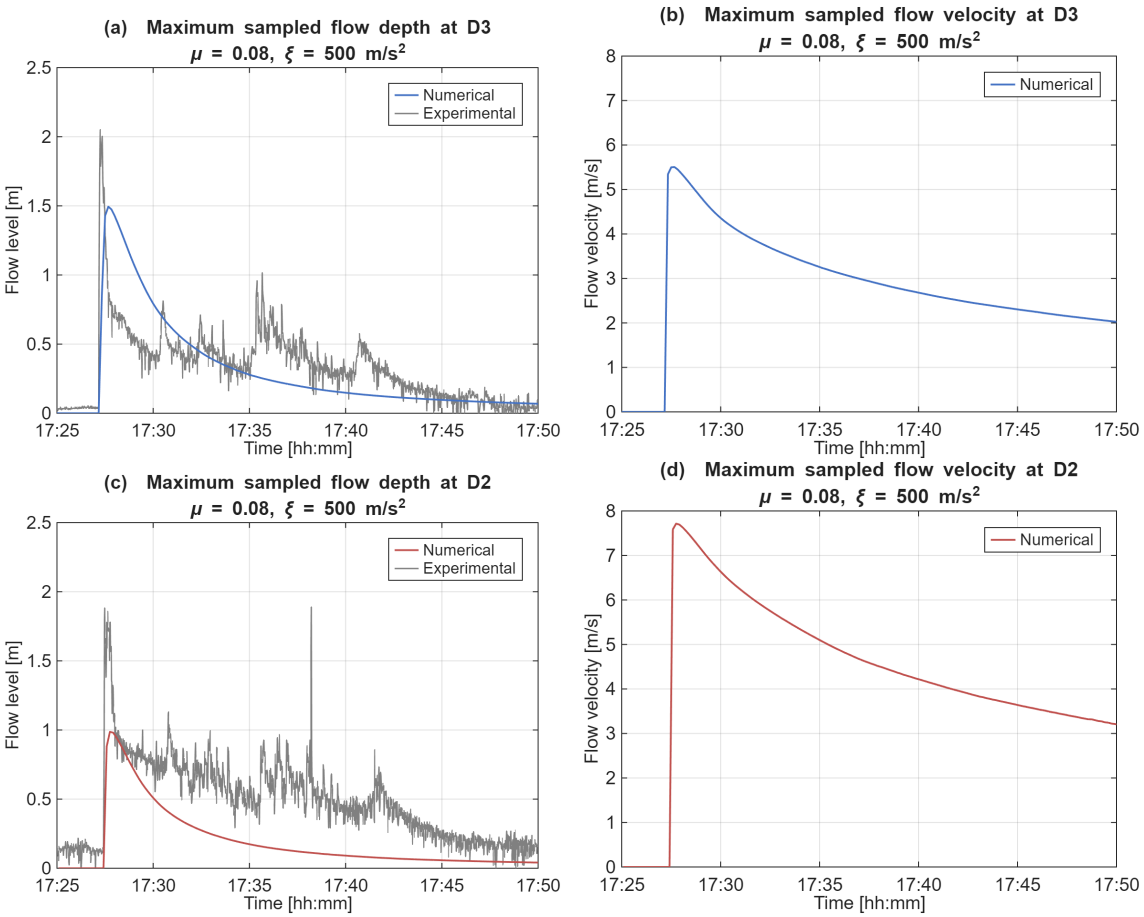


Figure 5.8: Comparison of the numerical response obtained from sampling areas centered at the actual monitoring sensor locations against recorded flow depth for the 18 July 2013 event considering $\mu = 0.08$ and $\xi = 500$ m/s^2: **(a)** maximum sampled flow depth at D3; **(b)** maximum sampled flow velocity at D3; **(c)** maximum sampled flow depth at D2; **(d)** maximum sampled flow velocity at D2.

At the actual sensor locations (**Figure 5.8**), the numerical peak flow depth obtained with the selected combination of parameters is close to the experimental peak at D3, whereas it remains lower than the recorded maximum at D2. At both monitoring sections, however, the numerical hydrographs decrease more rapidly than the recorded signal during the post-peak phase. This discrepancy is particularly evident at D2, where the experimental flow depth remains relatively higher for a longer period.

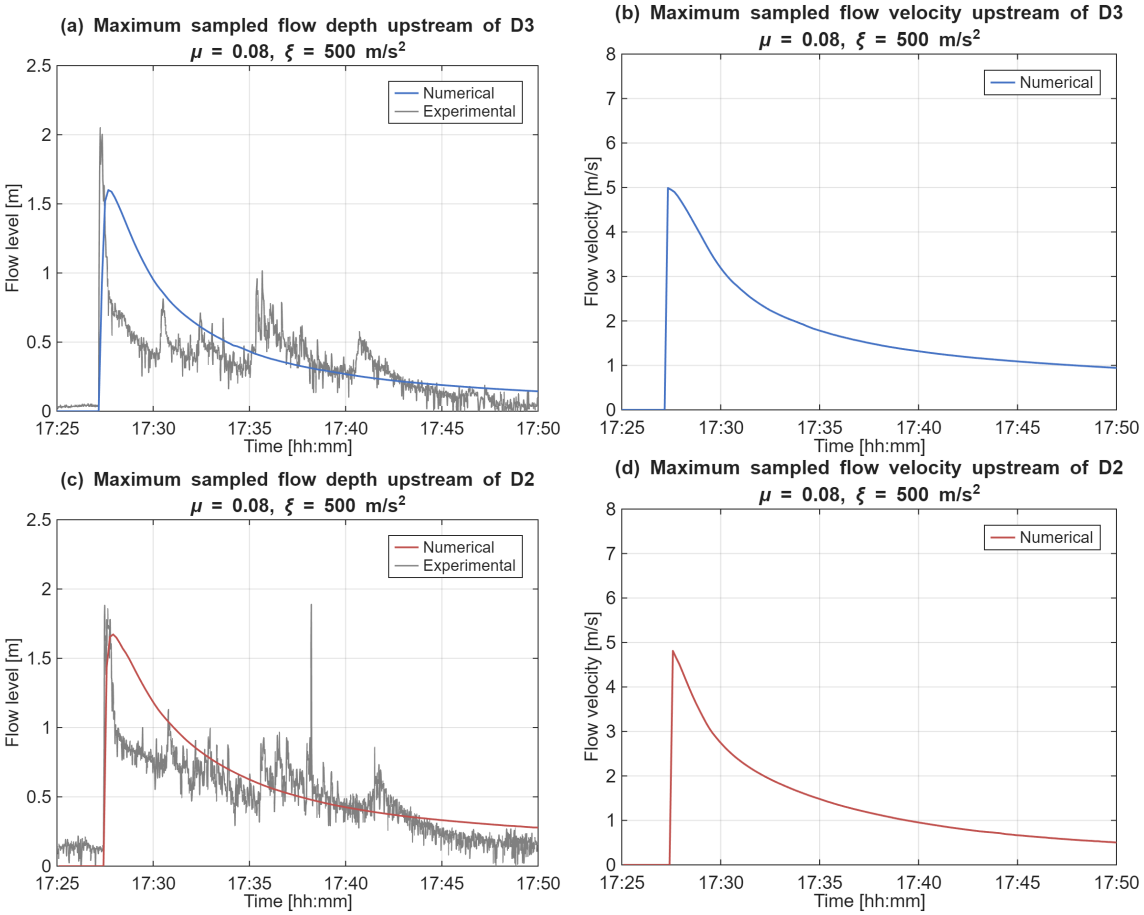


Figure 5.9: Comparison of the numerical response obtained from sampling areas shifted upstream of the monitoring sensor locations against recorded flow depth for the 18 July 2013 event considering $\mu = 0.08$ and $\xi = 500$ m/s^2: **(a)** maximum sampled flow depth upstream of D3; **(b)** maximum sampled flow velocity upstream of D3; **(c)** maximum sampled flow depth upstream of D2; **(d)** maximum sampled flow velocity upstream of D2.

At the upstream-shifted positions (**Figure 5.9**), the numerical response changes substantially. In particular, the simulated peak at D2 becomes closer to the recorded one, whereas at D3 the peak flow depth remains approximately unchanged. At both monitoring sections, the subsequent decrease in flow depth becomes more gradual and better follows the overall post-peak evolution of the experimental hydrograph. In addition, these differences demonstrate that the local values of flow depth and velocity are strongly affected by the position of the sampling area relative to the topographic steps. Overall, the relative agreement with the recorded signal varies depending on the sampling position and the phase of the hydrograph. The parameters selection was therefore based on the overall numerical response, considering the behavior at both monitoring sections and across the different phases of the hydrograph.

Considering also the local flow velocities, the experimental propagation velocity of approximately 5.7 m/s falls within the range of the simulated peak velocities obtained at D3 and D2. Although the two quantities are not directly equivalent, since the experimental value represents a propagation velocity between the monitoring sections whereas the

numerical values represent local flow velocities, their comparable magnitude provides an additional indication of the consistency of the simulated flow response.

Given the overall reproduction of the monitored debris-flow response, the selected combination of parameters ($\mu = 0.08$ and $\xi = 500\ \mathrm{m/s^2}$) was subsequently adopted for the analysis of flow runout within the retention basin for the same event and, without further calibration, for the simulation of the 26 July 2019 event.

5.2 18 July 2013 event: deposition and check-dam configurations

After analyzing the flow response within the instrumented reach, the selected rheological parameters ($\mu = 0.08$ and $\xi = 500\ \mathrm{m/s^2}$) were used to investigate the behavior of the simulated debris flow within the downstream retention basin and its interaction with the open filter check dam. As described in the previous chapter, two configurations of the structure were considered: a closed configuration, in which the barrier was represented as a continuous obstacle, and an open configuration including the central slit modeled as a rectangular opening. This second stage of the analysis therefore focuses on the influence of the barrier configuration on flow accumulation and propagation rather than on the calibration of the rheological parameters.

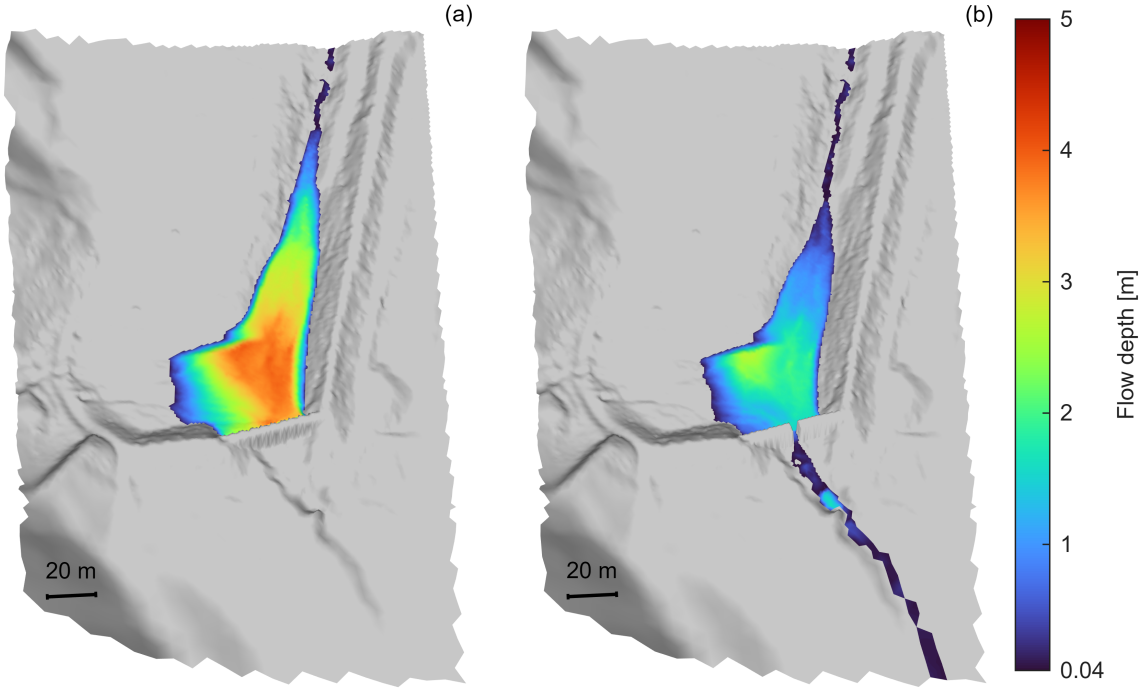


Figure 5.10: Three-dimensional view of the final flow-depth distribution within the retention basin for the 18 July 2013 event: **(a)** closed barrier configuration; **(b)** open barrier configuration.

The three-dimensional representation in **Figure 5.10** provides an overall view of the interaction between the simulated mass and the barrier. In the closed configuration, the flowing material is retained upstream of the structure, resulting in substantial accumulation within the deposition basin. When the opening is introduced, part of the material is able to pass through the slit and continue into the downstream channel, while the remaining material accumulates upstream of the barrier. The comparison clearly shows the different behavior produced by the two representations of the structure.

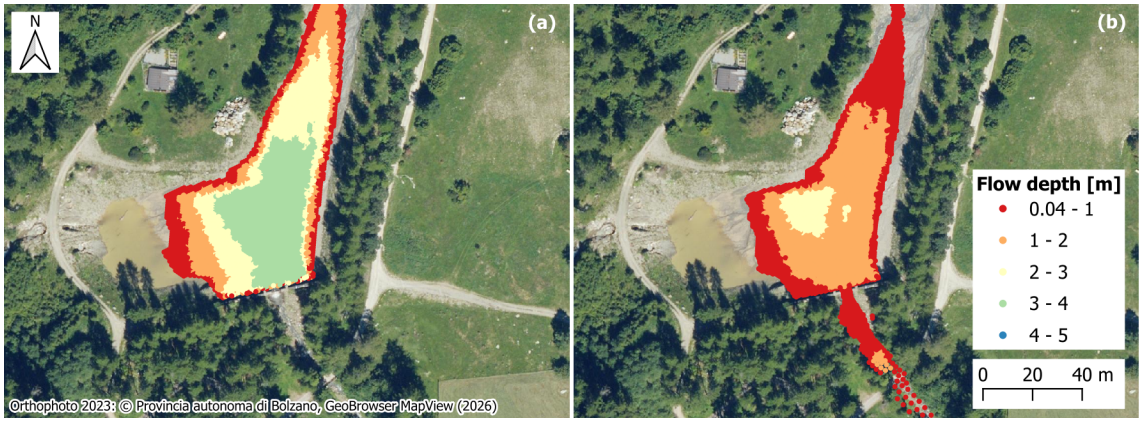


Figure 5.11: Plan view of the final flow-depth distribution within the retention basin for the 18 July 2013 event: **(a)** closed barrier configuration; **(b)** open barrier configuration.

The plan view of the final flow-depth distribution in **Figure 5.11** allows the differences in accumulation within the basin to be examined more clearly. The closed configuration is characterized by a larger area of relatively high flow depth immediately upstream of the barrier, consistently with the complete obstruction of the flow path. In the open configuration, the possibility of material passing through the slit modifies the final distribution within the basin, allowing the simulated flow to continue downstream of the structure. However, a pronounced convergence of the accumulated material toward the slit is not clearly visible in the final flow-depth distribution.

Since the final flow-depth distribution presented above represents only the state of the simulated mass within the retention basin at the end of the event, it does not provide complete information on the spatial extent and maximum flow depths experienced during propagation. For this reason, the maximum flow depth recorded at each mesh node throughout the simulation was also considered. At the final simulation time, $h_{\max}$ represents the maximum value reached locally during the entire simulated event rather than the instantaneous flow depth at that time.

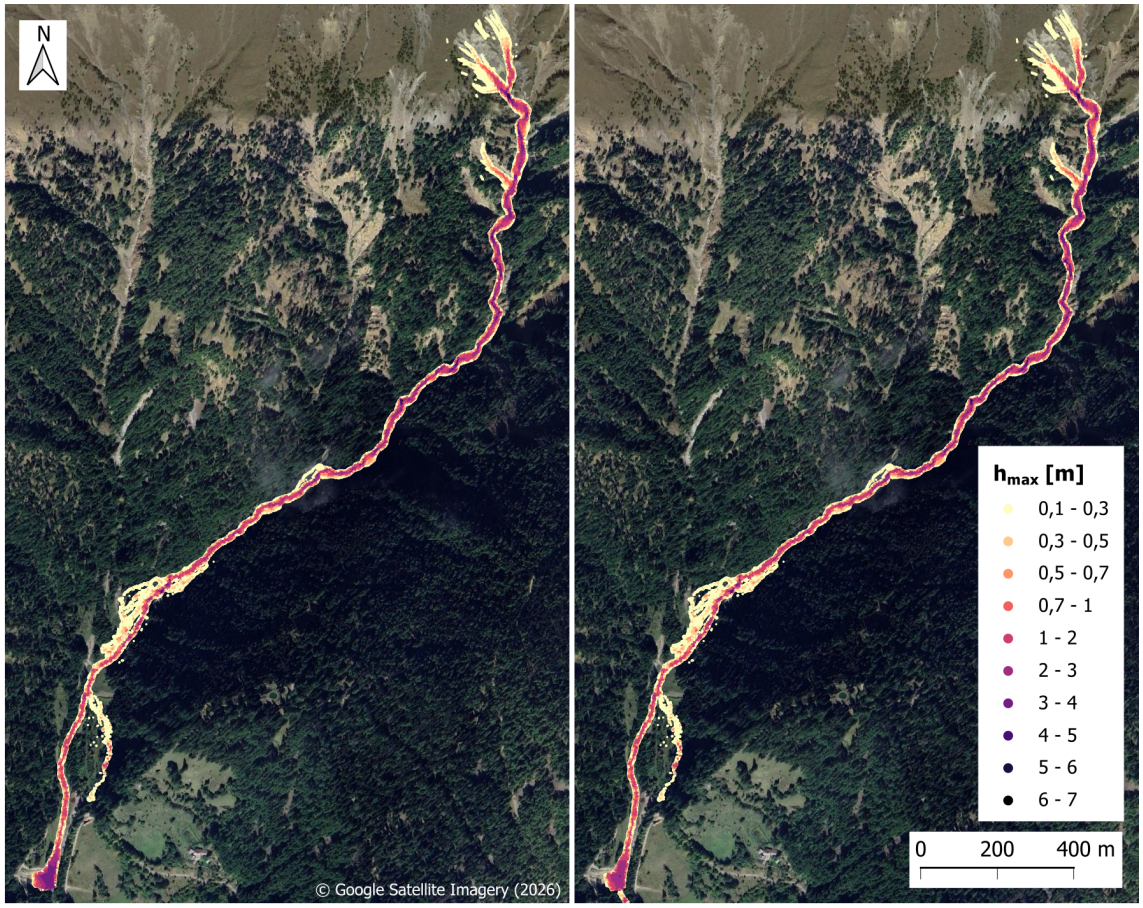


Figure 5.12: Maximum flow depth reached during the simulation of the 18 July 2013 event for (a) the closed and (b) the open barrier configuration.

The spatial distribution of $h_{\max}$ in **Figure 5.12** provides an overall representation of the propagation pathway of the simulated debris flow from the source area to the retention basin. As described in Section 4.2, the two configurations differ only at the barrier. The influence of the barrier conformation becomes evident at the retention basin, where the closed set-up prevents further propagation downstream, whereas the open one allows part of the flow to pass through the slit and continue along the downstream channel.

To further examine the local interaction between the debris flow and the barrier opening, the distribution of the maximum flow velocity, $v_{\max}$, within the retention basin was also analyzed. Results are shown in **Figure 5.13**.



Figure 5.13: Maximum flow velocity reached within the retention basin during the simulation of the 18 July 2013 event for (a) the closed and (b) the open barrier configuration.

In the open configuration (**Figure 5.13b**), the v_{max} distribution reveals a preferential flow pathway toward the slit, with higher maximum velocities progressively concentrating toward the opening and continuing into the downstream channel. This convergent pattern is considerably less evident in the final flow-depth distribution presented above (**Figure 5.11b**). This difference can be related to the distinct information represented by the two variables. The final flow depth describes the state of the simulated mass at the end of the event and is therefore mainly associated with the material accumulating within the basin. Instead, v_{max} represent the maximum velocity experienced at each location throughout the simulation and can therefore preserve the signature of the transient convergence of the moving material toward the opening.

These results complete the analysis of the 18 July 2013 event, extending the assessment from flow propagation within the instrumented channel reach to the interaction of the simulated debris flow with the downstream retention structure.

5.3 26 July 2019 event: assessment of parameter transferability

The selected rheological parameter set was subsequently applied, without further calibration, to the 26 July 2019 event to assess its transferability to a different debris-flow event within the same catchment. The same 2011 DTM adopted for the simulation of the 2013 event was also used for the 2019 event as described in Section 4.3. Consequently possible morphological changes in the channel occurring between the topographic survey and the 2019 event are not represented in the numerical model. Despite occurring along the same channel, the 2019 event differed from the 2013 event in terms of flow characteristics and total mobilized volume, as described in Chapter 3. The application of the previously calibrated parameters therefore provides an opportunity to evaluate if the rheological representation identified for the 2013 event can reproduce the monitored response of a different debris-flow event in the same basin.

The numerical response was evaluated following the same procedure adopted for the 2013 event, by comparing the maximum flow depths sampled around the monitoring locations with the corresponding radar stage measurements. At D3 and D2, the results obtained at the actual sensor locations were complemented by those corresponding to the upstream-shifted virtual positions, in order to account for the influence of the local topographic variations identified during the analysis of the 2013 event. As for the previous event, the corresponding mean sampled values are reported in Appendix A.

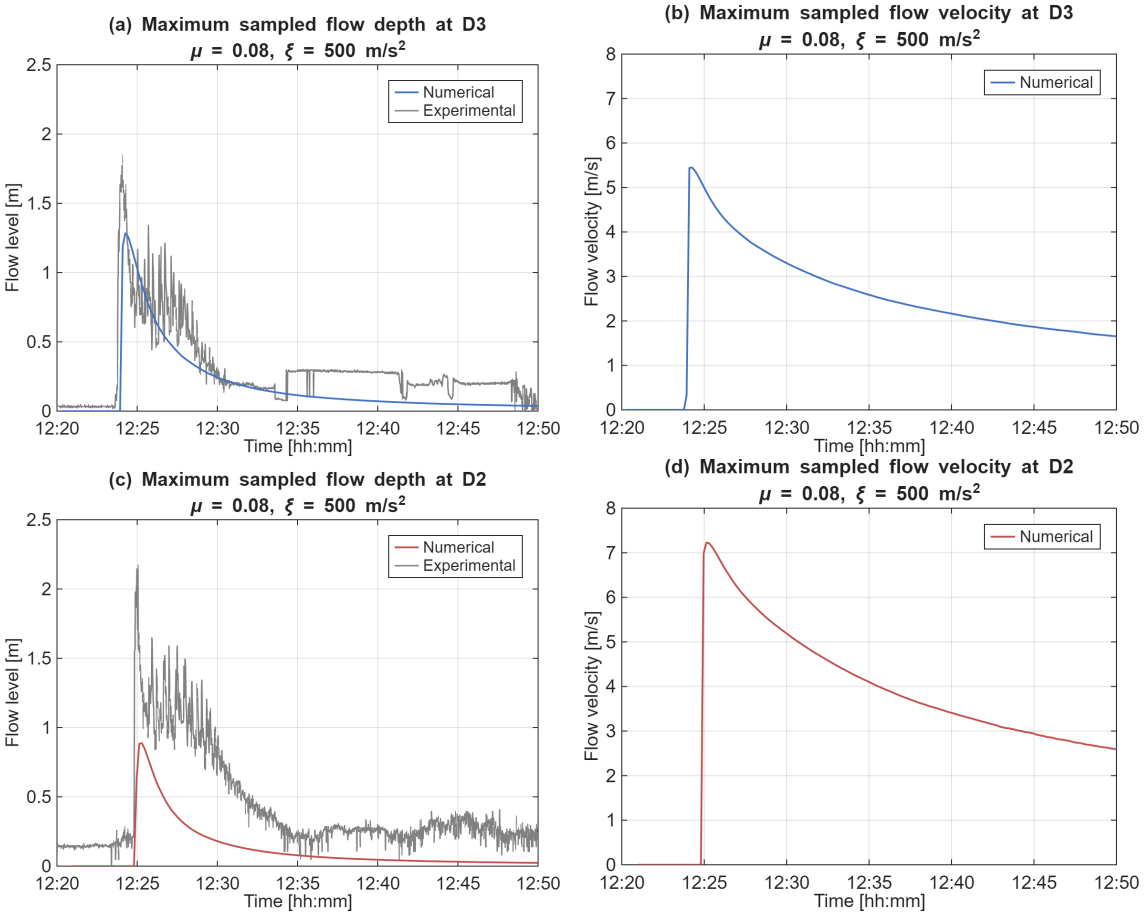


Figure 5.14: Comparison of the numerical response obtained from sampling areas centered at the actual monitoring sensor locations against recorded flow depth for the 26 July 2019 event using the rheological parameters calibrated on the 2013 event: **(a)** maximum sampled flow depth at D3; **(b)** maximum sampled flow velocity at D3; **(c)** maximum sampled flow depth at D2; **(d)** maximum sampled flow velocity at D2.

At the actual sensor locations (**Figure 5.14**), the numerical response shows different levels of agreement at D3 and D2. At D3, the simulated hydrograph captures the timing of the main peak flow depth and its following decreasing trend, although the numerical peak remains lower than the recorded one. At D2, the difference in peak magnitude is more pronounced, with the numerical model substantially underestimating the maximum recorded flow depth. The numerical hydrograph also decreases more rapidly immediately after the peak, while the experimental signal remains at higher flow depths.

As observed for the 2013 event, the local topographic conditions at the monitoring sections have a significant influence on the sampled numerical response. The same upstream virtual displacement previously introduced for D3 and D2 was therefore also considered for the 2019 simulation.

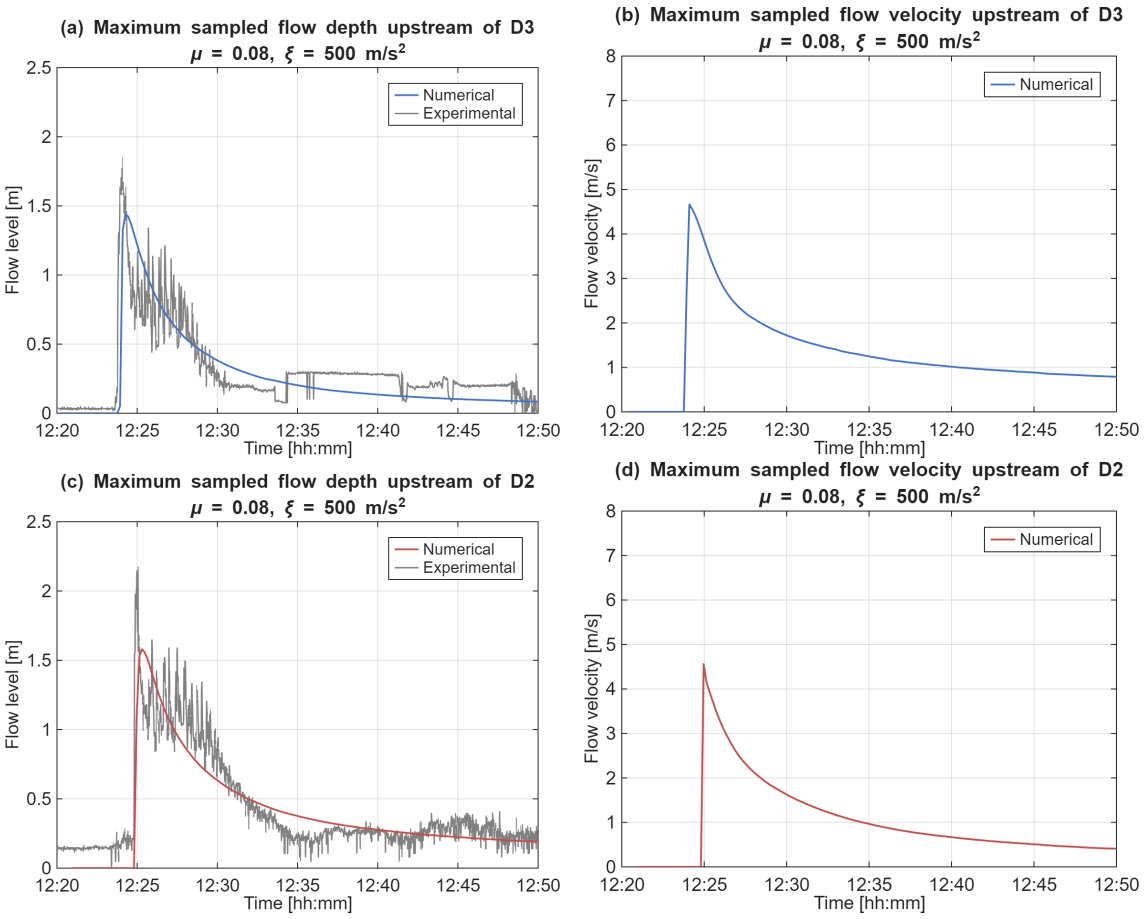


Figure 5.15: Comparison of the numerical response obtained from sampling areas shifted upstream of the monitoring sensor locations against recorded flow depth for the 26 July 2019 event using the rheological parameters calibrated on the 2013 event: **(a)** maximum sampled flow depth upstream of D3; **(b)** maximum sampled flow velocity upstream of D3; **(c)** maximum sampled flow depth upstream of D2; **(d)** maximum sampled flow velocity upstream of D2.

The upstream-shifted sampling positions (**Figure 5.15**) produce changes that are consistent with the sensitivity to local topography identified for the 2013 event. At D3, the magnitude of the main numerical peak remains comparable to that obtained at the actual sensor location, while some differences are observed in the subsequent evolution of the hydrograph. At D2, the effect is considerably more pronounced: the simulated peak flow depth increases and becomes substantially closer to the recorded maximum, while the subsequent recession limb also follows the experimental hydrograph more closely.

The comparison between the two sampling positions therefore confirms that the numerical response of the 2019 event is strongly influenced by the local channel topography

represented in the numerical model. As discussed for the 2013 event, the upstream displacement is not intended to represent an alternative monitoring location. Rather, it provides a diagnostic assessment of the sensitivity of the numerical response to pronounced local variations in channel-bed topography. For the 2019 event, however, the interpretation of these local effects should also account for the use of the 2011 DTM, which does not include possible morphological changes that occurred in the monitored reach between the topographic survey and the simulated event. Indeed, ten debris-flow events occurred within the catchment during this period (see **Table 3.1**), potentially contributing to changes in the local channel morphology.

The 2019 event also provides an additional monitoring location for assessing the transferred combination of parameters, since the upstream monitoring section D4 became operational in 2019. For this reason, D4 provides an independent comparison at a monitoring location that was not involved in the calibration procedure.

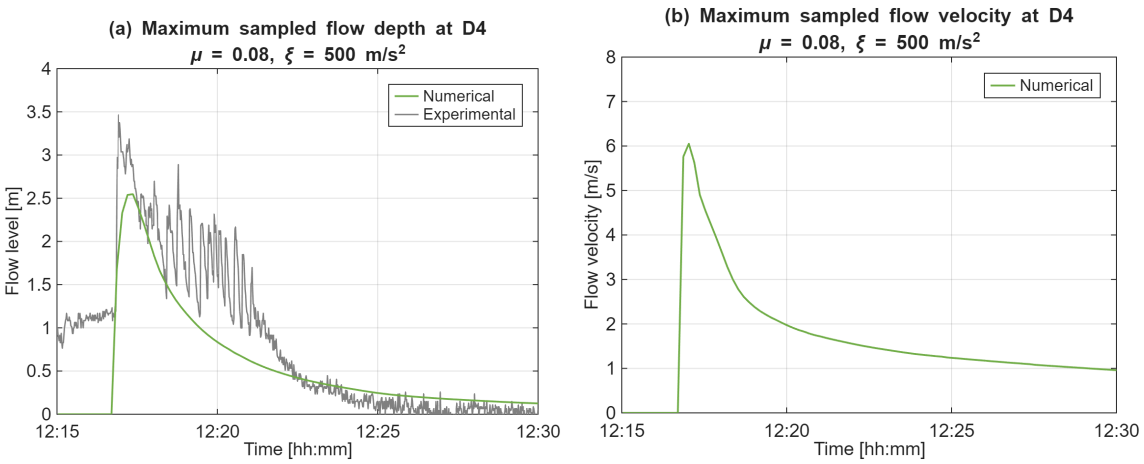


Figure 5.16: Comparison of the numerical response at monitoring section D4 against the recorded flow depth for the 26 July 2019 event using the rheological parameters calibrated on the 2013 event: **(a)** maximum sampled flow depth at D4; **(b)** maximum sampled flow velocity at D4.

At D4 (**Figure 5.16**), the numerical simulation reproduces the overall shape of the hydrograph, although the absolute numerical and experimental values differ. In particular, the recorded level is already approximately 1 m immediately before the arrival of the main front. As described in Section 3.6, the 2019 event was characterized by a precursory surge preceding the bouldery front, which provides a physical interpretation for the non-zero stage recorded before the main peak.

Consequently, the agreement at D4 can be more appropriately assessed by considering not only the absolute peak values, but also the increase in level associated with the arrival of the main front. This variation can be expressed as

$$\Delta h = h_{peak} - h_{pre-front} \tag{5.2}$$

where h_{peak} is the level corresponding to the peak of the hydrograph and $h_{pre-front}$ represents the level immediately before the arrival of the main front. Given the fluctuations

of the recorded signal during this phase, a representative experimental pre-front level of approximately 1 m was considered. For the experimental curve, the non-zero pre-front stage is consistent with the precursory surge observed for the event. In the numerical response, the flow depth immediately before the arrival of the front is null. For this reason Δh_{num} corresponds to the numerical peak flow depth.

The experimental peak reaches 3.46 m, resulting in an experimental level increase of approximately 2.5 m with respect to the representative pre-front value. This increase can therefore be compared with the numerical peak flow depth of approximately 2.5 m. Despite the difference in absolute peak values, the comparison highlights a close agreement in the flow-depth increase associated with the passage of the main front, together with the similar overall shape of the numerical and experimental hydrographs.

Flow propagation velocity provides an additional criterion for assessing the transferability of the calibrated parameters. As described in Section 3.6, the mean propagation velocities estimated from the monitored 2019 event were approximately 1.3 m/s along the D4–D3 channel reach and 1.4 m/s along the D3–D2 segment. Considering the corresponding distances of 549 m and 80 m, respectively, the corresponding numerical propagation velocities were estimated from the travel times of the numerical peaks between the monitoring sections, following the same procedure adopted for the 2013 event (see eq. (5.1)). Results are reported in **Table 5.2**. For this calculation, the numerical flow-depth series sampled at the actual sensor locations were used.

Table 5.2: Comparison between numerical and experimental mean propagation velocities along the D4–D3 and D3–D2 channel reaches for the 26 July 2019 event. Numerical velocities were estimated from the travel times of the corresponding simulated flow-depth peaks.

Reach	Distance [m]	Δt_{num} [s]	Δt_{exp} [s]	v_{num} [m/s]	v_{exp} [m/s]
D4–D3	549	90	422	6.1	1.3
D3–D2	80	20	58	4.0	1.4

The numerical peak travel times are 90 s along the D4–D3 reach and 20 s along D3–D2, corresponding to mean propagation velocities respectively of 6.1 and 4.0 m/s. Both values are considerably higher than the corresponding experimental estimates of 1.3 and 1.4 m/s. The comparison therefore shows that the transferred parameter set produces a substantially faster propagation of the simulated flow along both monitored channel reaches.

The same tendency is observed when considering the local maximum velocities sampled at the actual monitoring sections. For the 2013 calibration event, the experimental propagation velocity was within the range of the numerical peak velocities obtained at D3 and D2 for the selected parameter combination. In contrast, for the 2019 event, the observed propagation velocities fall below the numerical velocity peaks obtained at the monitoring sections. The numerical velocity peaks reach approximately 6, 5.5, and 7 m/s respectively at D4, D3, and D2 (**Figure 5.14** and **Figure 5.16**), and therefore remain above the observed propagation velocities. Although the local sampled velocity peaks and

the mean propagation velocities derived from travel times represent different quantities and should not be directly equated, both comparisons indicate that the simulated flow is characterized by higher velocities than those observed during the 2019 event.

These results indicate that the rheological parameters calibrated on the 2013 event do not reproduce all aspects of the 2019 debris-flow dynamics with the same level of agreement. In particular, the differences observed in the propagation velocities suggest that the direct transferability of the calibrated Voellmy parameters between the two events is limited, despite their occurrence within the same catchment. Nevertheless, the transferred combination of parameters provides an overall satisfactory reproduction of the observed flow depths, indicating that the numerical simulation still captures some relevant features of the 2019 event.

However, the observed discrepancies cannot be exclusively attributed to differences in rheological behavior. As previously discussed, the 2019 simulation was performed using the 2011 DTM, and possible morphological changes occurring between the topographic survey and the event are therefore not represented in the numerical model. Furthermore, as discussed in Section 3.5, debris flows in the Gadria basin, despite occurring under similar catchment conditions, exhibit considerable variability from one event to another in terms of volume, material composition and flow characteristics (e.g., differences in the relative proportion of fine and coarse material), as well as surge sequence, duration, and propagation dynamics. Such variability represents an additional aspect to be considered when interpreting the transferability of a single rheological combination of parameters between different events.

6 Conclusions

This thesis addressed the back-analysis of monitored debris flows, with particular attention to the transferability of calibrated rheological parameters between different events occurring within the same basin. The Rio Gadria catchment was selected as case study because its long-term monitoring system provides detailed observations of recurrent debris-flow events, making it a valuable natural laboratory for model calibration and validation. The RASH3D depth-averaged numerical code was adopted to simulate two monitored debris flows, which occurred on 18 July 2013 and 26 July 2019, using a Voellmy rheological formulation. The 2013 event was selected as the benchmark case for rheological calibration, while the 2019 event was subsequently simulated to assess the transferability of the calibrated parameters.

For the 2013 benchmark event, particular attention was reserved to the construction of the numerical model, including the identification of the source area, the preparation of the topographic input data and the generation of an unstructured computational mesh with different levels of local refinement. The Voellmy rheology was adopted to represent the resistance acting on the moving mass through the combination of a frictional contribution, controlled by the coefficient μ, and a turbulent velocity-dependent contribution, governed by the turbulence coefficient ξ.

The rheological parameters were calibrated through a parametric analysis based on comparison between the numerical response and the flow-depth measurements recorded by the stage radar sensors at the D3 and D2 monitoring sections. The analysis showed that both rheological parameters affect the simulated flow dynamics and also highlighted the relevant influence of local topography when numerical results are compared with point-scale monitoring observations. In particular, the response extracted at the actual sensor locations differed from that obtained immediately upstream of the local topographic steps, indicating that the effects of the rheological parameters on sampled flow depth and velocity cannot be interpreted independently of the channel geometry and topography.

Among the investigated combinations, $\mu = 0.08$ and $\xi = 500\ \mathrm{m/s^2}$ provided the most satisfactory overall reproduction of the observed behavior and were therefore selected for subsequent analyses. The calibrated parameter combination reproduced the temporal evolution and magnitude of the monitored flow depths at D3 and D2 and provided a satisfactory representation of the propagation velocity of the 2013 event.

The analysis of the 2013 event was then extended to the downstream retention basin to investigate debris-flow deposition and the interaction of the simulated mass with the open filter check dam. Closed and open configurations of the barrier were considered to assess the influence of the central slit on the simulated flow. The presence of the opening produced a preferential pathway through the barrier, particularly evident in the maximum-velocity distribution, where the flow progressively converged toward the slit and continued into the downstream channel. On contrast, this transient behavior was less evident in the final flow-depth distribution, which primarily reflected the material accumulated within the basin at the end of the simulation. These analyses also highlighted the relevance of the spatial representation of the barrier opening. A local mesh refinement of 0.5 m was introduced around the slit, while the sensitivity of the local response to finer spatial resolutions remains to be investigated.

The calibrated Voellmy parameter set was then applied, without further adjustment, to the 26 July 2019 event. This second simulation provided a direct assessment of parameter transferability between two debris flows occurring within the same catchment and therefore under a comparable geological and topographic setting. The transferred parameters reproduced some relevant features of the monitored flow-depth response, but important discrepancies emerged in terms of flow velocity. The same tendency was observed in both the propagation velocities derived from the peak travel times and the local numerical velocity peaks at the monitoring sections. Although these local values and the mean propagation velocities along the channel reach represent different quantities, both comparisons consistently indicated that the simulated 2019 event propagated faster than the real event.

The comparison between the two events indicates that rheological parameters calibrated on a single debris-flow event cannot necessarily be directly transferred to another event occurring within the same catchment. This represents one of the main outcomes of the present study and emphasizes the substantial event-to-event variability that characterizes debris-flow dynamics. Differences in material composition, water content, volume and surge characteristics may contribute to different flow responses and therefore to the runout rheological behavior of individual events. At the same time, the discrepancies observed for the 2019 simulation cannot be exclusively attributed to rheology. The same 2011 topographic dataset was adopted for both events, meaning that morphological changes that occurred within the basin before the 2019 event were not represented. In addition, the monitored events at Gadria exhibit considerable variability in volume, duration, surge sequence, and propagation dynamics. For this reason, the results should be interpreted as evidence of limited direct transferability of the calibrated parameters, rather than as an indication that the rheological formulation alone is responsible for the differences between the two simulations. The application of alternative rheological formulations available in RASH3D would represent a further step toward evaluating if different representations of the resistance mechanisms can provide a more consistent description of the observed event-to-event variability.

Overall, the study highlights the scientific and practical importance of long-term monitored catchments for the investigation and numerical modeling of debris flows. The availability of observations from real events makes it possible not only to identify parameter combinations capable of reproducing individual events, but also to test their performance under different flow conditions. In this context, the Gadria monitoring site offers a particularly valuable opportunity, since numerous debris-flow events with different characteristics have been recorded over more than a decade. Long-term monitoring therefore provides an essential basis for improving the understanding of debris-flow dynamics and for progressively increasing the reliability of numerical models. In addition, the integration of field observations and numerical modeling can contribute to debris-flow hazard assessment and risk mitigation, supporting the evaluation of potentially affected areas and the development of appropriate mitigation strategies.

As a future development, the complete monitoring network available at Gadria could be used to complement the stage-radar observations used in the present study. Geophones records could be integrated with flow-depth measurements to provide additional information on debris-flow propagation and event magnitude. Moreover, the extensive instrumentation of the monitoring barrier offers the possibility of combining measurements of flow depth, surface velocity, basal forces and pore-fluid pressure with the distribution of impact forces along the vertical face of the structure. These observations could provide valuable additional constraints for the characterization of debris-flow dynamics and for the assessment of the interaction between the flow and mitigation structures.

Finally, the available hydrometeorological observations offer the possibility of extending the present runout-oriented analysis toward debris-flow triggering conditions and potentially unstable source areas. The network of rain gauges provides high-resolution precipitation measurements at different elevations and has highlighted the spatial variability of rainfall conditions within the catchment. The integration of numerical modeling with the different monitoring datasets available at Gadria could therefore contribute to a more comprehensive understanding of debris-flow triggering, propagation, deposition and interaction with mitigation structures.

A Additional results based on spatial mean value

This appendix presents the mean flow-depth and velocity results obtained from the numerical analyses described in Chapter 5. These results complement the maximum values presented in the main text.

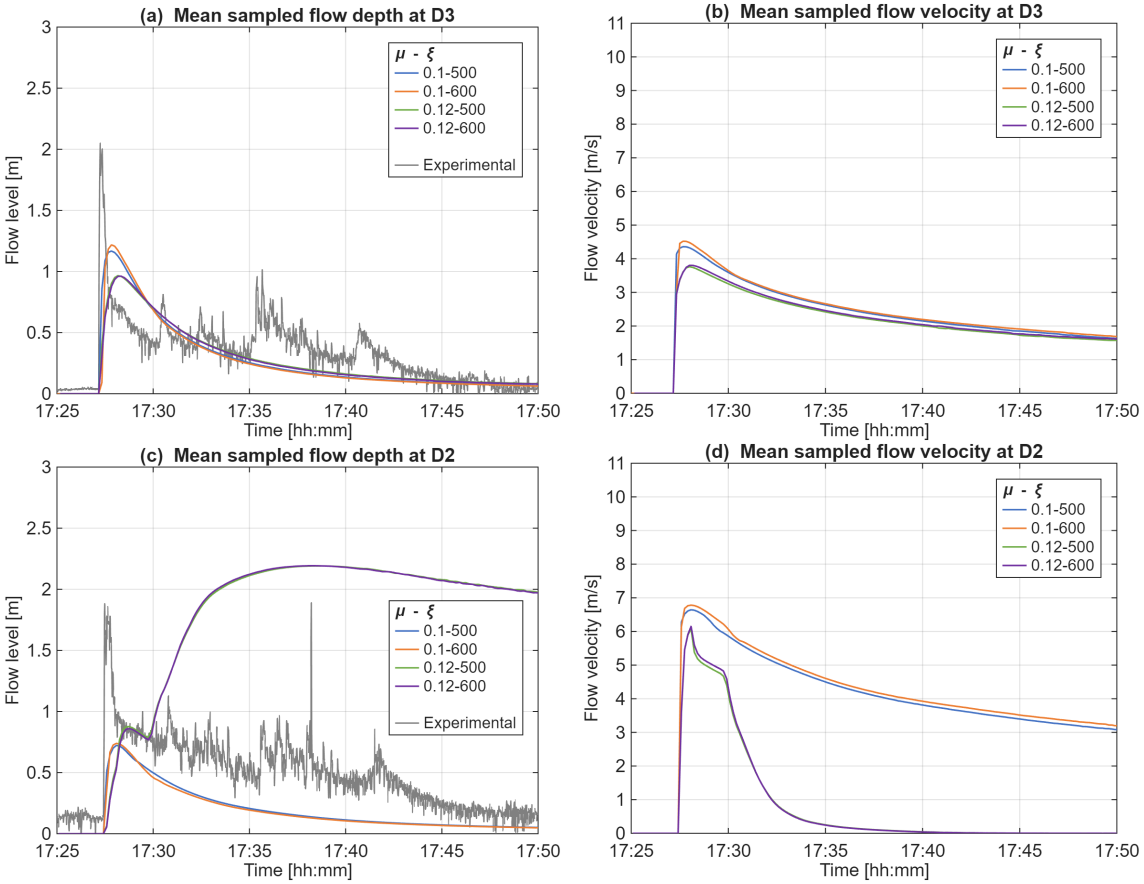


Figure A.1: Preliminary analysis of the numerical response obtained from sampling areas centered at the actual monitoring sensor locations for the 18 July 2013 event, with comparison against recorded flow depth: **(a)** mean sampled flow depth at D3; **(b)** mean sampled flow velocity at D3; **(c)** mean sampled flow depth at D2; **(d)** mean sampled flow velocity at D2.

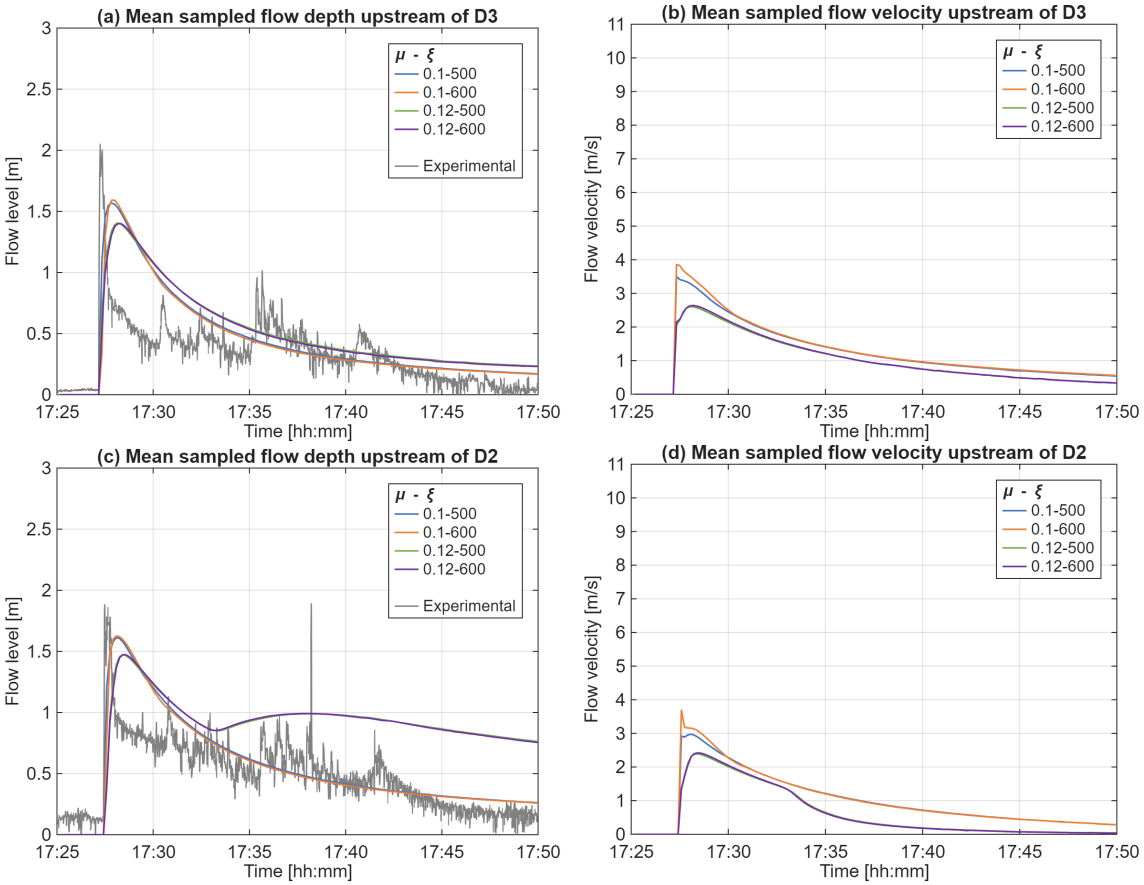


Figure A.2: Preliminary analysis of the numerical response obtained from sampling areas shifted upstream of the monitoring sensor locations for the 18 July 2013 event, with comparison against recorded flow depth: **(a)** mean sampled flow depth upstream of D3; **(b)** mean sampled flow velocity upstream of D3; **(c)** mean sampled flow depth upstream of D2; **(d)** mean sampled flow velocity upstream of D2.

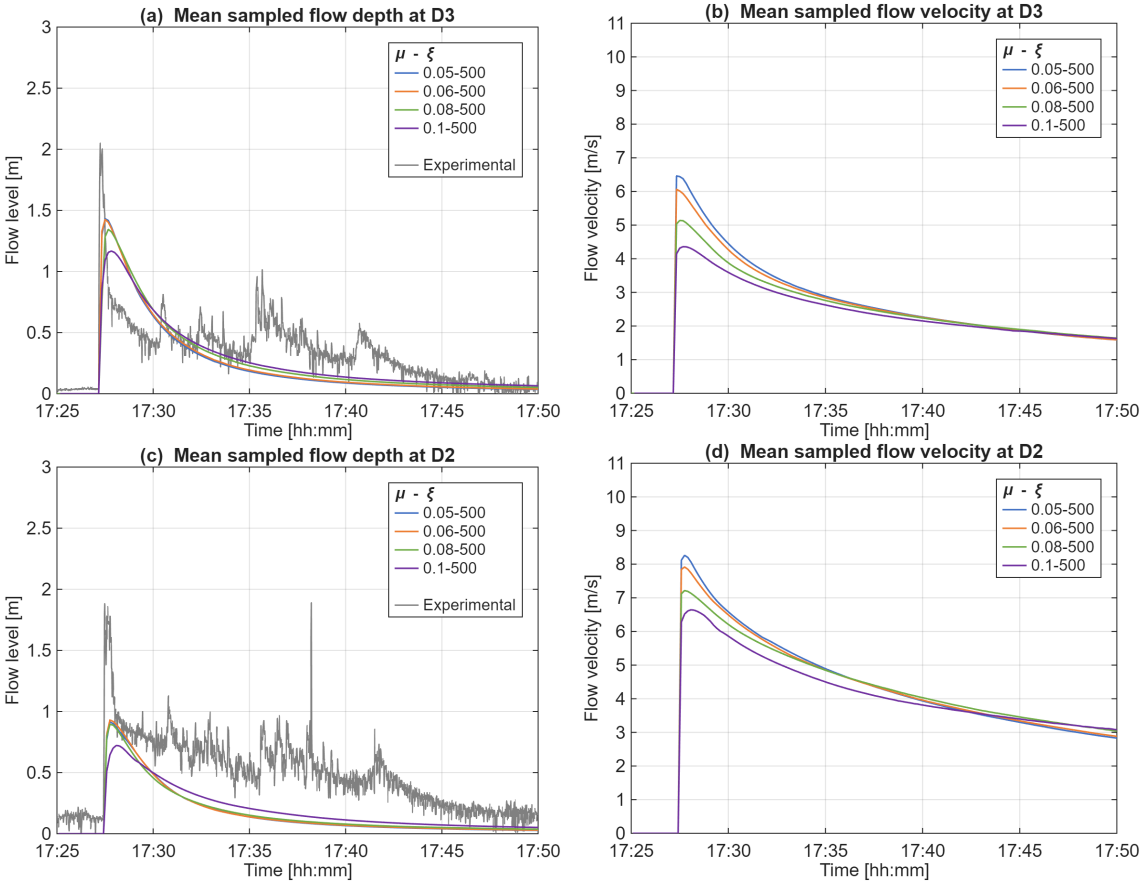


Figure A.3: Parametric analysis of the numerical response obtained from sampling areas centered at the actual monitoring sensor locations for the 18 July 2013 event varying μ at fixed ξ, with comparison against recorded flow depth: **(a)** mean sampled flow depth at D3; **(b)** mean sampled flow velocity at D3; **(c)** mean sampled flow depth at D2; **(d)** mean sampled flow velocity at D2.

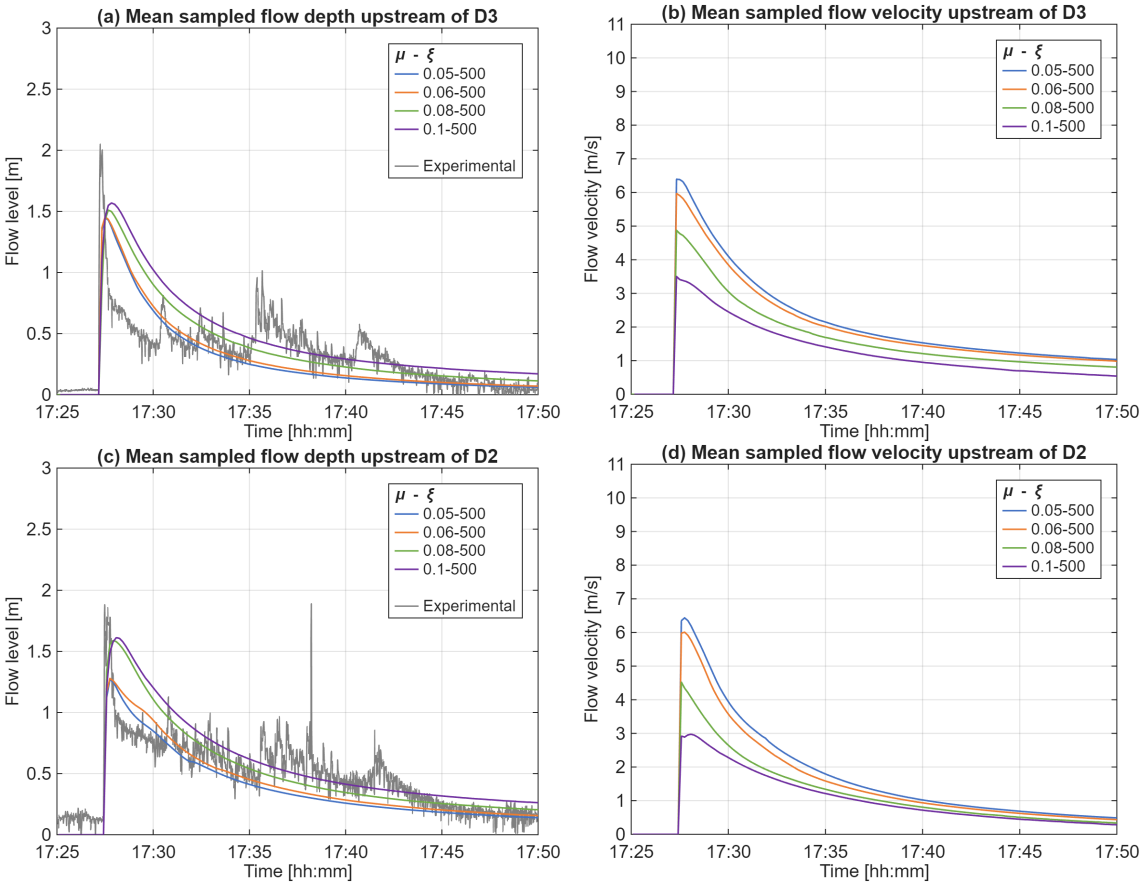


Figure A.4: Preliminary analysis of the numerical response obtained from sampling areas shifted upstream of the monitoring sensor locations for the 18 July 2013 event varying μ at fixed ξ, with comparison against recorded flow depth : **(a)** mean sampled flow depth upstream of D3; **(b)** mean sampled flow velocity upstream of D3; **(c)** mean sampled flow depth upstream of D2; **(d)** mean sampled flow velocity upstream of D2.

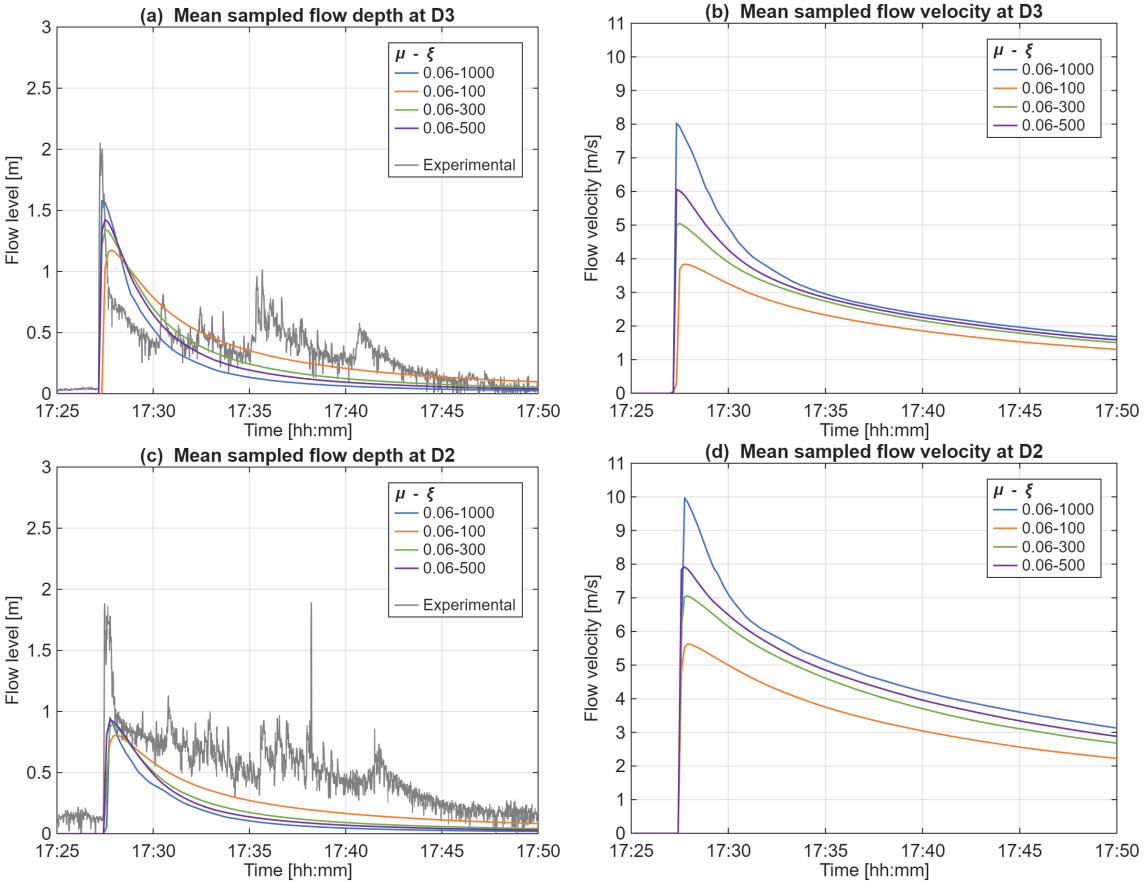


Figure A.5: Parametric analysis of the numerical response obtained from sampling areas centered at the actual monitoring sensor locations for the 18 July 2013 event varying ξ at fixed μ, with comparison against recorded flow depth : **(a)** mean sampled flow depth at D3; **(b)** mean sampled flow velocity at D3; **(c)** mean sampled flow depth at D2; **(d)** mean sampled flow velocity at D2.

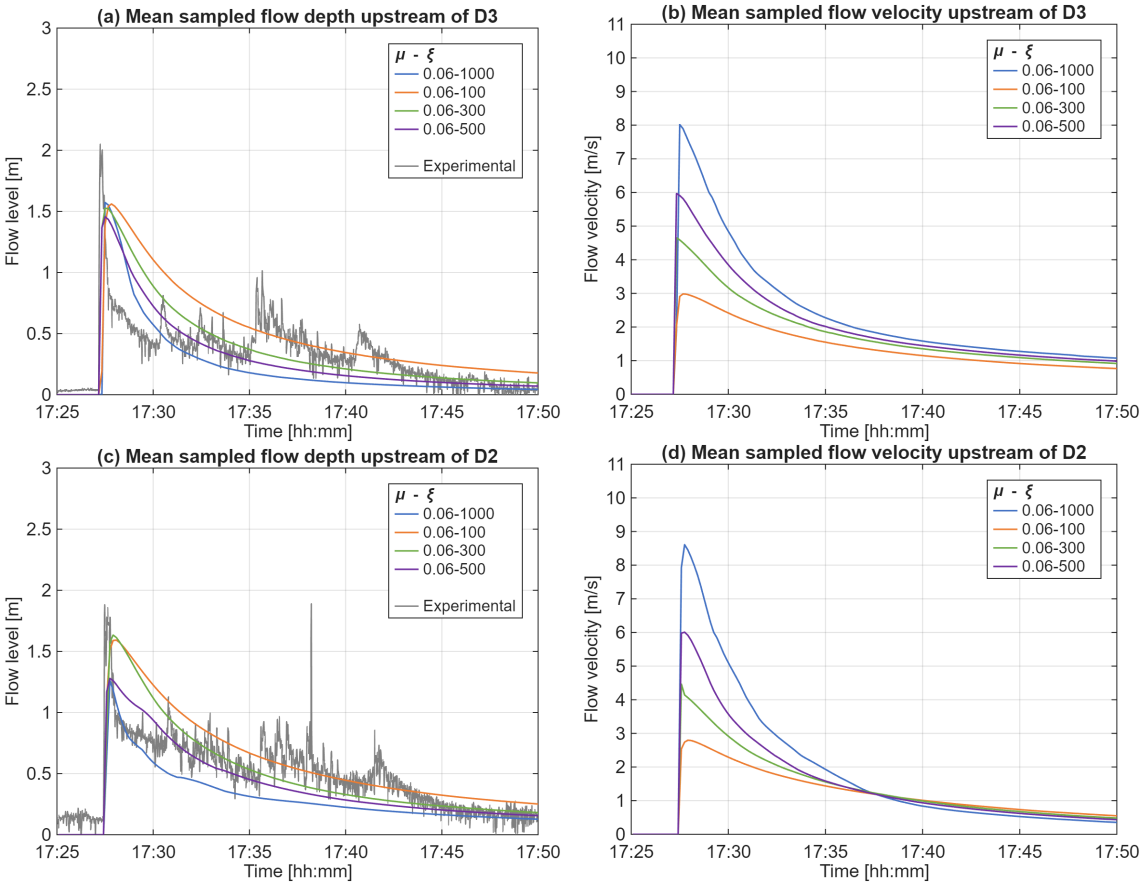


Figure A.6: Parametric analysis of the numerical response obtained from sampling areas shifted upstream of the monitoring sensor locations for the 18 July 2013 event varying ξ at fixed μ, with comparison against recorded flow depth : **(a)** mean sampled flow depth upstream of D3; **(b)** mean sampled flow velocity upstream of D3; **(c)** mean sampled flow depth upstream of D2; **(d)** mean sampled flow velocity upstream of D2.

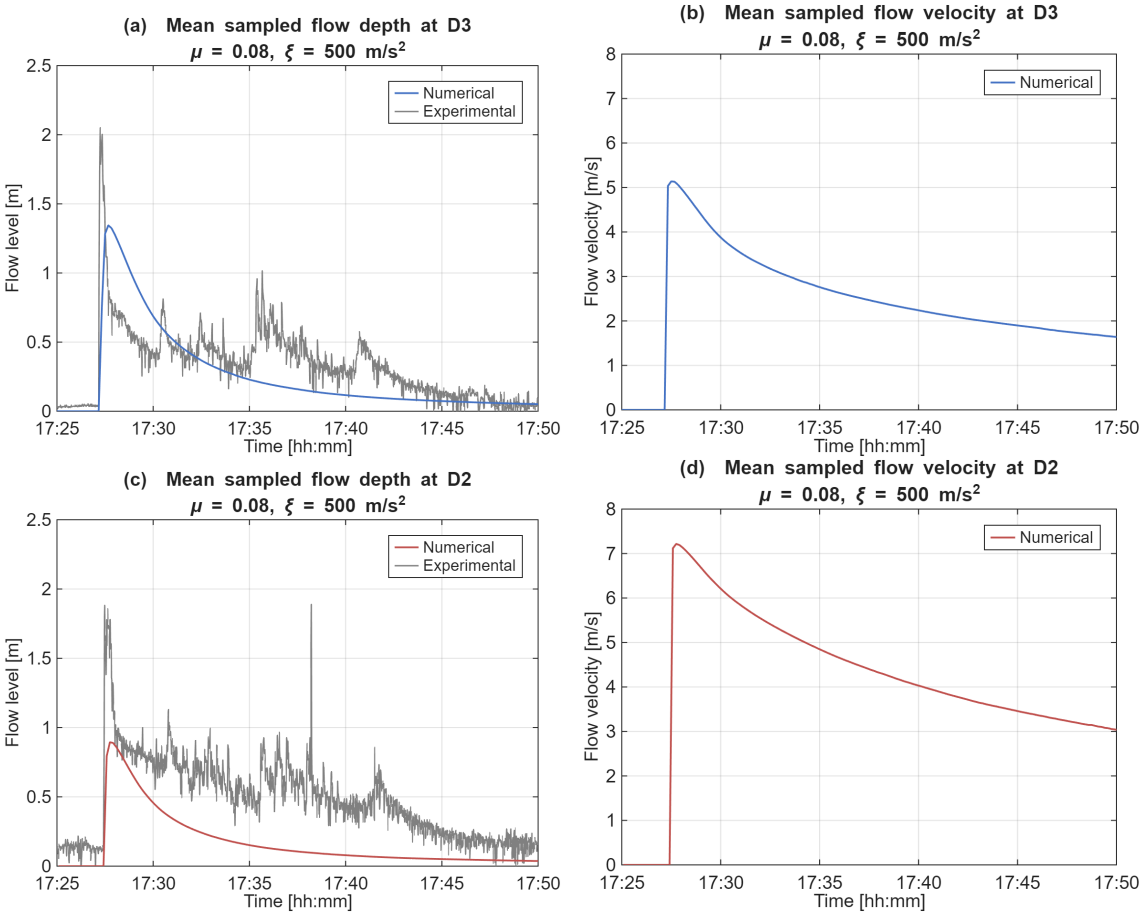


Figure A.7: Comparison of the numerical response obtained from sampling areas centered at the actual monitoring sensor locations against recorded flow depth for the 18 July 2013 event considering $\mu = 0.08$ and $\xi = 500$ m/s^2: **(a)** mean sampled flow depth at D3; **(b)** mean sampled flow velocity at D3; **(c)** mean sampled flow depth at D2; **(d)** mean sampled flow velocity at D2.

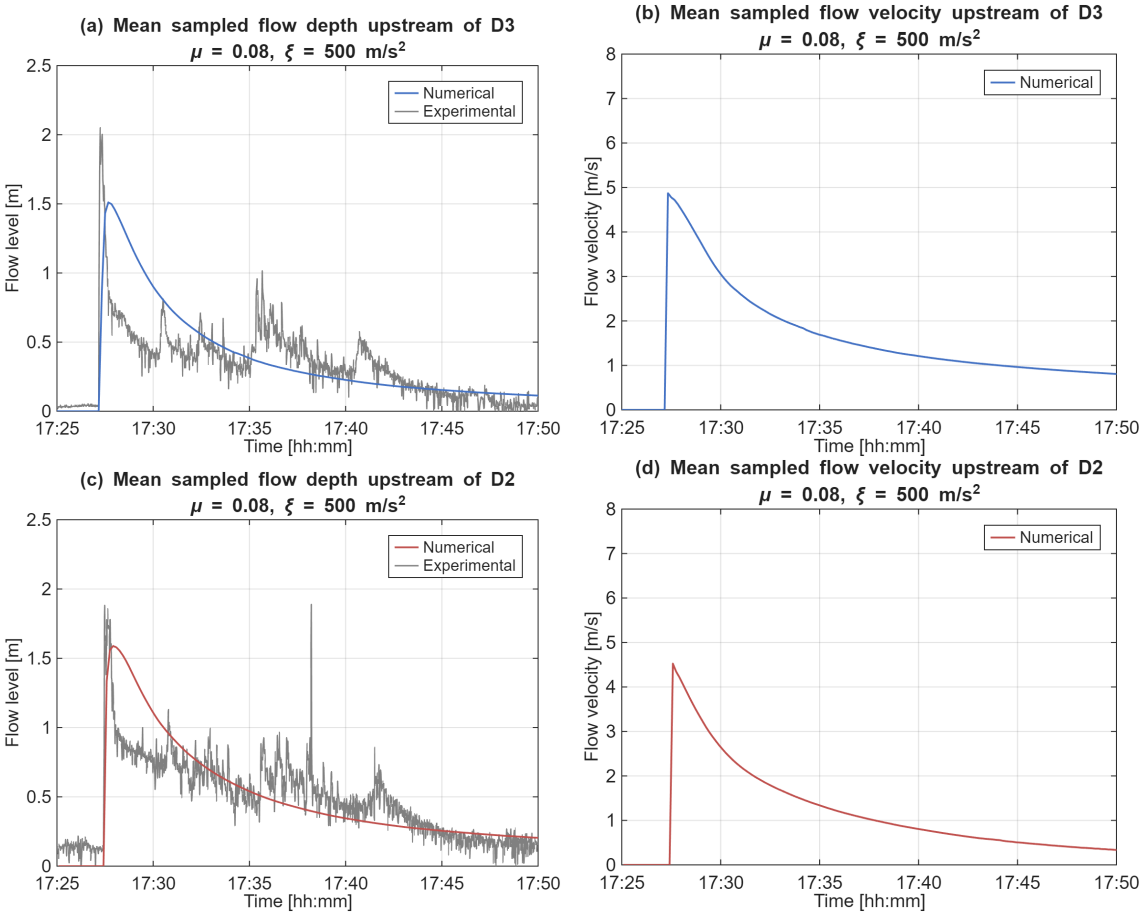


Figure A.8: Comparison of the numerical response obtained from sampling areas shifted upstream of the monitoring sensor locations against recorded flow depth for the 18 July 2013 event considering $\mu = 0.08$ and $\xi = 500$ m/s^2: **(a)** mean sampled flow depth upstream of D3; **(b)** mean sampled flow velocity upstream of D3; **(c)** mean sampled flow depth upstream of D2; **(d)** mean sampled flow velocity upstream of D2.

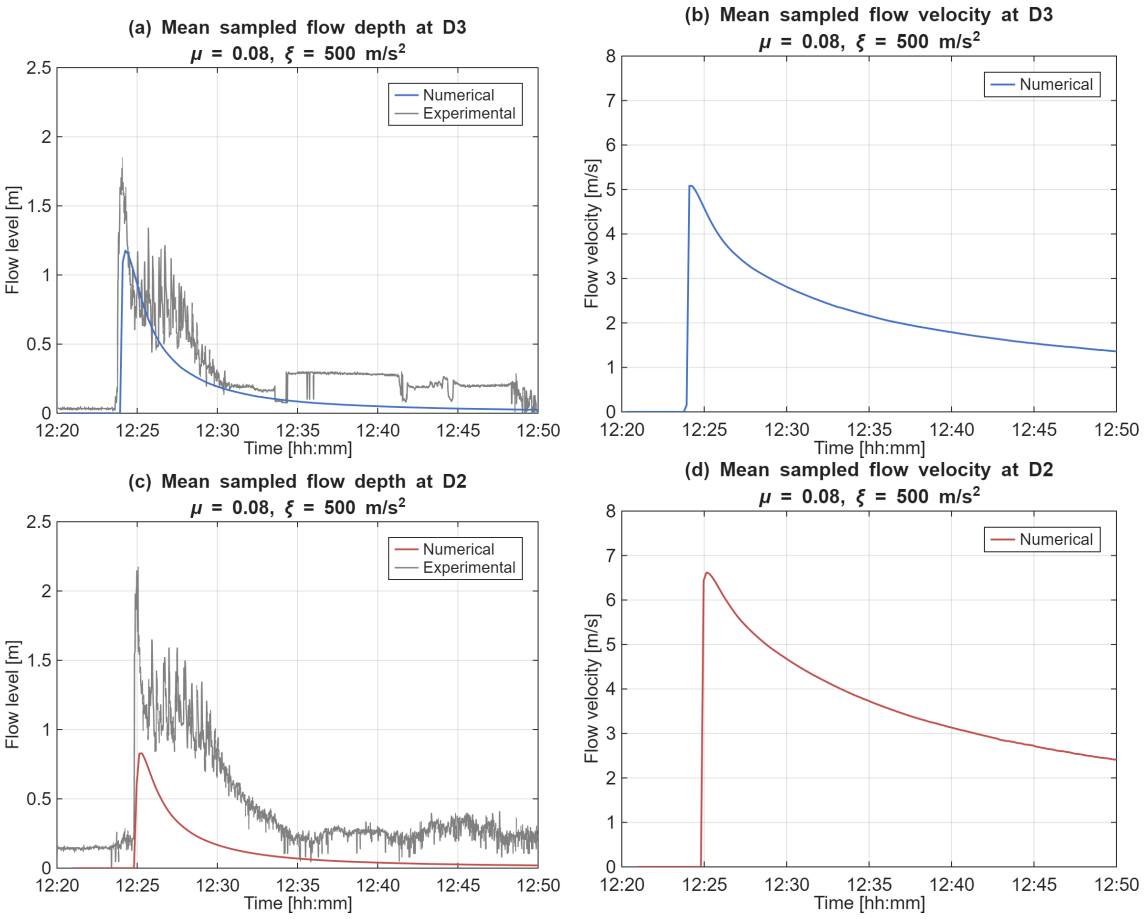


Figure A.9: Comparison of the numerical response obtained from sampling areas centered at the actual monitoring sensor locations against recorded flow depth for the 26 July 2019 event using the rheological parameters calibrated on the 2013 event: **(a)** mean sampled flow depth at D3; **(b)** mean sampled flow velocity at D3; **(c)** mean sampled flow depth at D2; **(d)** mean sampled flow velocity at D2.

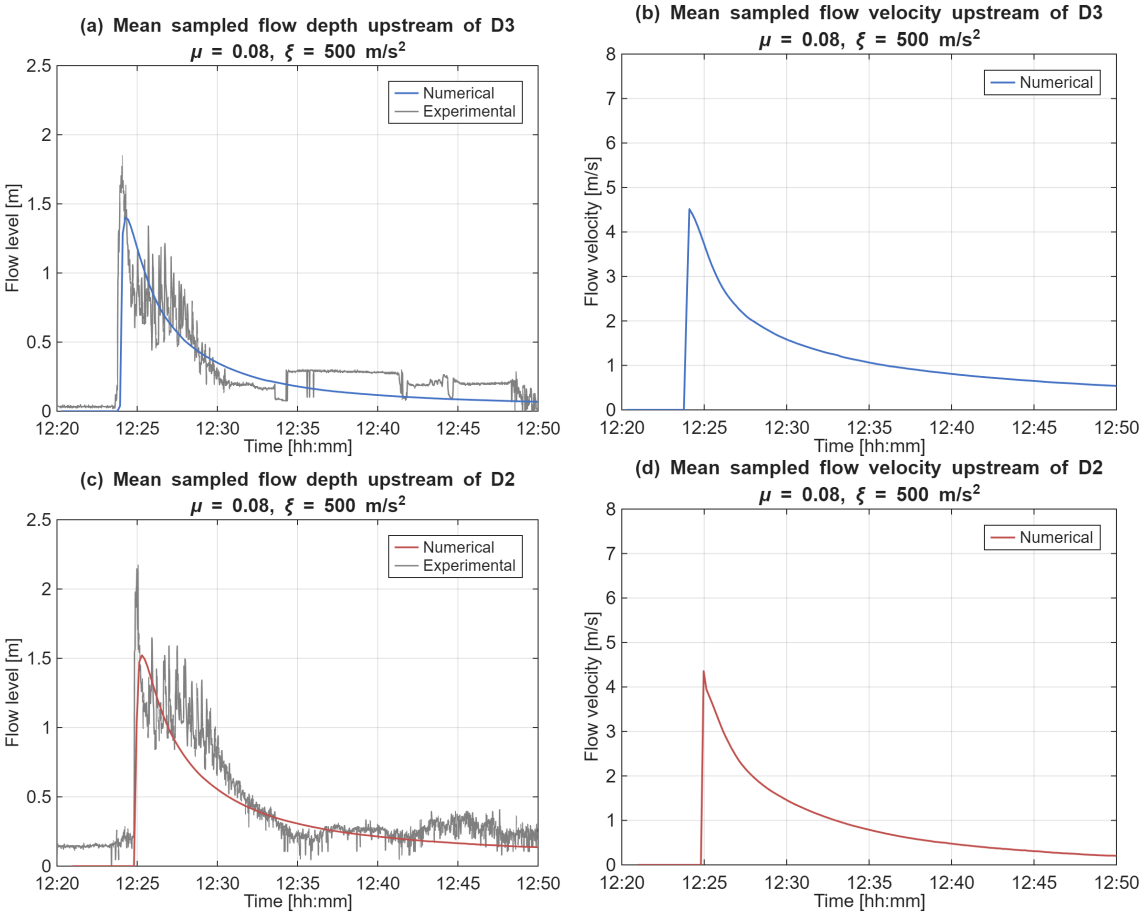


Figure A.10: Comparison of the numerical response obtained from sampling areas shifted upstream of the monitoring sensor locations against recorded flow depth for the 26 July 2019 event using the rheological parameters calibrated on the 2013 event: **(a)** mean sampled flow depth upstream of D3; **(b)** mean sampled flow velocity upstream of D3; **(c)** mean sampled flow depth upstream of D2; **(d)** mean sampled flow velocity upstream of D2.

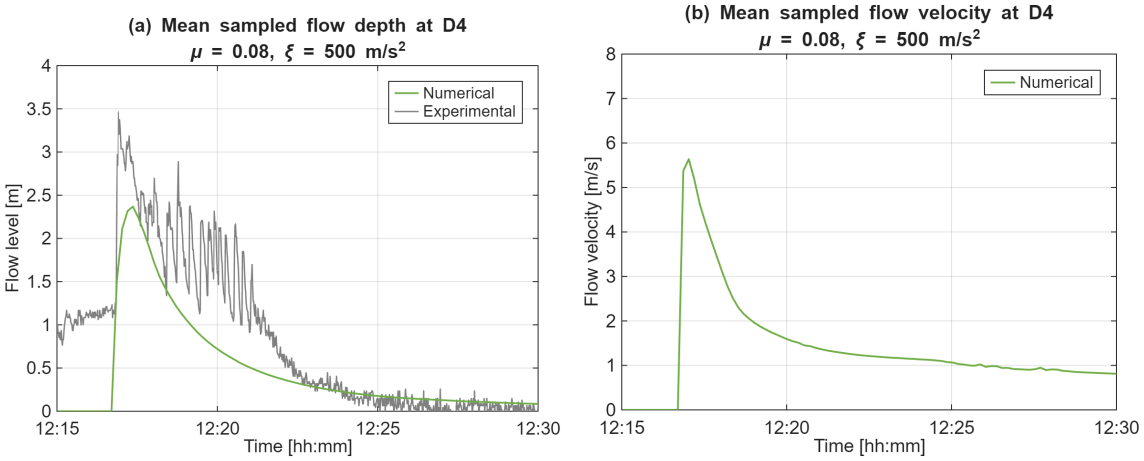


Figure A.11: Comparison of the numerical response at monitoring section D4 against the recorded flow depth for the 26 July 2019 event using the rheological parameters calibrated on the 2013 event: **(a)** mean sampled flow depth at D4; **(b)** mean sampled flow velocity at D4.

Overall, the mean flow-depth and velocity results show temporal trends consistent with those observed for the corresponding maximum values, while generally exhibiting slightly lower values.

Bibliography

Ahmadi-Adli, M. (2014). *Shallow landslides triggered by rainfall in unsaturated soils*. PhD thesis. Ankara, Turkey: Middle East Technical University.

Bird, R. B., W. E. Stewart, and E. N. Lightfoot (2007). *Transport Phenomena*. 2nd ed. New York, USA: John Wiley & Sons.

Brardinoni, F., V. Picotti, S. Maraio, P. P. Bruno, M. Cucato, C. Morelli, and V. Mair (2018). "Postglacial evolution of a formerly glaciated valley: Reconstructing sediment supply, fan building, and confluence effects at the millennial time scale". In: *Bulletin* 130.9-10, pp. 1457–1473.

Bressan, L. (2024). *Elaborazione delle mappe del pericolo da colata detritica sul bacino del Rio Gadria (BZ)*. Master's thesis. Padova, Italy: Università degli Studi di Padova.

Cavalli, M., S. Trevisani, F. Comiti, and L. Marchi (2013). "Geomorphometric assessment of spatial sediment connectivity in small Alpine catchments". In: *Geomorphology* 188, pp. 31–41.

Comiti, F., L. Marchi, P. Macconi, M. Arattano, G. Bertoldi, M. Borga, F. Brardinoni, M. Cavalli, V. D'Agostino, D. Penna, et al. (2014). "A new monitoring station for debris flows in the European Alps: first observations in the Gadria basin". In: *Natural hazards* 73.3, pp. 1175–1198.

Coviello, V., J. I. Theule, L. Marchi, F. Comiti, S. Crema, M. Cavalli, M. Arattano, A. Lucía, and P. Macconi (2019). "Deciphering sediment dynamics in a debris-flow catchment: Insights from instrumental monitoring and high-resolution topography". In: *Proceedings of the 7th International Conference on Debris-Flow Hazards Mitigation*. Golden, Colorado, USA: Association of Environmental and Engineering Geologists, pp. 103–110.

Coviello, V., J. I. Theule, S. Crema, M. Arattano, F. Comiti, M. Cavalli, A. LucÍa, P. Macconi, and L. Marchi (2021). "Combining instrumental monitoring and high-resolution topography for estimating sediment yield in a debris-flow catchment". In: *Environmental & Engineering Geoscience* 27.1, pp. 95–111.

Cruden, D. (1991). "A simple definition of a landslide." In: *Bulletin of Engineering Geology & the Environment* 43.1.

Cruden, D. and D. J. Varnes (1996). "Landslide Types and Processes". In: *Landslides: Investigation and Mitigation*. Ed. by A. K. Turner and R. L. Schuster. Special Report 247. Washington, D.C.: Transportation Research Board, National Research Council, pp. 36–75.

D'Agostino, V. and G. Bertoldi (2014). "On the assessment of the management priority of sediment source areas in a debris-flow catchment". In: *Earth Surface Processes and Landforms* 39.5, pp. 656–668.

Dei Cas, L., A. Trigila, and C. Iadanza (2021). *Linee Guida per il monitoraggio delle frane*. Linee Guida SNPA 32/2021. Roma: Sistema Nazionale per la Protezione dell'Ambiente (SNPA).

Duncan, J. M., S. G. Wright, and T. L. Brandon (2014). *Soil Strength and Slope Stability*. 2nd ed. Hoboken, NJ: John Wiley & Sons.

Fell, R. (1994). "Landslide risk assessment and acceptable risk". In: *Canadian Geotechnical Journal* 31.2, pp. 261–272.

Finis, E. de, P. Gattinoni, L. Marchi, and L. Scesi (2017). "Modeling debris flows in anomalous basin-fan systems". In: *Workshop on World Landslide Forum*. Springer, pp. 601–609.

Glade, T., M. G. Anderson, and M. J. Crozier, eds. (2005). *Landslide Hazard and Risk*. Chichester, UK: John Wiley & Sons.

Guzzetti, F., A. Carrara, M. Cardinali, and P. Reichenbach (1999). "Landslide hazard evaluation: a review of current techniques and their application in a multi-scale study, Central Italy". In: *Geomorphology* 31.1-4, pp. 181–216.

Hatchinson, J. (1988). "Morphological and geotechnical parameters of landslides in relation to geology and hydrology." In: *Proc. 1st. Int. Symp. on Landslides." Landslides"*. Vol. 1, pp. 3–35.

Hock, R., G. Rasul, C. Adler, B. Cáceres, S. Gruber, Y. Hirabayashi, M. Jackson, A. Kääb, S. Kang, S. Kutuzov, et al. (2019). "High mountain areas". In: *IPCC special report on the ocean and cryosphere in a changing climate*. H.-O. Pörtner, DC Roberts, V. Masson-Delmotte, P. Zhai, M. Tignor, E . . ., pp. 131–202.

Hungr, O. (2000). "Analysis of debris flow surges using the theory of uniformly progressive flow". In: *Earth surface processes and landforms: the journal of the British Geomorphological Research Group* 25.5, pp. 483–495.

Hungr, O., S. G. Evans, M. J. Bovis, and N. J. Hutchinson (2001). "A Review of the Classification of Landslides of the Flow Type". In: *Environmental & Engineering Geoscience* 7.3, pp. 221–238.

Hungr, O., S. Leroueil, and L. Picarelli (2014). "The Varnes classification of landslide types, an update". In: *Landslides* 11.2, pp. 167–194.

Hürlimann, M., D. Rickenmann, V. Medina, and A. Bateman (2008). "Evaluation of approaches to calculate debris-flow parameters for hazard assessment". In: *Engineering Geology* 102.3-4, pp. 152–163.

IPCC (2021). *Climate Change 2021: The Physical Science Basis*. Cambridge, United Kingdom and New York, NY, USA: Cambridge University Press.

Iverson, R. M. (1997). "The physics of debris flows". In: *Reviews of geophysics* 35.3, pp. 245–296.

— (2000). "Landslide triggering by rain infiltration". In: *Water resources research* 36.7, pp. 1897–1910.

Jakob, M. and O. Hungr (2005). *Debris-flow Hazards and Related Phenomena*. Springer Praxis Books. Heidelberg, Germany: Springer Science Business Media.

Julien, P. Y. and Y. Lan (1991). "Rheology of hyperconcentrations". In: *Journal of Hydraulic Engineering* 117.3, pp. 346–353.

La Porta, G., A. Leonardi, M. Pirulli, F. Cafaro, and F. Castelli (2024). "Time-resolved triggering and runout analysis of rainfall-induced shallow landslides". In: *Acta Geotechnica* 19.4, pp. 1873–1889.

Leroueil, S. and R. Chandler (2001). "Natural slopes and cuts: movement and failure mechanisms". In: *Géotechnique* 51.3, pp. 197–243.

Mangeney, A., P. Heinrich, and R. Roche (2000). "Analytical solution for testing debris avalanche numerical models". In: *Pure and Applied Geophysics* 157.6, pp. 1081–1096.

Marchi, L., V. Coviello, F. Comiti, S. Crema, M. Cavalli, and P. Macconi (2019). "Rainfall threshold for debris flow occurrence in the Gadria catchment, Eastern Italian Alps". In: *EGU General Assembly Conference Abstracts*. Vienna, Austria: European Geosciences Union.

Marchi, L., V. Coviello, M. Cavalli, F. Comiti, S. Crema, and P. Macconi (2023). "Monitoring debris flows in the Gadria catchment (eastern Italian Alps): Data and insights acquired from 2018 to 2020". In: *E3S Web of Conferences*. Vol. 415. EDP Sciences.

McDougall, S. (2017). "2014 Canadian Geotechnical Colloquium: Landslide runout analysis—current practice and challenges". In: *Canadian Geotechnical Journal* 54.5, pp. 605–620.

Nagl, G., J. Hübl, and R. Kaitna (2019). "Measurements of velocity profiles in natural debris flows: a view behind the muddy curtain". In: *Proceedings of the 7th International Conference on Debris-Flow Hazards Mitigation*. Golden, Colorado, USA: Association of Environmental and Engineering Geologists, pp. 177–183.

— (2020). "Velocity profiles and basal stresses in natural debris flows". In: *Earth Surface Processes and Landforms* 45.8, pp. 1764–1776.

— (2022). "Stress anisotropy in natural debris flows during impacting a monitoring structure". In: *Landslides* 19.1, pp. 211–220.

Paganini, P., A. Pavan, and A. Conighi (2011). "Rilievo laser scan ed aerofotografico del bacino del torrente Strimm". In: *Relazione Interna OGS 2011/117 GDL 45*.

Pirulli, M. (2005). *Numerical modelling of landslide runout. A continuum mechanics approach*. PhD thesis. Torino, Italy: Politecnico di Torino.

Pirulli, M. and A. Mangeney (2008). "Results of back-Analysis of the propagation of rock avalanches as a function of the assumed rheology". In: *Rock Mechanics and Rock Engineering* 41.1, pp. 59–84.

Pirulli, M. (2010). "Morphology and substrate control on the dynamics of flowlike landslides". In: *Journal of geotechnical and geoenvironmental engineering* 136.2, pp. 376–388.

Pirulli, M., C. Scavia, and M. Tararbra (2015). "On the use of numerical models for flow-like landslide simulation". In: *Engineering Geology for Society and Territory-Volume 2: Landslide Processes*. Springer, pp. 1625–1628.

Pirulli, M., M. Barbero, M. Marchelli, and C. Scavia (2017). "The failure of the Stava Valley tailings dams (Northern Italy): numerical analysis of the flow dynamics and rheological properties". In: *Geoenvironmental Disasters* 4.1.

Raich, H. (2011). *Analisi della pericolosità del bacino del Rio Gadria attraverso indagini storico-documentali*. MA thesis. Padova, Italy: Università degli Studi di Padova.

Simoni, S., G. Vignoli, and B. Mazzorana (2017). "Enhancing sediment flux control and natural hazard risk mitigation through a structured conceptual planning approach". In: *Geomorphology* 291, pp. 159–173.

Theule, J. I., S. Crema, L. Marchi, M. Cavalli, and F. Comiti (2018). "Exploiting LSPIV to assess debris-flow velocities in the field". In: *Natural Hazards and Earth System Sciences* 18.1, pp. 1–13.

Turner, A. K. and R. L. Schuster, eds. (1996). *Landslides: Investigation and Mitigation*. Special report / Transportation Research Board, National Research Council 247. Washington, DC: National Academy Press.

Varnes, D. J. (1978). "Slope movement types and processes". In: *Special report* 176.11.

Website References

Google (2026). *Google Maps Satellite Imagery*. URL: https://maps.google.com (visited on 06/13/2026).

Provincia Autonoma di Bolzano - Alto Adige (2026a). *GadriaLab – Sito di monitoraggio di colate detritiche sul Rio Gadria*. URL: https://pericoli-naturali.provincia.bz.it/it/gadrialab-sito-di-monitoraggio-di-colate-detritiche-sul-rio-gadria (visited on 06/16/2026).

— (2026b). *GeoBrowser MapView*. URL: https://mapview.civis.bz.it/ (visited on 06/13/2026).

Acknowledgements

I would like to express my sincere gratitude to Prof. Marina Pirulli, my thesis supervisor, for her guidance throughout this work and for the valuable advice.

I am especially grateful to Dr. Giulia La Porta, my co-supervisor, for closely supporting me throughout the development of this thesis. Her constant assistance and valuable suggestions were essential to the completion of this work.

I would like to thank Dr. Lorenzo Marchi (CNR-IRPI) for sharing his extensive knowledge of the Rio Gadria catchment and for the valuable scientific insights that contributed to this study.

My thanks also go to Prof. Andrea Andreoli (Libera Università di Bolzano), Dr. Marco Martini, and Dr. Pierpaolo Macconi (both from Centro Funzionale provinciale dell'Agenzia per la Protezione Civile della Provincia Autonoma di Bolzano) for kindly providing the documentation, data, and technical material used in this research.

Finally, I would like to express my gratitude to Prof. Claudio Scavia, whose passion for teaching led me to develop an interest in geotechnical engineering.